Wave Based Modeling Methods for Acoustic Inclusion and Multiple Scattering Problems in the Mid-Frequency Range

Onur ATAK

Examination committee:
Prof. dr. ir. W. Sansen, chair (public)
Prof. dr. ir. C. Vandecasteele, chair (prelim.)
Prof. dr. ir. W. Desmet, supervisor
Dr. ir. B. Pluymers, supervisor
Prof. dr. ir. D. Huybrechs, supervisor
Prof. dr. ir. P. Sas
Prof. dr. ir. D. Vandepitte
Prof. dr. J. Sánchez-Dehesa
(Universitat Politècnica de València)
Prof. dr. Ing. G. Müller
(Techniche Universität München)

Dissertation presented in partial fulfillment of the requirements for the degree of Doctor in Engineering Science

July 2014

Uitgegeven in eigen beheer, Onur Atak, Celestijnenlaan 300B box 2420, B-3001 Heverlee (Belgium)

ISBN 978-94-6018-869-5

D/2014/7515/93

Acknowledgements

I have always felt lucky in life that things come together nicely. Now, yet another piece (a big one for sure!) is falling into its place and I feel lucky again. I feel lucky because I was surrounded by so many great people. Not only that they made this journey incredibly fun but also very enriching and enlightening. So, on the eve of this happy occasion, I would like to thank them and express my gratitude.

First of all, I would like to thank my supervisors Wim Desmet, Bert Pluymers and Daan Huybrechs. Wim, you have never ceased to impress and inspire me during my time at PMA. Be it your vast knowledge on the field or your "time bending" scheduling abilities or your skills in finding always the right words... You have helped me improve myself in so many ways. I have always felt grateful to be a part of your team, so thank you for giving me this opportunity and for all the things you have done for me! Bert, you have always been the greatest motivator for me. Your enthusiasm towards your work, your professionalism and broad skill set are so impressive, even just being around you pushed me to try my best towards everything that I encountered during my PhD. Even the small tasks that may sound tedious became attractive because of your dedication. What is great is that, on top of all of these things, you were a great company for drinking beers as well :) So, thanks for all of these things and more! Daan, you have truly broadened my perspective and provided different angles to my work. Our meetings always pushed me to bend my engineering point of view, which made them both enlightening and fun. You were always so good at explaining the complicated concepts in an easy way and that thought me a lot. Thank you for helping me and for the good times we spent.

I would like to thank Paul Sas and Dirk Vandepitte as well, who were the assessors in my jury and contributed to the improvement of the manuscript. Thank you Paul for providing a good overview and thank you Dirk for your double attention to details. I appreciated all the comments coming from both of you and also our social interactions over the years, which always made me feel welcome.

I would like to extend my gratitude to the external jury members, Prof. Müller and Prof. Sánchez-Dehesa. Thank you for all your suggestions and comments which helped improving my work. Both of you were very kind and supportive

and that was invaluable to me, knowing that such comments were coming from people who are highly respected in their fields. I hope our paths would cross each other again soon, in another occasion.

I would like to thank Koos Huijssen and Monika Rychtarikova for their contributions to Chapter 3. Koos was very kind to provide the FM-BEM results and Monika shared the measurement data with ray tracing results. Thank you both, as I enjoyed our collaboration thoroughly.

There are of course many colleagues that I would like to thank for contributing to my work and making my time at PMA so enjoyable. I would like to start with the "wave group". Bert VG, thank you for your innovative work on the ML-WBM, which formed the basis of my research. While I did not have the chance to interact with you too much about work when you were at PMA, I had the pleasure to discover the fun-outside-the-work Bert afterwards and really enjoyed my time around you. Sharing your wisdom (and sometimes misery :) on being a father was very useful for me, so thanks for that as well. Bart, when I first started my research and had lot of questions, you were there to answer them and provide the critical insight. While Bert VG's work was the basis, yours was the first building block towards my work and thanks for that. Of course our interaction was merely work related after the first years :) Thanks for all the good memories, looong chats and for always staying with me to see the end of the bottle ;) Karel, your patience and willingness to help me (especially on my Dutch practices!) were very valuable to me. I have to admit that after you left the office, my language skills took a nose dive so I hope we can catch up on that! Elke, my dear (!) neighbor... Trying to explain everything would take too long so I hope these keywords would help :) Thanks for the flying sharp objects, the cold war, squash wounds, the napping tiger, rroochk werchhterr, the extra whiskey and more! And of course thanks for your help on the WBM topics, for always making spot on suggestions and all the cooperation! Roberto, I have always enjoyed our conversations, I have learned a lot from them and always appreciated your insights, so thanks for that. Your main contribution to my work, however, happened at the moment you introduced me to the Italian coffee! Staying awake in the afternoons can be quite crucial during a PhD, so this work literally might not have existed without you :) Thanks! Stijn, we might be on the opposite sides of the "organized-chaotic" scale, but this did not stop us from being partners-in-crime in many occasions! Be it the fully technical, work related talks or full-nerd-mode Star Wars conversations, you have made my time better at PMA, so thanks for that! Kunmo, it has always been my pleasure to learn more about your work and also Korean culture. Thanks for all the interesting talks! Also, I hope that "so-so" means "good" ;) Hendrik, it is really nice to see that the WBM research is at safe hands with you and thank you also for providing the much needed gaming chat during the coffee breaks :) Laurens, I have really enjoyed working closely with you on isogeometric analysis and I am looking forward to collaborate more! Thanks for making this new concept easy for me and also for being always a good company.

There are also many more people that I would like to thank outside of the wave group. While they may not have direct technical influence on my work, they helped creating a very friendly working/living environment during this journey, so their contribution is equally important to me.

Matt, I would like to thank you for sharing my enthusiasm for basketball! Before you came, I always had the look from people like "what is this weird sport you are talking about?" :) While I still get that look from time to time, at least now I got only half the attention :p Axel, at a pace that was never seen before, you managed to find your place in our group with the "special Axel section" :) Thanks for creating such memorable moments in the office! Tjorven, thanks for the funniest conversations and the "age of" events! My colleagues from "the other side" deserve a mention too. Marianna, Tommaso, Claus, Andy, Jan and Frank, thank you all for the good times and interesting conversations. Wim Verhaeghe, you have a special place in my hearth and I will always miss you and remember you fondly. I would like to thank all the people that are and were a part of the MHF group, for contributing to create such a nice working environment.

I would like to tip my hat to all the fellows and supervisors I met through the Mid-Frequency project. I have learned so many things during this project and have great memories from the events. Thank you all for making the project a great success and fun experience!

I would like to thank our secretaries Lieve, Karin, Regine and Valerie for helping me with all kinds of situations and being always welcoming! Also, I would like to thank Jan and Ronny for being supportive and solving all the IT problems.

Maliciğim ve Denizciğim, sizler olmasaydınız Leuven günlerimiz bu kadar güzel geçemezdi. 100. Yıl ruhunu burada yaşatmamıza yardımcı olduğunuz için çook teşekkürler, iyi ki varsınız! Asım ve Korcan (sizden de çift gibi bahsetmem talihsiz oldu kusura bakmayın :)); doktora serüveninin başından beri çok bilinmezli denklemin değişmezleri oldunuz ;) Sayısız biraya ve maceralara ortak olduğunuz için teşekkürler! Eda, Onur M, Aysu, Hakan B, Onur K, Burak, Tuğba, Hakan I, Latif, Duygu.. hepinize çok teşekkürler! Gurbet sizlerle güzel :)

Thomas, Cladia, Manu, Paula, Yves, Doa, Iffy, Tina and Adrien; thanks guys for the great company!

Greatest acknowledgement goes to my family! I would like to thank my parents and my brother for supporting me in every sense of the word through my years abroad. The most difficult thing to endure was being away from you. I love you so much and as the years past, I realize more and more the importance of the things that you have thought me and become more grateful to you for raising me as the person I am. Thank you!

Anneciğim, babacığım ve turtim, beni her konuda sonuna kadar desteklediğiniz için sonsuz teşekkürler. Doktoramın benim için en zor kısmı sizlerden ayrı kalmaktı. Sizi çok seviyorum ve yıllar geçtikçe bana kattıklarınızın önemini

daha iyi anlıyor ve beni bu şekilde yetiştirdiğiniz için sizlere daha da minnettar oluyorum. Sizleri kocaman öpüyorum!

My beautiful daughter Arya, you have brought so much happiness to my life that there are not enough words to express it. Watching you grow and getting to know you better as you reveal your character are amazing experiences! I can't wait to see the day that you will be reading these lines!

Güzel kızım Arya, hayatıma kattığın neşeyi tarif etmemin imkanı yok. Senin büyümene tanık olmak, karakterin oluştukça seni daha yakından tanımak deneyimlerin en güzeli! Bu satırları okuyacağın günleri iple çekiyorum ve seni kocaman öpüyorum!

My beautiful wife Zeynep, every day you are proving me wrong; because I thought I would not be able to love you more! Thank you for being my beloved wife, thank you for being the mother of Arya, thank you for making my life a joy and thank you for your unconditional support!

Onur
June 26, Leuven

Abstract

The effect of sound on living quality is significant. Good acoustic properties are not considered luxurious for commercial products anymore, but necessary. Therefore, designers and engineers have made acoustic design an integral part of the product cycle. As the computational resources become ever more powerful, the acoustic design process, together with the other engineering and design decisions shift more and more to the virtual environment. Consequently, the demand for good Computer Aided Engineering (CAE) tools is higher than ever.

Despite the critical reliance on the CAE tools and the considerable research effort being spent over the years, no single numerical method has emerged to provide full frequency solution to the acoustic problems. Instead, dedicated methods have been established for low- and high-frequency regions, such as the Finite Element Method, the Boundary Element Method, Statistical Energy Analysis, ray tracing methods etc. Whereas the aforementioned methods prevail in their target frequency ranges, they fail to address the mid-frequency range, either because of prohibitive calculation times or unfulfilled underlying assumptions. The Wave Based Method (WBM), which constitutes the core technology of the presented thesis, was developed for the efficient solution of steady-state acoustic problems in the mid-frequency range. The WBM is a meshless, deterministic numerical simulation technique, which uses expansions of exact solutions of the governing equation(s) to represent primary field variable(s). In order for the method to converge, the problem domain has to be convex or it has to be divided into convex subdomains, which limits its practical applicability to moderately complex geometries. This limitation is further exposed for certain problems settings. Inclusion and multiple scattering problems, which are instrumental for various engineering fields, are among those and require extensive partitioning of the domain to comply with the convexity criterion.

These specific problem settings do not only pose challenges for the WBM, but also for the domain discretization methods. A geometrically complex inclusion may drive the discretization criteria and may lead to long calculation times; multiple scatterers that are well separated make it difficult to apply absorbing boundary conditions and so on.

In light of the above statements, the presented work focuses on two main

aspects. Firstly, the current WBM technologies are assessed and enhanced in their own framework. Despite its geometrical limitations, the WBM and its recent extension Multi-level WBM can still be successfully applied to various practical problems. A room acoustics case is presented to demonstrate the efficiency of the WBM, which also motivates the use of the WBM in inclusion and multiple scattering problems. Symmetric boundary conditions in Cartesian coordinates are derived for the Multi-level WBM to address symmetric multiple scattering problems. The method is then used to design novel acoustic metamaterials in the form of acoustic lenses.

Secondly, geometrical requirements of the WBM are relaxed for inclusion and multiple scattering problems. A hybrid Boundary Element-Wave Based Method is developed to this end. The hybrid method combines the best of the two worlds. It benefits from the efficient solution of the WBM for simple scatterers or cavities and it uses the flexibility of the BEM for complex scatterers or inclusions. The method is derived for 2D and 3D problems and validated through various benchmark cases against the current state-of-the-art methods.

Through both contributions, the efficiency of the WBM and its ability to address the mid-frequency range is demonstrated.

Beknopte samenvatting

Geluid heeft een onmiskenbaar effect op de levenskwaliteit; goede akoestische eigenschappen zijn daarom een vereiste voor commerciële producten. Ontwerpers en ingenieurs beschouwen het akoestische ontwerp van hun product, naast o.a. mechanisch ontwerp, als een integraal stuk van de productcyclus. Door de opkomst van steeds rekenkrachtigere en performantere computers verschuift het akoestisch ontwerpproces samen met andere ingenieurs- en ontwerpbeslissingen steeds meer naar de virtuele omgeving. Bijgevolg is de vraag naar efficiënte rekenprogramma's groter dan ooit.

Ondanks deze nood en het vele onderzoek dat de laatste decennia is verricht, is er nog geen enkele numerieke methode beschikbaar die over het volledige hoorbare frequentiegebied inzetbaar is voor het oplossen van akoestische problemen. In plaats daarvan zijn er specifieke methodes ontwikkeld voor laag- en hoogfrequente analyses, zoals de eindige-elementenmethode, de randelementenmethode (REM), statistische energie analyse, *ray tracing* methodes, enz. Deze methodes zijn zeer performant voor hun vooropgesteld frequentiegebied, maar kunnen geen oplossing bieden in het zogenaamde middenfrequente gebied, ofwel door te lange rekentijden, ofwel door niet vervulde onderliggende veronderstellingen. De golfgebaseerde methode (GBM), die de kern vormt van dit proefschrift, is ontwikkeld met het oog op een efficiëntere oplossing van harmonische akoestische problemen in het middenfrequent gebied. De GBM is een deterministische numerieke methode die een gewogen som van exacte oplossingen van de heersende differentiaalvergelijking(en) gebruikt om de primaire veldveranderlijke(n) te benaderen. De methode maakt geen gebruik van een opdeling van het probleemdomein in kleine elementen. Het probleemdomein moet evenwel convex zijn, of moet opgedeeld worden in convexe deeldomeinen, om convergentie van de methode te garanderen. Hierdoor is de methode in de praktijk voornamelijk inzetbaar voor problemen met een beperkte geometrische complexiteit. De convexiteitseis vormt een sterke beperking voor sommige probleemtypes; caviteiten met inclusies en onbegrensde problemen met meerdere verstrooiers vereisen een partitionering van de probleemgeometrie in een zeer groot aantal deeldomeinen. De bovenvermelde probleemtypes stellen niet alleen grote uitdagingen aan de GBM, maar ook aan domeindiscretisatiemethodes; een geometrische complexe inclusie kan de elementgrootte bepalen en bijgevolg leiden tot zeer lange rekentijden;

meerdere gescheiden verstrooiers bemoeilijken het toepassen van absorberende randvoorwaarden, enz.

Met het oog op deze problemen concentreert dit werk zich op twee hoofdlijnen. Ten eerste worden de huidige GBM methodieken beoordeeld en vervolgens verbeterd binnen hun eigen kader. Ondanks de geometrische beperkingen zijn de GBM en diens meerlaagse uitbreiding inzetbaar voor een breed spectrum aan praktische problemen. Een ruimteakoestisch rekenprobleem toont de efficiëntie van de GBM en motiveert het gebruik van de GBM voor problemen met inclusies en meerdere verstrooiers. Het meerlaags modelleerconcept is verder verbeterd. Symmetrierandvoorwaarden zijn afgeleid in Cartesische coördinaten om symmetrische problemen met meerdere verstrooiers aan te pakken. De methode is vervolgens toegepast om nieuwe akoestische metamaterialen te ontwerpen in de vorm van akoestische lenzen.

Ten tweede worden de geometrische vereisten van de GBM afgezwakt voor problemen met inclusies en verstrooiers door de ontwikkeling van een hybride randelementen-golfgebaseerde methode. Deze methode combineert het beste van beide technieken; ze profiteert van de efficiënte GBM voor geometrisch eenvoudige verstrooiers of inclusies of caviteiten en maakt gebruik van de REM voor complexe verstrooiers of inclusies. De methode wordt voor zowel 2D als 3D geometrieën afgeleid en wordt gevalideerd voor verschillende voorbeelden t.o.v. courant gebruikte technieken.

Door beide bijdragen wordt de efficiëntie van de GBM en diens potentieel om middenfrequente problemen aan te pakken duidelijk gedemonstreerd.

List of symbols

Abbreviations

2D	Two-dimensional
3D	Three-dimensional
BEM	Boundary Element Method
CAE	Computer aided engineering
DoF	Degrees of freedom
DtN	Dirichlet-to-Neumann map
FEM	Finite Element Method
FM-BEM	Fast Multipole Boundary Element Method
FRF	Frequency response function
GA	Genetic Algorithm
Hybrid BE-WBM	Hybrid Boundary Element-Wave Based Method
Hybrid FE-WBM	Hybrid Finite Element-Wave Based Method
ML-WBM	Multi-level Wave Based Method
SAEs	Scattering Acoustic Elements
SCs	Sonic crystals
SEA	Statistical Energy Analysis
SPL	Sound pressure level
WBM	Wave Based Method

Arabic symbols

$\boldsymbol{A}_\bullet$		(System) matrix for $\bullet$
$\boldsymbol{C}_{\bullet,*}$		Coupling matrix between $\bullet$ and $*$
c		Acoustic speed of sound
$D^{(\bullet)}$		Acoustic domain
$\boldsymbol{F}_\bullet$		Matrix of forcing terms for $\bullet$
$G(\vec{r_1}, \vec{r_2})$		Green's kernel function
$H_n^{(2)}(\vec{r})$		Hankel function of the second kind and order n
$h_l^{(2)}(\vec{r})$		Spherical Hankel function of the second kind and order l
j		Imaginary unit, $\sqrt{(}-1)$
k		Acoustic wave number
$k_\bullet$		Acoustic wave number component
N_D		Number of WBM subdomains
$N_I^{(\gamma)}$		Number of interfaces in subdomain γ
$\vec{n}$		Normal vector
n_λ		Number of levels in ML-WBM or hybrid BE-WBM models
$n_w^{(\gamma)}$		Number of wave functions for WBM subdomain γ
$p(\vec{r})$		Acoustic pressure
$\hat{p}^{(\gamma)}(\vec{r})$		WBM approximation of the acoustic pressure for subdomain γ
$\hat{p}_f^{(\gamma)}(\vec{r})$		Particular solution field in WBM field variable expansion for subdomain γ
$p_w^{(\gamma)}(\vec{r})$		Pressure contribution from the WBM submodel (subdomain γ) for the hybrid BE-WBM
$p_b(\vec{r})$		Pressure contribution from the BEM submodel for the hybrid BE-WBM
$p_{tot}^{(\gamma)}(\vec{r})$		Total pressure field for the hybrid BE-WBM in the WBM subdomain γ
$P_l^m(x)$		Associated Legendre function of degree l and order m
$\vec{r}$		Position vector
$\vec{r_\bullet}$		Position vector, relative to $\bullet$
	r, θ	Polar coordinates
	r, ϕ, θ	Spherical coordinates
$R_\bullet^{(\gamma)}(*)$		Boundary residual term of the subdomain γ for the WBM
$R_\bullet^{ML(\gamma)}(*)$		Boundary residual term of the subdomain γ for the ML-WBM
$R_\bullet^{HYB(\gamma)}(*)$		Boundary residual term of the subdomain γ for the hybrid BE-WBM
$S_\bullet$		Boundary of the BEM submodel
T		Truncation factor for the WBM wave functions

$\tilde{t}^{(\gamma)}(\vec{r})$	Weighting function of the weighted residual formulation
$t_{\omega}^{(\gamma)}$	Weighting factor of the ωth wave function in subdomain γ
$t^{(\gamma)}$	Vector containing weighting factors of the wave functions in subdomain γ
v_n	Acoustic normal velocity
$Y_l^m(\vec{r})$	Spherical harmonics of degree l and order m
Z_n	Acoustic normal impedance

Greek symbols

$\Phi_w^{(\gamma)}(\vec{r})$	wth wave function for WBM subdomain γ
$\Phi^{(\gamma)}(\vec{r})$	Vector containing all wave functions for WB subdomain γ
$\Gamma_\bullet$	General boundary definition. It refers to the WBM submodel boundary in the hybrid BE-WBM context.
Γ_t^g	Global truncation circle/sphere boundary of the unbounded WBM
μ	Indirect BEM double layer potential
ω	Angular frequency
$\rho_\bullet$	Density
σ	Indirect BEM single layer potential

Miscellaneous symbols

∞	Infinity
∇	Gradient operator
∇^2	Laplacian operator
$\frac{\partial \bullet}{\partial *}$	Partial derivative
$\mathcal{L}_v$	Normal velocity operator
$\mid \bullet \mid$	Absolute value
$\overline{\bullet}$	Imposed quantity
$\bullet^T$	Transpose of a matrix
$\cup$	Union operator
$\cap$	Intersection operator
$\bullet^{(\alpha)}$	Entity related to bounded WBM subdomain α
$\bullet^{(\beta)}$	Entity related to general WBM subdomain β
$\bullet^{(\gamma)}$	Entity related to general WBM subdomain γ
$\bullet^{(+)}$	Entity related to unbounded WBM subdomain +
$\bullet^{(+,i)}$	Entity related to ith 'level' for the ML-WBM or the hybrid BE-WBM
$\bullet^{sym}$	Symmetric form of $\bullet$
$\bullet_p$	Entity related to pressure boundary condition
$\bullet_v$	Entity related to velocity boundary condition
$\bullet_Z$	Entity related to impedance boundary condition
$\bullet_I$	Entity related to interface condition
$\bullet_{*,t}$	Entity related to truncation circle/sphere

Contents

Chapter 1

Introduction

1.1 Importance of acoustics and CAE

Mechanical waves that propagate through a medium as pressure oscillations are referred to as sound, when the oscillation frequencies are within the limits of human hearing. As hearing constitutes a vital pillar in humans' perception of their surroundings, the effect of sound on humans is significant. As such, it is of high importance to control the sound in living environments.

The exposure to sound in daily life comes from various sources. They may come from transportation vehicles, domestic appliances, computers etc. When these exposures are discomforting and unwanted, it is mostly referred to as noise. Most of the efforts in controlling the sound concentrate on reducing the noise. Reduction of noise radiated from vehicles as well as sound absorption in the passenger cabins are typical examples. On the other hand, there are also considerable efforts being spent on amplifying or shaping the sound. For instance, loudspeakers are designed to accurately reproduce the source signals. The sound coming from closing a door of a vehicle can be designed to give a certain feeling of trust and quality association. Another example is manipulating the sound waves to predict the existence of an object as it is in radar applications.

To be able to manipulate the sound and create the aforementioned experiences, engineers make numerous design choices during product development. With the ever advancing computational power in today's world, these design choices are being more and more made in virtual prototypes in the early stages of the product development cycle. This ongoing transition to the use of Computer Aided Engineering (CAE) tools not only reduces the time-to-market but also the cost of physical prototyping. In addition, the expensive last minute changes to acoustic properties of the products are avoided because they are accounted for during the whole product cycle. Considering the fierce competition of the

global market and the struggle of brands, reducing the time-to-market and creating the best products with the least costs are crucial for success. This makes the importance of the use of CAE tools higher than ever. This reliance on the CAE tools also brings a critical research effort to the field surrounding the same goals, i.e. having robust, accurate and efficient numerical modeling methods, which are also user friendly.

1.2 Challenges in numerical modeling

Even with considerable research efforts being spent over numerous years, the numerical modeling methods for acoustic problems still experience critical problems. An ideal numerical method would be able to predict the varying nature of acoustic waves over the whole audible range, which starts from 20 Hz and goes up to 20 kHz, with great efficiency and accuracy. This task, however, is not trivial because the acoustic wavelength changes tremendously in this frequency range. In low frequencies, i.e. when the length of the acoustic waves is comparable to or larger than the size of the considered geometry, the system has deterministic behavior and is less prone to variabilities. Going higher in frequency, the wavelength becomes much smaller than the considered geometry and predicting the exact behavior of the system becomes harder because any small variation in the input parameters has great impact on the resulting wave field. Moreover, the deterministic data loses their relevance in representing an ensemble of products. Because of this difference in the system behavior at low and high frequencies, having one numerical modeling method to predict the acoustic behavior over the whole audible range is still very difficult to achieve and is the subject of ongoing research. In addition, acoustic problems are of global nature, which prohibits the modeling of subcomponents independent from each other. In other words, modeling of complete systems is required. As such, the size of the models can be very large, which makes the solution of these problems computationally expensive.

Because of the aforementioned difficulties in developing a single numerical method for the solution in full frequency range, the efforts have been divided to develop dedicated numerical methods for specific frequency ranges.

Low-frequency range In this frequency range, the system behavior is deterministic and less prone to variability. Therefore, modeling nominally identical geometries, e.g. products coming out of a production line, is possible by using deterministic methods. The most common low-frequency deterministic methods are the Finite Element Method (FEM) [153] and the Boundary Element Method (BEM) [149], which belong to the family of element based methods. The FEM is the most preferred method for bounded problems because of its efficiency and the BEM is the most preferred method for unbounded problems because it inherently satisfies the Sommerfeld radiation

condition. Both of them are element based methods that discretize the domain or boundaries of the problem into small elements.

For the FEM, the problem domain is discretized and the primary field variable is approximated by using simple polynomial shape functions. For the BEM, a boundary integral formulation is used to describe the primary field variable and only the boundaries of the problem domain are discretized. As both of them use small elements to describe the problem geometry, the geometrical complexity of the problem is not the decisive factor in the performance of the methods for most of the practical applications. The performance is mainly driven by the number of elements and associated degrees of freedom in the system. The discretization should be fine enough to correctly predict the behavior of the acoustic waves. As the frequency increases, the number of elements should also be increased to capture the changing nature of the waves. This eventually affects the computational cost and restricts the practical applicability of these methods to low frequencies.

High-frequency range The system behavior at high frequencies changes drastically as compared to low frequencies. The wave field becomes highly complex and the effect of variability becomes more important. The computational cost to capture this behavior using deterministic methods becomes too high and for some applications, deterministic results do not provide meaningful data. Instead, methods that take into account the statistical or asymptotic behavior of the systems are used. The most commonly used method for engineering applications at high frequencies is the Statistical Energy Analysis (SEA) [90]. For room acoustic simulations, methods based on geometrical acoustics are preferred, such as the image source method [54] or ray tracing methods [144].

SEA predicts the spatial average of the energy level. The full system is divided into subsystems and the energy flow between them is calculated. These calculations are based on coupling loss factors between the subsystems while the subsystems are assumed to have a high modal overlap. Although the method is not computationally demanding, the underlying assumptions restrict the use of the method to high frequencies.

The methods based on geometrical acoustics calculate the paths traveled by the sound waves by considering the reflections, scattering effects etc. These paths are assumed to be rectilinear, which provides good approximations when the wavelength is very small as compared to the structures waves interact. Therefore, these methods are better suited for high frequencies.

Mid-frequency range Notwithstanding their shortcomings, the methods for low- and high-frequency regions are widely accepted in the industry and are rather well established. On the other hand, there is a gap between them that is referred to as the mid-frequency region, where low-frequency methods become computationally too expensive and the underlying assumptions of the high-frequency methods are not satisfied. As such, the current widely accepted

methods fail to address the mid-frequency region. This creates a big problem for engineers, because the referred frequency region plays an important role for many practical applications. Since the mid-frequency region exhibits a blend of the wave characteristics from low- and high-frequency regions, there is no clear answer to how to solve the issue. As such, there are different strategies to bridge the gap between low- and high-frequencies:

- Enhancing the computational efficiency of the deterministic methods, such that the frequency range that they can address is extended. There have been various works on the improvement of the FEM, either from the optimization of the modeling process side [17, 69, 107] or by changing the underlying formulations [7, 22, 46, 47]. It is also possible to use iterative solvers and parallelization to speed up the solving process [40] and its combination with decomposition of the FEM domain [48]. For the BEM, it is possible to use approximations of the far field elements in combination with an iterative solver and enhance the method's efficiency, e.g. the Fast Multipole BEM (FM-BEM) [51, 58]. While the aforementioned enhancements concentrate on improving the commonly used methods, there is a new family of approaches called Trefftz methods [127, 105], which aim to tackle the problem fundamentally different than the element based methods. The Wave Based Method [38], which constitutes the basis of this thesis, belongs to those. The method uses *a priori* knowledge of the field to build its system of equations and has a small model size. As such, it provides an efficient solution which makes it suitable for mid-frequency problems.

- Relaxing the underlying assumptions of the high-frequency methods, such that they can be used for the mid-frequency region. For the SEA, the parameters can be updated by using accurate data from deterministic methods [108]. For the geometrical acoustics methods, enrichment of the asymptotic solutions by polynomial functions helps reducing the minimum addressable frequency [23].

- Creating hybrid methods to use the information from low- and high-frequency methods and blend them to bridge the mid-frequency gap. An example is the combined Finite Element Geometrical Acoustics method [4], where the results from both methods are averaged for the mid-frequency region. Another example is the hybrid Finite Element/Statistical Energy Analysis Method [91], where the components with high modal density are modeled with SEA and the components with low modal density are modeled with FEM.

Despite all the efforts summarized above, no method has emerged as a widely accepted solution to the mid-frequency problem yet. Moreover, even the most established methods for the low-frequency range have their shortcomings. In addition to their high computational cost for higher frequencies, they exhibit interpolation and pollution errors in representing the field [17]. They also need

considerable effort in the pre-processing stage to discretize the problem domain or boundary. With increasing frequency, the discretization has to be refined. As for the high-frequency methods, they rely on the accurate data that comes from deterministic methods in order to be applicable over a wider frequency range.

The shortcomings of the low-frequency methods are further exposed for certain problem settings. Inclusion and multiple scattering problems, which are instrumental for various engineering fields, are among those and pose challenges of their own. Here, inclusion problems refer to the cases where an obstacle or more are in interaction with a bounded domain. Multiple scattering problems refer to the cases where two or more obstacles are in interaction in an unbounded field. These specific problem settings can be quite challenging, especially for domain discretization methods such as the FEM. A geometrically complex inclusion may drive the discretization criteria and may lead to long calculation times. Multiple scatterers that are well separated make it difficult to apply absorbing boundary conditions. For certain optimization problems; for instance, when a designer wants to decide on the optimal position of an acoustic treatment in a room, the requirement for remeshing the domain for each iteration introduces a considerable disadvantage.

To conclude, the challenges in numerical modeling of acoustic problems are many and in varying nature. These challenges are inherited by inclusion and multiple scattering problems as well. While the ever advancing computational power extends the limits of possible application cases, there is still a need for faster, more accurate and more user friendly numerical methods that can predict the acoustic field over a wide frequency range.

1.3 Research objectives and achievements

The research objectives of this dissertation are set in light of the challenges described in the previous section with the emphasis on the mid-frequency problem. The research on the Wave Based Method (WBM), which was initiated by Desmet [38], has been going on for over a decade with the aim of creating an alternative method to element based methods that can bridge the mid-frequency gap. The WBM uses *a priori* defined expansions of functions that exactly satisfy the governing equation(s) to represent primary field variable(s). This approach, as opposed to element based methods that use simple polynomial shape functions, does not introduce pollution errors (as described in [17]) at higher frequencies. Moreover, it is a meshless method that can be refined for higher frequencies effortlessly, which saves a considerable time in the preprocessing step.

The main disadvantage of the WBM is that its practical applicability is limited to moderately complex geometries. This limitation stems from an intrinsic property of the method. For the WBM to converge, the problem domain has to be convex or it has to be divided into convex subdomains. However,

following a FEM-like approach of fine discretization makes the WBM lose its efficiency. Because of this drawback, the inherent advantages of the WBM over the element based methods have only been exploited in limited cases. As such, the method has not yet fulfilled its full potential.

The objectives of this dissertation are to extend the problem configurations for which the WBM can be effectively used and exploit its advantages on large-size mid-frequency problems. In order to meet these objectives, a dual research goal has been defined:

Assessment and enhancement of the WBM and the Multi-level WBM As explained above, the WBM has its limitations in terms of showing its efficiency for geometrically complex problems. On the other hand, there are numerous practical applications where it can be used efficiently, especially with its recent Multi-level extension. The Multi-level WBM (ML-WBM) was developed to relax the geometrical requirements for inclusion [136] and multiple scattering problems [133]. When the (ML-)WBM is used for the right application, the method outperforms the element based methods in computational efficiency and brings various practical advantages. As such, the first goal of this dissertation is to assess the advantages of the available WBM technologies and enhance them within their own framework.

Relaxing the geometrical requirements of the WBM There has been progress over the years to relax the geometrical requirements for the WBM framework. The hybrid Finite Element - Wave Based Method [137] was developed to deal with bounded acoustic problems with fine details on the boundaries, such that the FEM can be used to model the exterior details and large, simple acoustic subdomains can be modeled with the WBM inside the FEM domain. For unbounded problems, the hybrid FE-WBM can be used similar to Dirichlet-to-Neumann map (DtN) for the FEM [11]. Apart from the hybrid FE-WBM, the ML-WBM also relaxes the geometrical requirements for inclusion and multiple scattering problems. While both methods are successful in their target applications, they fail to efficiently address bounded problems with complex inclusions or multiple scattering problems with geometrically complex scatterers. As such, the second goal of this dissertation is to develop new techniques that extend the practical applicability of the WBM.

In light of the dual research goal, the following achievements have been accomplished:

- The WBM is applied on a room acoustics case and compared with another mid-frequency method, the Fast Multipole BEM (FM-BEM). In addition, it is compared with measurements and a ray tracing method. As such, its performance is assessed for a large-size problem in the mid-frequency range.

- Symmetric boundary conditions in Cartesian coordinates are derived for the ML-WBM for 2D and 3D multiple scattering problems. Consequently, the range of the models that the ML-WBM can tackle efficiently is extended.
- The ML-WBM is used in shape and topology optimization scenarios for acoustic problems. Acoustic lenses are chosen as the target application. The conceptual advantages of using the ML-WBM in such design scenarios are demonstrated.
- By using the ML-WBM in shape and topology optimization scenarios, innovative 2D and 3D acoustic lenses are designed. For topology optimizations, the lenses are made up of Helmholtz resonators. Scatterers from a predefined periodic distribution are eliminated to form new topologies that focus the sound at a given point and a given frequency. As for the shape optimizations, the distribution of periodic scatterers is kept the same and the shape of the unit scatterer, together with the lattice parameters are optimized to focus sound. Both approaches result in innovative designs, which comprise lenses with varying unit scatterer shapes, as opposed to the current acoustic lens designs in literature, which are made up of circular scatterers.
- A hybrid Boundary Element - Wave Based Method is developed for the efficient solution of inclusion and multiple scattering problems. The hybrid method combines the best of the two worlds. It benefits from the efficient solution of the WBM for simple scatterers or cavities and it uses the flexibility of the BEM for complex scatterers or inclusions. The method is derived for 2D and 3D problems and benchmarked against most commonly used element based methods.

1.4 Outline of the dissertation

This dissertation comprises eight chapters. Chapters 1 and 2 set the theme and background of the presented research and give a summary of the broader scientific context. Chapters 3 to 7 present key scientific contributions. Chapter 8 concludes this dissertation and suggests possible future topics.

Chapter 1 The present chapter discusses the importance of acoustics and the role of CAE tools. The challenges for the numerical modeling methods are explained and in accordance with these challenges, the goals and achievements of this dissertation are presented.

Chapter 2 An overview of the state-of-the-art methods related to the work in this dissertation is provided. Special attention is paid to the WBM, as the method forms the basis for the advancements presented in this dissertation.

Recent advancements in the field to mitigate the mid-frequency problem are discussed.

Chapter 3 A novel application of the WBM on a room acoustics case is presented, where the method's efficiency is assessed by comparing it to the FM-BEM's. The method's accuracy is also compared with measurements and a ray tracing method. As such, this chapter motivates further development of the WBM by demonstrating its potential.

Chapter 4 The theory of the ML-WBM is reviewed and the method is enhanced by deriving symmetric boundary conditions. The derivations are done for both 2D and 3D problems. As such, this chapter forms the theoretical background for Chapter 5, where the ML-WBM is applied on acoustic lens design.

Chapter 5 Novel acoustic lens designs are presented by using the ML-WBM as the numerical modeling method. Firstly, a novel optimization procedure is proposed, where the shape of the unit scatterer and the lattice parameters are optimized. Subsequently, a well known design procedure for acoustic lenses is followed, which optimizes the topology of an acoustic lens by eliminating scatterers. By using a Helmholtz resonator as the unit scatterer, the designs are improved as compared to their counterparts in literature, which use circular scatterers. The improvement is demonstrated for 2D and 3D acoustic lenses.

Chapter 6 A hybrid Boundary Element - Wave Based Method is derived for bounded problems with inclusions and multiple scattering problems. The conceptual advantages of the method and how it fits into the current WBM framework are discussed. The domain decomposition procedure, which lays the foundation of the hybrid method is presented for bounded and unbounded problems. The detailed derivation of the hybrid method and the resulting coupling matrices are given.

Chapter 7 The derived hybrid Boundary Element - Wave Based Method is applied to six different numerical verification cases. The first three examples are multiple scattering problems and the latter three are bounded problems with inclusions. The accuracy of the method, with emphasis on coupling algorithms, is tested. The hybrid method is benchmarked against the BEM and the FM-BEM for unbounded problems and against the FEM for the bounded problems.

Chapter 8 The presented work is summarized and conclusions are drawn. Topics for future research are suggested.

Chapter 2

State-of-the-Art in deterministic modeling of acoustic problems

This chapter aims to provide the relevant background in order to position the contributions of the dissertation. The chapter starts with the mathematical description of the problem under consideration. Subsequently, a short survey of the state-of-the-art is given. The most common element based methods with their recent enhancements are presented, which are followed by a short review of Trefftz methods. A detailed explanation of the Wave Based Method is given to form the basis of the following chapters. Finally, the properties of the Finite Element Method, the Boundary Element Method and the Wave Based Method are compared and the chapter is concluded.

2.1 Mathematical description of the problem

The problem under consideration, shown in Figure 2.1, is a steady-state acoustic problem, where the acoustic pressure field $p(\vec{r})$ is governed by the inhomogeneous Helmholtz equation:

$$\nabla^2 p(\vec{r}) + k^2 p(\vec{r}) = -j\rho_0 \omega \delta(\vec{r}, \vec{r_q}) q, \tag{2.1}$$

with ∇^2 the Laplace operator, k the acoustic wave number, δ the Dirac-delta function, ρ_0 the fluid density, ω the angular frequency and q a volume velocity source strength. For unbounded problems, the problem boundary Γ consists of 2 parts: the finite part of the boundary, Γ_b, and the boundary at infinity, Γ_∞. For bounded problems, only Γ_b exists. Based on the three types of commonly applied acoustic boundary conditions, the finite boundary can be

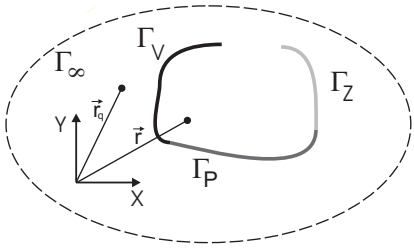

Figure 2.1: A 2D unbounded acoustic problem

further divided in three non-overlapping parts: $\Gamma_b = \Gamma_v \cup \Gamma_p \cup \Gamma_Z$. If one defines the normal velocity operator $\mathcal{L}_v(\bullet)$ as:

$$\mathcal{L}_v(\bullet) = \frac{j}{\rho_0 \omega} \vec{\nabla}(\bullet) \cdot \vec{n}, \tag{2.2}$$

where $\vec{n}$ is the normal vector, the boundary residuals can be written as:

$$\vec{r} \in \Gamma_v : R_v(p(\vec{r})) = \mathcal{L}_v(p(\vec{r})) - \overline{v}_n(\vec{r}) = 0, \tag{2.3}$$

$$\vec{r} \in \Gamma_p : R_p(p(\vec{r})) = p(\vec{r}) - \overline{p}(\vec{r}) = 0, \tag{2.4}$$

$$\vec{r} \in \Gamma_Z : R_Z(p(\vec{r})) = \mathcal{L}_v(p(\vec{r})) - \frac{p(\vec{r})}{\overline{Z}_n(\vec{r})} = 0. \tag{2.5}$$

The quantities $\overline{v}_n$, $\overline{p}$ and $\overline{Z}_n$ represent the imposed normal velocity, pressure and normal impedance, respectively. At the boundary at infinity, Γ_∞, the Sommerfeld radiation condition for outgoing waves is applied. This condition ensures that no acoustic energy is reflected at infinity and is expressed as:

$$\vec{r} \in \Gamma_\infty : R_\infty(p(\vec{r})) = \lim_{|\vec{r}| \to \infty} \left(|\vec{r}|^{\frac{d-1}{2}} \left(\frac{\partial p(\vec{r})}{\partial |\vec{r}|} + jkp(\vec{r}) \right) \right) = 0, \tag{2.6}$$

where d is equal to 2 or 3 for two-dimensional (2D) problems and three-dimensional (3D) problems, respectively. The Helmholtz equation (2.1), together with the associated boundary conditions (2.3), (2.4), (2.5) (and (2.6) for unbounded problems) yields a fully defined mathematical formulation of the acoustic pressure field $p(\vec{r})$.

2.2 Element based methods

The most commonly used element based methods for acoustic problems are the FEM and the BEM. The FEM is the most preferred method for bounded

problems while the BEM is the most preferred for unbounded problems. The following subsections present the general principles of the methods together with various enhancements to their conventional forms.

2.2.1 The Finite Element Method

The FEM is an element based method which requires the discretization of the problem domain into a large number of small, non-overlapping elements. The FEM system is constructed by writing a weak form of the governing partial differential equation with boundary conditions. The weak form involves weighting functions which can be chosen arbitrarily and basis functions of the field variables. A linear combination of (in general) simple polynomial shape functions is used as the basis function set. These shape functions are defined within each element through the nodes, as an approximation to the exact solution of the Helmholtz equation. Following a Galerkin procedure, the weighting functions are chosen the same as the basis functions. Subsequently, the numerical discretization of the weighted residual formulation yields a set of linear equations, which form the FEM matrices.

Because of the use of simple polynomial shape functions, a fine discretization is needed in order to accurately represent field variables and decrease the interpolation error. In addition to the interpolation error, pollution errors are also introduced because of the mismatch between the physical and numerical wavelenghts [17]. This leads to a shift in the resonance frequencies of the system as compared to an exact solution. While for low-frequency applications, the effect is negligible, for mid-frequency problems it becomes the dominant source of error [17].

The FEM in its conventional form is a direct method, i.e. the unknowns of the system have a direct physical meaning; in the case of acoustics, nodal pressure values. In order for the FEM to solve unbounded problems, special boundary conditions need to be defined to satisfy the Sommerfeld radiation condition (2.6). Various ways of ensuring this condition are reviewed in [68, 125]. One common approach is called Perfectly Matched Layers, where extra elements are added to the FEM mesh that absorb incoming waves and avoid reflections at external boundaries [116]. Another common approach is called Dirichlet to Neumann Map (DtN) method. This method defines a mapping from pressure to velocity data on the external boundary and simulates the radiation of the waves through analytic solutions [55]. As the FEM is a widely known method, further details of the method are omitted here. A comprehensive review can be found in [153]. Moreover, a general comparison of the properties of the FEM with the BEM and the WBM is presented in Section 2.5.

2.2.2 Enhancements to the FEM

Although the FEM is the most commonly used method for bounded problems, it has its shortcomings as well. Over the years, substantial research efforts have been spent to enhance the method. The enhancements may come in various forms with different goals. While most of them target increasing the efficiency of the method, some aim to decrease the inherent errors of the method or to ease the preprocessing step. An extensive overview of the advances in FEM can be found in [68] and also in [125]. Here, a brief overview is given for selected methods.

Iterative solvers The size of the FEM matrices can be very large, especially for mid-frequency problems. It is possible to economize on the matrix solving cost by using iterative solvers. The FEM matrices are sparse and symmetric, which makes it possible to use specialized solvers. Most common iterative methods are based on a Krylov subspace which is an orthogonal vector space that is refined in each iteration until a satisfactory solution is gathered. An important note about iterative solvers is that, most of the time they rely on problem specific preconditioners to ensure convergence and good efficiency. Comparisons of different iterative methods and preconditioners can be found in [78, 41, 10]. While it is possible to apply iterative solvers on the conventional form of the FEM, various enhancements to the core FEM formulations rely on iterative solvers as well, as detailed in the following categories.

Multigrid FE methods Multigrid methods are built upon the principle of using coarser meshes that are computationally cheap to capture the general behavior of the system, while using finer meshes to resolve the oscillatory behavior. A general category of the methods that use a similar philosophy is called multiscale methods. The difference between the multiscale and multigrid FE methods is that, the latter rely on coarser and finer discretizations of the FE domain, while multiscale methods refer to a more general setting and may benefit from enriched sets. As such, the ones that use enriched basis sets are listed in the next category.

Multigrid FE methods are based on iterative solvers. There are various studies on finding high performance preconditioners [2, 39, 42]. While the solution time can be effectively decreased with these methods, the need for a set of different level of discretizations and pollution errors coming from the coarser meshes harm the practical applicability of the method.

Basis function enrichments Simple polynomial shape functions used in the conventional FEM formulations bring the requirement of fine discretization of the problem domain, in order to accurately capture the harmonic behavior of the field. This requirement leads to larger systems with increasing frequency and makes the FEM lose its appeal for mid-frequency problems. One way

to decrease the required number of elements per wavelength is by enriching the basis function set with special functions. Various methods have followed this route and have enriched the basis function set with plane waves to extend the practical frequency limits of the FEM. The Partition of Unity FEM (PUFEM) [97], The Discontinuous Enrichment Method (DEM) [46, 123], The Discontinuous Galerkin Method (DGM) [47, 50] are some of the known examples. It should be noted that some of these methods incorporate the principles of the Trefftz methods and are also mentioned in Section 2.3.

The PUFEM multiplies the polynomial shape functions with plane waves to enrich the basis set, while the inter-element continuity is inherently satisfied. The DEM, on the other hand, applies the plane wave enrichment differently, such that Lagrange multipliers are introduced to enforce a weak continuity of the solution across the element interfaces. The polynomial basis and the enrichment basis correspond to different scales of the problem. As such, it is a multiscale approach. For problems with plane wave excitation and sound-soft, sound-hard boundary conditions, the polynomial basis of the DEM can be dropped, which leads to the DGM.

For most of the plane wave enriched FEM formulations, the problem is that they lead to inherently ill-conditioned systems. As such, care must be taken when applying the enrichments. An improvement over the PUFEM is a method called generalized FEM (GFEM)[119, 120, 121], which uses a combined FEM-PUFEM approach to overcome the ill-conditioning of the system matrices. The FEM part is used for the coarse scale and plane wave enriched PUFEM part is used for the fine scale. However, the integration schemes become very important for the success of the method and the pollution errors are still in effect [120].

Domain decomposition methods The main motivation of domain decomposition methods is to divide the large problem domain into small non-overlapping subdomains in order to effectively use parallelization. The Component Mode Synthesis (CMS) [101], the Finite Element Tearing and Interconnecting Method for Helmholtz problems (FETI-H) [49, 44] which is a dual variable method and its variant with dual-primal variables, FETI-DPH [45, 99], are prominent examples for domain decomposition methods.

The CMS uses modal representations of its components and connects them by using static or dynamic constraint modes on the interfaces. As the interaction between the components is represented by the constrained modes on the interfaces, the normal modes of the components are eliminated during the system assembly. As such, the CMS shows its efficiency for the systems that can be divided into large components with small interface connections.

The FETI-H method is an iterative substructuring method, which couples the decomposed domains through Lagrange multipliers defined on the interfaces. The primary degrees of freedom are eliminated which makes the Lagrange multipliers the only unknowns of the system. A preconditioner is used for the iterative solver, which is obtained from the solution of a coarse problem

with plane waves. The FETI-DPH improves the FETI-H by keeping the primal variables at subdomain corners. It has a better performance and allows massive parallelization of the problem. While the FETI methods provide fast solutions, they need a longer preprocessing step as compared to the FEM because of the decomposition of the domain meshes.

Fast frequency sweep algorithms Most of the engineering applications require the calculation of the response over a wide frequency range. Calculating the frequency response with small incremental steps is time consuming. The main idea of fast frequency sweep algorithms is to calculate the response on a selection of points and extrapolate the frequency response by using the derivative of the solution. A considerable speed-up can be achieved by using these methods [6, 87]. However, the best performance is obtained for systems with rather smooth response characteristics. As such, interior problems with low impedance may not benefit from these algorithms, especially at higher frequencies, where the modal density is increased.

2.2.3 The Boundary Element Method

The BEM is an element based numerical prediction technique which utilizes the boundary integral equation to relate field variables in the continuum domain to boundary variables on the boundary of the problem geometry. As such, the BEM needs only the discretization of the boundary into small elements as compared to the domain discretization of the FEM. There are various BEM formulations in literature, which are summarized in [149]. The most commonly used ones are the direct collocation formulation [18] and the indirect variational formulation [67] (which is also referred to as the Symmetric Galerkin BEM [15]). In its direct form, the boundary variables are the pressure and velocity. In its indirect form, the boundary variables are designated as the difference of the pressure and the difference of the normal derivative of the pressure between both sides of the boundary surface [67]. These variables are named as double layer potential, μ, and single layer potential, σ, respectively. The indirect formulation allows modeling of open boundaries (in other words zero thickness boundaries), while the direct formulation requires fully closed boundaries. As such, the direct formulation can be used either on an interior or an exterior problem at a time.

The BEM uses Green's kernel functions in its representation of the field variables. The Sommerfeld radiation condition is always inherently satisfied. As such, the BEM solves unbounded problems without any extra treatment. This property of the BEM, together with its boundary-only discretization requirement makes it the most popular method for the solution of unbounded problems.

The general properties of the method is further discussed in Section 2.5, together with its comparison to the FEM and the WBM. A detailed derivation of the method can be found in [149].

2.2.4 Enhancements to the BEM

While the BEM is the most commonly used method for unbounded problems, there are issues regarding the efficiency of the method in its conventional form, especially for large-size problems in the mid-frequency range. In addition, for unbounded problems with closed boundaries, the solution is not unique at the resonance frequencies of the internal domain. This leads to additional errors at those frequencies, if care is not taken. Therefore, various enhancements to the core BEM formulations have been done over the years to increase the efficiency of the method while some concentrated on avoiding fictitious frequencies. The most common ones are listed as follows:

Fast Multipole BEM The Fast Multipole Boundary Element Method (FM-BEM) [51, 58, 112] yields a fast, approximate solution to the conventional BEM. The key idea of the Fast Multipole approach is that the interactions between all elements in the full system matrix are split into far field interactions and near field interactions. The near field interactions are incorporated using the conventional BEM matrix. The far field interactions are not obtained point-to-point, as in the conventional BEM, but for clusters of source-receiver points that are sufficiently far enough from each other. This approximation, together with the use of iterative solvers allows the FM-BEM to be efficiently applied on large-size problems in the mid-frequency range. The computational complexity of the problem becomes on the order of $\mathrm{O}(N \log N)$, instead of the order of $\mathrm{O}(N^2)$ to $\mathrm{O}(N^3)$ for a standard BEM. While the FM-BEM is already widely accepted in the engineering community, the practical application of the method has some limitations. To be more specific, the calculation of the multi-pole algorithms is costly, which makes the setup time long. As such, when applied on small-size problems, the FM-BEM is computationally more expensive than a standard BEM. Special care is also needed for low-frequency problems. As such, dedicated algorithms should be used to ensure the convergence of the iterative solvers [57].

H-Matrices A Hierarchical matrix (H-Matrix) refers to a block-structured matrix that comprise low-rank submatrices [9]. By using low-rank approximations to the matrix partitions, it is possible to get fast matrix-vector products and get data-sparse approximations to non-sparse matrices. When applied on the BEM for acoustic problems, these approximations result in a similar structure to the FM-BEM, i.e. the far away elements are approximated. The difference of H-matrix methods is that they don't require specialized analytical expressions for different kernel functions, as opposed to dedicated multi-pole expressions of the FM-BEM's. They can be used as black box algorithms. A

study on comparison of H-matrices to the FM-BEM shows that the performance of the two are comparable, however the result depends on the application case [19]. A general observation is that the setup time needed for H-matrices is longer as compared to the FM-BEM, however H-matrices yield faster vector-matrix multiplications, which can result in faster total solution times for certain applications.

Boundary Element Tear and Interconnecting Method The Boundary Element Tear and Interconnecting (BETI) [86] Method follows the footsteps of the FETI. The problem domain is decomposed into several non-overlapping subdomains. The global continuity is enforced through Lagrange multipliers on the interfaces. By eliminating the original degrees of freedom and applying an iterative solving procedure, a method that is suitable for easy parallelization is obtained. One advantage of the BETI is its ability to model heterogeneities when they are in the form of piecewise smooth media. However, the BETI requires special treatments for stability and the coupling of the BETI and the Fast Multipole Method for efficient solution of Helmholtz problems is still to be done [118].

Wave Boundary Elements The Wave Boundary Elements (WBE) [100] is based on the idea of enriching the basis function set to economize on the number of elements needed to accurately solve the problem. As such, it follows the philosophy of the PUFEM. The polynomial shape functions are multiplied with plane waves within each element to enrich the basis set. The unknowns of the system become the amplitudes of the corresponding plane waves. With such an enrichment, a low discretization level of 2.5-3 degrees of freedom per wavelength can be achieved [14]. However, the resulting system is inherently ill-conditioned, as such a careful handling of the problem is essential for the success of the method. A balance has to be found in the number of added plane waves, as doing so increases the accuracy while negatively affecting the ill-conditioning of the system.

Iterative solvers The solution of the BEM matrices is expensive for large-size problems. Although the boundary-only discretization makes the resulting system smaller as compared to the FEM, the fully populated and complex nature of the BEM matrices makes it less favorable. It is possible to use iterative solvers to speed up the solving time. However, special care needs to be taken to ensure the convergence of the solvers [129]. Because of the aforementioned properties of the BEM matrices, classic iterative schemes like Jacobi and Gauss-Seidel either do not converge or show low convergence rates. The class of iterative solvers based on conjugate gradient (CG) method are preferred because of this reason [130, 131]. Among those, generalized minimal residual (GMRES) and bi-conjugate gradient (Bi-CG) have shown good performance. Nevertheless, a good preconditioner is needed most of the time to gain good results. The use of iterative solvers is especially vital for the FM-BEM, H-

Matrices and BETI methods. A general comparison of different iterative methods can be found in [93].

Treatment of fictitious frequencies In order to suppress the errors at fictitious frequencies, various techniques have been proposed. The treatments are different for direct and indirect formulations. For the direct collocation formulation, the Combined Helmholtz Integral Equation Formulation (CHIEF) method [115] is the most common one. The basic idea is to define over-determination points inside the cavity to make the system more stable at the resonance frequencies. One should be careful about the number of points added and their locations because the success of the method heavily depends on them. While the CHIEF method adds extra terms to the basic formulation, it is also possible to define a new formulation, as it is done in the Burton and Miller method [20] . The basic idea is to modify the boundary integral equation by adding the normal derivative of itself. This combined formulation makes the problem definition unique and avoids fictitious frequencies. However, the cost is high because of the added terms and care must be taken for the resulting hyper-singular formulation. For the indirect formulation, assigning impedance boundary conditions to the surface inside the cavity creates a formulation similar to the Burton and Miller's and makes the problem unique. Doing so doubles the number of degrees of freedom in the system, however applying the impedance boundary condition on a subset of the elements has shown to save computational cost while still effectively mitigate the fictitious resonance problem [32].

2.3 Trefftz Methods

Element based methods are widely used and have become an industry standard through commercial packages. However, the intrinsic requirement to preprocess the problem domain/boundary through mesh generation and the possible high computational cost for the mid-frequency range remain problematic for the end-users. These issues have led to the rise of a family of meshless approaches called Trefftz methods [127, 105]. The main idea behind these methods is to use *a priori* knowledge of the field to represent the main variables, in the form of function expansions that exactly satisfy the governing equation. As such, it is possible to represent the field with lower degrees of freedom as compared to element based method. The very first idea was proposed by Trefftz [127] in 1926. It was decades later that his ideas were picked up again to create a new research area on the development of alternative deterministic methods to element based methods.

A general classification of Trefftz methods can be found in [79], where different formulations to build up the system of equations are detailed, e.g. collocation, least squares or Galerkin weighted residual formulations. In addition, direct and indirect representations of the primary variables are discussed. A

comprehensive review of available Trefftz methods can be found in [105]. Here, a selection of prominent examples is highlighted.

Various Trefftz methods use distributions of sources inside/outside of boundaries to represent the field. The sources are mainly chosen as monopoles. The Equivalent Source Method [81], the Method of Fundamental Solutions (MFS) [43, 8] and the Full-Field Method [98] are some examples. The number and distribution of the sources are the deciding factors for the success of these methods, so they should be chosen carefully. Singularities may rise when the sources are placed on the boundaries. To avoid these singularities, some methods use a non-singular basis set that is called radial basis functions. Some examples are the Boundary Knot Method [24] and the Kansa's Method [77]. While they avoid singularities, they require the definition of extra source positions inside the domain because the RBFs are not exact solutions of the governing equation.

Some Trefftz approaches decompose the domain into subdomains to apply *a priori* defined function sets. The coupling of the subdomains can be done in various ways. Direct coupling algorithms favor relating the pressure and velocity terms or a combination of them. It is also possible to introduce auxiliary variables on the interfaces [47]. Variational Theory of Complex Rays [109, 82] is an example of domain decomposition methods. A set of plane waves are defined for each subdomain and the system is built through a variational formulation. The Wave Based Method falls also into this category and is detailed in the next section.

There are also various methods in literature, where Trefftz approaches are coupled to element based methods. The categorization of these hybrid approaches is difficult because of their varying nature. For instance, some of the basis function enrichment methods presented in Section 2.2.2 incorporate principles of the Trefftz methods to element based methods. As such, they can be considered as hybrid Trefftz-element based methods. However, the coupling defined here refers to the coupling of two distinct methods, which are used to model different parts of the physical problem. The hybrid FE-WBM [137], which is detailed in the next section, and the hybrid BE-WBM, which is presented in Chapter 6 fall into this category. Another example is coupling of the MFS and the BEM [122]. It is also possible to couple two Trefftz methods, as in coupling of the MFS and Kansa's method [56]. These hybrid methods follow the philosophy of combining the best of the two worlds.

A common drawback of almost all Trefftz methods is the inherent ill-conditioning of the system matrices [152]. This stems from the highly oscillatory nature of the basis function sets. When the wave field becomes complicated and more functions are needed to represent it accurately, the ill-conditioning becomes more pronounced.

As it is shortly summarized above, there are numerous Trefftz methods available in literature. The distinguishing factors among them are generally the selection of the unique basis function sets and the different formulations to build up the

system of equations. The WBM's proposed function set includes evanescent waves in addition to the commonly used propagating waves, which gives it a distinction. Moreover, a Galerkin weighted residual formulation is used on the boundaries, which helps reducing the overall error more effectively as compared to least squares or collocation formulations [79].

2.4 The Wave Based Method

The Wave Based Method (WBM) is a deterministic numerical modeling technique for the analysis of steady-state dynamic problems. It has been developed as an alternative to element based methods and follows an indirect Trefftz approach. It uses *a priori* defined expansions of functions called wave functions to represent the dynamic field variables. Unlike the simple polynomial shape functions used by element based methods, the wave functions exactly satisfy the governing equations.

For bounded problems, a sufficient condition for the WBM to converge is the convexity of the considered domain [38] or that the domain is decomposed into convex subdomains. The main strategy in the decomposition process is to end up with a rather small number of large subdomains [105]. Following a FEM like approach and dividing the domain into very small parts introduces extra interfaces in the domain and eventually causes the WBM to lose its efficiency. For this reason, the method is more suitable for problems of moderate geometrical complexity.

For unbounded problems, an artificial boundary is drawn to separate the field into bounded and unbounded domains. Different types of wave function sets are defined to represent each. The conventional WBM uses a global circular truncation line or spherical surface Γ_t^g which encloses all the geometry at once, as shown in Figure 2.2.

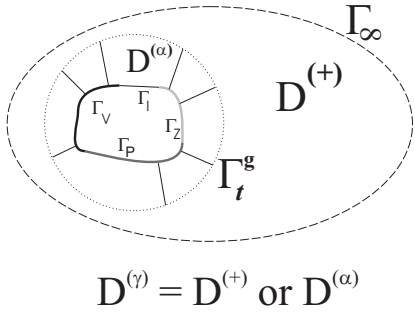

Figure 2.2: Graphical representation of the WBM modeling concept for unbounded problems

The partitioning of the domain by following the above given guidelines constitutes the first step in the WBM modeling. The general model construction can be summarized in four main steps:

A. Partitioning into subdomains.

B. Selection of the appropriate wave functions in the pressure expansion.

C. Construction of the system of equations using a weighted residual formulation of the boundary and continuity conditions.

D. Solution of the system of equations and postprocessing of the dynamic variables.

The unknowns of the WBM system are the wave function contribution factors. Since the unknowns are not physical quantities, the method is referred to as an indirect Trefftz method.

2.4.1 Field variable expansion

In the considered problem, the primary field variable is the steady-state acoustic pressure $p(\vec{r})$ and it is approximated by a solution expansion $\hat{p}(\vec{r})$. Depending on the acoustic subdomain, $D^{(\gamma)}$, the acoustic pressure is approximated as:

$$p^{(\gamma)}(\vec{r}) \simeq \hat{p}^{(\gamma)}(\vec{r}) = \sum_{w=1}^{n_w^{(\gamma)}} \Phi_w^{(\gamma)}(\vec{r}) t_w^{(\gamma)}(\vec{r}) + \hat{p}_f^{(\gamma)} = \Phi^{(\gamma)}(\vec{r})\, t^{(\gamma)} + \hat{p}_f^{(\gamma)}(\vec{r}), \quad \vec{r} \in D^{(\gamma)}. \tag{2.7}$$

In this general form, γ is the corresponding number of the WBM subdomain, $D^{(\gamma)}$. The functions $\Phi_w^{(\gamma)}$ represent *a priori* defined wave functions and $t_w^{(\gamma)}$ are their corresponding contribution factors, $n_w^{(\gamma)}$ is the number of wave functions within subdomain $D^{(\gamma)}$. $\Phi^{(\gamma)}$ is the row vector collecting wave functions and $t^{(\gamma)}$ is the column vector collecting weighting factors. The selection of the wave functions differs for solving bounded and unbounded problems. For this reason, γ represents a general WBM subdomain and is replaced with α for bounded subdomains, $D^{(\alpha)}$, and with + to represent an unbounded domain, $D^{(+)}$, as it is shown in Figure 2.2 . Finally, $\hat{p}_f^{(\gamma)}$ represents a particular solution resulting from acoustic source terms q in the right hand side of the inhomogeneous Helmholtz equation (2.1).

Wave functions for 2D bounded problems

The wave functions are selected in a way that they exactly satisfy the homogeneous form of the Helmholtz equation (2.1). For 2D bounded subdomains, wave functions are separated into two sets called the r- and the

s-set:

$$\sum_{w=1}^{n_w^{(\alpha)}} \Phi_w^{(\alpha)}(\vec{r}) t_w^{(\alpha)} = \sum_{w_r=1}^{n_{w_r}^{(\alpha)}} \Phi_{w_r}^{(\alpha)}(\vec{r}) t_{w_r}{}^{(\alpha)} + \sum_{w_s=1}^{n_{w_s}^{(\alpha)}} \Phi_{w_s}^{(\alpha)}(\vec{r}) t_{w_s}{}^{(\alpha)}, \tag{2.8}$$

with (α) being the corresponding number of the bounded subdomain $D^{(\alpha)}$ and $n_w^{(\alpha)} = n_{w_r}^{(\alpha)} + n_{w_s}^{(\alpha)}$. These wave functions are defined as:

$$\Phi_w^{(\alpha)}(\vec{r}(x,y)) = \begin{cases} \Phi_{w_r}^{(\alpha)}(x,y) = \cos(k_{xw_r}^{(\alpha)} x)\, e^{-jk_{yw_r}^{(\alpha)} y}, \\ \Phi_{w_s}^{(\alpha)}(x,y) = e^{-jk_{xw_s}^{(\alpha)} x}\, \cos(k_{yw_s}^{(\alpha)} y). \end{cases} \tag{2.9}$$

In order for the wave functions (2.14) to be exact solutions of the homogeneous Helmholtz equation, the following equation must hold:

$$\left(k_{xw_r}^{(\alpha)}\right)^2 + \left(k_{yw_r}^{(\alpha)}\right)^2 = \left(k_{xw_s}^{(\alpha)}\right)^2 + \left(k_{yw_s}^{(\alpha)}\right)^2 = k^2. \tag{2.10}$$

With this equation, it is possible to define an infinite number of wave functions (2.14). Desmet [38] proposes to select the following wave number components:

$$\begin{cases} \left(k_{xw_r}^{(\alpha)}, k_{yw_r}^{(\alpha)}\right) = \left(\frac{w_1^{(\alpha)}\pi}{L_x^{(\alpha)}}, \pm\sqrt{k^2 - \left(k_{xw_r}^{(\alpha)}\right)^2}\right) \\ \left(k_{xw_s}^{(\alpha)}, k_{yw_s}^{(\alpha)}\right) = \left(\pm\sqrt{k^2 - \left(k_{yw_s}^{(\alpha)}\right)^2}, \frac{w_2^{(\alpha)}\pi}{L_y^{(\alpha)}}\right) \end{cases} \tag{2.11}$$

with $w_1^{(\alpha)}$ and $w_2^{(\alpha)} = 0, 1, 2, \cdots$. $L_x^{(\alpha)}$ and $L_y^{(\alpha)}$ are the dimensions of the (preferably smallest) rectangular bounding box enclosing the considered subdomain.

Wave functions for 3D bounded problems

For 3D bounded subdomains, wave functions are separated into three sets called the r-, s- and t-set and defined as [38]:

$$\Phi_w^{(\alpha)}(\vec{r}(x,y,z)) = \begin{cases} \Phi_{w_r}^{(\alpha)}(x,y,z) = \cos(k_{xw_r}^{(\alpha)} x)\, \cos(k_{yw_r}^{(\alpha)} y)\, e^{-jk_{zw_r}^{(\alpha)} z} \\ \Phi_{w_s}^{(\alpha)}(x,y,z) = \cos(k_{xw_s}^{(\alpha)} x)\, e^{-jk_{yw_s}^{(\alpha)} y}\, \cos(k_{zw_s}^{(\alpha)} z) \\ \Phi_{w_t}^{(\alpha)}(x,y,z) = e^{-jk_{xw_t}^{(\alpha)} x}\, \cos(k_{yw_t}^{(\alpha)} y)\, \cos(k_{zw_t}^{(\alpha)} z) \end{cases} \tag{2.12}$$

The requirement for (2.12) to be exact solutions of (2.1) is analogous to the 2D case:

$$\begin{aligned} &\left(k_{xw_r}^{(\alpha)}\right)^2 + \left(k_{yw_r}^{(\alpha)}\right)^2 + \left(k_{zw_r}^{(\alpha)}\right)^2 \\ &= \left(k_{xw_s}^{(\alpha)}\right)^2 + \left(k_{yw_s}^{(\alpha)}\right)^2 + \left(k_{zw_s}^{(\alpha)}\right)^2 \\ &= \left(k_{xw_t}^{(\alpha)}\right)^2 + \left(k_{yw_t}^{(\alpha)}\right)^2 + \left(k_{zw_t}^{(\alpha)}\right)^2 = k^2. \end{aligned} \tag{2.13}$$

The following wave number components are proposed [38]:

$$\begin{cases} \left(k_{xw_r}^{(\alpha)}, k_{yw_r}^{(\alpha)}, k_{zw_r}^{(\alpha)}\right) = \left(\frac{w_1^{(\alpha)}\pi}{L_x^{(\alpha)}}, \frac{w_2^{(\alpha)}\pi}{L_y^{(\alpha)}}, \pm\sqrt{\left(k^{(\alpha)}\right)^2 - \left(k_{xw_r}^{(\alpha)}\right)^2 - \left(k_{yw_r}^{(\alpha)}\right)^2}\right) \\ \left(k_{xw_s}^{(\alpha)}, k_{yw_s}^{(\alpha)}, k_{zw_s}^{(\alpha)}\right) = \left(\frac{w_3^{(\alpha)}\pi}{L_x^{(\alpha)}}, \pm\sqrt{\left(k^{(\alpha)}\right)^2 - \left(k_{xw_s}^{(\alpha)}\right)^2 - \left(k_{zw_s}^{(\alpha)}\right)^2}, \frac{w_4^{(\alpha)}\pi}{L_z^{(\alpha)}}\right) \\ \left(k_{xw_t}^{(\alpha)}, k_{yw_t}^{(\alpha)}, k_{zw_t}^{(\alpha)}\right) = \left(\pm\sqrt{\left(k^{(\alpha)}\right)^2 - \left(k_{yw_t}^{(\alpha)}\right)^2 - \left(k_{zw_t}^{(\alpha)}\right)^2}, \frac{w_5^{(\alpha)}\pi}{L_y^{(\alpha)}}, \frac{w_6^{(\alpha)}\pi}{L_z^{(\alpha)}}\right) \end{cases} \tag{2.14}$$

with $w_1^{(\alpha)} \cdots w_6^{(\alpha)} = 0, 1, 2, \cdots$. The dimensions $L_x^{(\alpha)}$, $L_y^{(\alpha)}$ and $L_z^{(\alpha)}$ represent the dimensions of the (smallest) rectangular bounding box, circumscribing the considered subdomain.

The set of wave functions described above constitutes an infinite series of wave-like functions. In order for the WBM to be amenable for numerical implementation, the infinite series expansion needs to be truncated to a finite basis set. A linear, frequency dependent truncation rule is suggested. In short, wave functions that have wave number components smaller than or approximately equal to the truncation factor T times the physical wave number k, are added to the wave function basis set. This results in upper bounds for the integer numbers $w_1^{(\alpha)}$, $w_2^{(\alpha)}$, $w_3^{(\alpha)}$, $w_4^{(\alpha)}$, $w_5^{(\alpha)}$ and $w_6^{(\alpha)}$ in equation (2.14):

$$\frac{w_{1_{max}}^{(\alpha)}\pi}{L_x^{(\alpha)}} \simeq \frac{w_{2_{max}}^{(\alpha)}\pi}{L_y^{(\alpha)}} \simeq \frac{w_{3_{max}}^{(\alpha)}\pi}{L_x^{(\alpha)}} \simeq \frac{w_{4_{max}}^{(\alpha)}\pi}{L_z^{(\alpha)}} \simeq \frac{w_{5_{max}}^{(\alpha)}\pi}{L_y^{(\alpha)}} \simeq \frac{w_{6_{max}}^{(\alpha)}\pi}{L_z^{(\alpha)}} \simeq Tk \tag{2.15}$$

Wave functions for 2D unbounded problems

For the wave function selection of the unbounded domain, the same principle as for bounded wave functions is followed, in that they exactly satisfy the Helmholtz equation. In addition, they are selected in a way that they also implicitly obey the Sommerfeld radiation condition, resulting in a set consisting entirely of outgoing waves. In this way, no extra care should be taken concerning the unboundedness of the problem; it is implicitly represented in the function set chosen for unbounded domains.

As proven by Herrera et al. [71], the exterior pressure $p^{(+)}(r,\theta)$ outside of a truncation circle of radius R resulting from an infinitely long cylinder of radius R with Neumann boundary conditions can be represented with the following solution set [103]:

$$\begin{aligned} p^{(+)}(r,\theta) \simeq \hat{p}^{(+)}(r,\theta) =& H_0^{(2)}(kr)t_{c0} \\ &+ \sum_{n=1}^{n_u} \left(H_n^{(2)}(kr)\cos(n\theta)t_{cn} + H_n^{(2)}(kr)\sin(n\theta)t_{sn}\right), \end{aligned} \tag{2.16}$$

with r and θ being the polar coordinates. $H_n^{(2)}(\bullet)$ is the n-th order Hankel function of the second kind. The contributions t_{c0}, t_{cn} and t_{sn} are determined by the velocity boundary condition. Reorganizing the equation to fit the general wave function form $\hat{p}^{(+)}(\vec{r}) = \sum_{w=1}^{n_w^{(+)}} \Phi_w^{(+)}(\vec{r}) t_w^{(+)}$ yields the following wave function set with $n_w^{(+)} = n_{w_c}^{(+)} + n_{w_s}^{(+)} + 1$:

$$\Phi_w^{(+)}(\vec{r}(r,\theta)) = \begin{cases} \Phi_{w_c}^{(+)}(r,\theta) = H_{w_c}^{(2)}(kr)\cos(w_c\theta), & w_c = 0,1,2,...,n_{w_c}^{(+)}, \\ \Phi_{w_s}^{(+)}(r,\theta) = H_{w_s}^{(2)}(kr)\sin(w_s\theta), & w_s = 1,2,...,n_{w_s}^{(+)}. \end{cases} \tag{2.17}$$

Wave functions for 3D unbounded problems

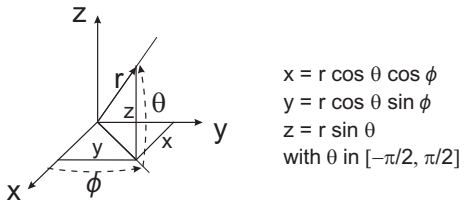

Figure 2.3: Spherical coordinate system definition

For 3D unbounded domains, the problem is considered in spherical coordinates r, θ and ϕ as defined in Figure 2.3. The following multipole series holds as the solution to 3D unbounded problems based on [75]:

$$p^{(+)}(r,\theta,\phi) \simeq \hat{p}^{(+)}(r,\theta,\phi) = \sum_{l=0}^{l_{max}} \sum_{m=-l}^{l} t_{lm}^{(+)} h_l^{(2)}(kr) Y_l^m(\theta,\phi), \tag{2.18}$$

which converges to the exact solution as $l_{max} \to \infty$. In this expression, $t_{lm}^{(+)}$ is a weighting factor, which is determined based on the boundary conditions and $h_l^{(2)}(kr)$ is the spherical Hankel function of the second kind, order l:

$$h_l^{(2)}(kr) = \sqrt{\frac{\pi}{2kr}} H_{l+1/2}^{(2)}(kr), \tag{2.19}$$

where $H_n^{(2)}(\bullet)$ is the n-th order Hankel function of the second kind. The term $Y_l^m(\theta,\phi)$ represents the spherical harmonics:

$$Y_l^m(\theta,\phi) = \sqrt{\frac{2l+1}{4\pi}\frac{(l-m)!}{(l+m)!}} P_l^m(\sin(\theta))\, e^{jm\phi}, \tag{2.20}$$

with $P_l^m(\bullet)$ the associated Legendre function of degree l and order m. To evaluate the spherical harmonics of negative order, the following relation is used [1]:

$$Y_l^{-m}(\theta,\phi) = (-1)^m \overline{Y}_l^m(\theta,\phi), \tag{2.21}$$

with $\overline{x}$ the complex conjugate of x.

Based on this expansion, the following set of 3D unbounded wave functions is defined:

$$\Phi_{lm}^{(+)}\left(\vec{r}(r,\theta,\phi)\right) = h_l^{(2)}(kr)Y_l^m(\theta,\phi). \tag{2.22}$$

For each $l = 1, 2, \ldots l_{max}$, the corresponding $m = -l \ldots l$ are included in the function set, yielding a total of $n_w^{(\alpha)} = (l_{max}+1)^2$ wave functions. The spherical harmonics describe the tangential field in θ and ϕ, while the spherical Hankel function dictates the radial decay of the solution.

Analogous to the bounded domain case, the series of functions in the expansion has to be truncated. An equivalent rule imposing a desired resolution in the unbounded domain relative to the physical wave number yields:

$$l_{max} \simeq 2R_t T k, \tag{2.23}$$

with l_{max} representing the highest order of the Hankel function in the unbounded function set for 2D/3D problems. For 3D problems, l_{max} also corresponds to the highest degree of the spherical harmonics in the unbounded function set. The term R_t is the radius of the global truncation circle/sphere Γ_t^g. The physical interpretation of this rule is that a desired resolution of T half wavelengths is imposed on the unbounded domain along Γ_t^g. This approach is akin to the truncation for the bounded domains and provides a similar resolution of the functions in the unbounded and any possible bounded subdomain.

Particular solution

The particular solution $\hat{p}_f^{(\gamma)}$ in equation (2.7) can be defined in various ways. The most commonly used ones are presented here. An acoustic plane wave excitation traveling at a propagation angle ϕ is defined as:

$$\hat{p}_{f,pw}^{(\gamma)}(x,y) = e^{jk\left(d(\phi)\right)} \quad \text{for 2D problems,} \tag{2.24}$$

$$\hat{p}_{f,pw}^{(\gamma)}(x,y,z) = e^{jk\left(d(\phi)\right)} \quad \text{for 3D problems,} \tag{2.25}$$

where $d(\phi)$ is the propagation vector of the plane wave. A point or cylindrical source is defined as:

$$\hat{p}_{f,p}^{(\gamma)}(x,y) = \frac{\rho_0 \omega Q^{(\gamma)}}{4} H_0^{(2)}\left(kr_q^{(\gamma)}\right) \quad \text{for 2D problems,} \tag{2.26}$$

$$\hat{p}_{f,p}^{(\gamma)}(x,y,z) = Q^{(\gamma)} \frac{e^{-jkr_q^{(\gamma)}}}{r_q^{(\gamma)}} \quad \text{for 3D problems.} \tag{2.27}$$

with $r_q^{(\gamma)}$ the distance between the source and receiver position, $H_0^{(2)}(\bullet)$ the zero-order Hankel function of the second kind and $Q^{(\gamma)} = \int_{\Gamma^{(\gamma)}} q^{(\gamma)} \mathrm{d}\Gamma$, the source strength.

2.4.2 Evaluation of boundary and interface conditions

To build up the system of algebraic equations, the boundary and the interface residuals are enforced to zero through a Galerkin weighted residual formulation. The interface conditions are needed to satisfy the continuity among interfaces and couple acoustic subdomains. For the boundary residuals, equations (2.3), (2.4) and (2.5) are used. For the interface residuals, various coupling algorithms are available in the WBM literature [105]. The most common one is a direct equivalent normal velocity continuity condition (also referred to as impedance coupling condition) and it is defined for the interface between two subdomains γ and β as :

$$\begin{aligned} \vec{r} \in \Gamma_I : & R_I^{(\gamma,\beta)} \left(p^{(\gamma)}(\vec{r}), p^{(\beta)}(\vec{r}) \right) = \\ & \left(\mathcal{L}_v(p^{(\gamma)}(\vec{r})) - \frac{p^{(\gamma)}(\vec{r})}{\overline{Z}_{int}} \right) + \left(\mathcal{L}_v(p^{(\beta)}(\vec{r})) + \frac{p^{(\beta)}(\vec{r})}{\overline{Z}_{int}} \right) = 0, \end{aligned} \tag{2.28}$$

where $\overline{Z}_{int}$ is an impedance coupling factor which is generally chosen as the characteristic acoustic impedance $\rho_0 c$ [105]. The given continuity condition can be used for both bounded-bounded and bounded-unbounded subdomain interfaces.

With boundary and interface conditions defined, the weighted residual formulation can be formed. For each subdomain, the residual functions are orthogonalized with respect to a weighting function $\tilde{t}^{(\gamma)}$ or its derivative. For N_D number of subdomains and $N_I^{(\gamma)}$ number of interfaces for each subdomain, it is written as :

$$\begin{aligned} \sum_{\gamma=1}^{N_D} \Big[& \int_{\Gamma_v^{(\gamma)}} \tilde{t}^{(\gamma)}(\vec{r})\, R_v^{(\gamma)}(p^{(\gamma)}(\vec{r})) \mathrm{d}\Gamma \\ & + \int_{\Gamma_Z^{(\gamma)}} \tilde{t}^{(\gamma)}(\vec{r})\, R_Z^{(\gamma)}(p^{(\gamma)}(\vec{r})) \mathrm{d}\Gamma \\ & + \int_{\Gamma_p^{(\gamma)}} -\mathcal{L}_v^{(\gamma)}(\tilde{t}^{(\gamma)}(\vec{r}))\, R_p^{(\gamma)}(p^{(\gamma)}(\vec{r})) \mathrm{d}\Gamma \\ & + \sum_{\beta=1,\beta\neq\gamma}^{N_I^{(\gamma)}} \int_{\Gamma_I^{(\gamma,\beta)}} \tilde{t}^{(\gamma)}(\vec{r})\, R_I^{(\gamma,\beta)} \left(p^{(\gamma)}(\vec{r}), p^{(\beta)}(\vec{r}) \right) \mathrm{d}\Gamma \Big] = 0, \end{aligned} \tag{2.29}$$

where γ and β are the corresponding subdomain numbers. These notations are used to represent both bounded, α, and unbounded subdomains, $+$, in the

same manner with previous sections. Like in the Galerkin weighting procedure used in the FEM, the weighting functions $\tilde{t}^{(\gamma)}$ are expanded in terms of the same set of acoustic wave functions used in the pressure expansion (2.7) :

$$\tilde{t}^{(\gamma)}(\vec{r}) = \sum_{w=1}^{n_w^{(\gamma)}} \Phi_w^{(\gamma)}(\vec{r}) t_w^{(\gamma)} = \Phi^{(\gamma)}(\vec{r})\, t^{(\gamma)}. \tag{2.30}$$

Substitution of the pressure expansion (2.7) and the weighting function expansion (2.30) into the weighted residual formulation (2.29) yields a square matrix system, whose solution provides the unknown weighting factors of the *a priori* defined wave functions.

2.4.3 Solution and post-processing

Solving the wave model yields the unknown contribution factors. To calculate the main field variable, the pressure expansion in equation (2.7) is used together with the calculated weighting factors. Derived quantities can be easily calculated from the analytical derivative of equation (2.7), without additional loss of accuracy.

2.4.4 Enhancements to the WBM

The WBM in its pure form has been applied to various problem settings: 2D/3D bounded acoustic problems [38, 132], 2D/3D unbounded [13, 103] and semi-unbounded acoustic problems [12], plate bending problems [138], plate membrane problems [139], assemblies of flat shells [143], coupled vibro-acoustic problems [104] and poro-elastic problems [35, 36, 37].

While the WBM has shown great promise with the wide application range, it has its shortcomings as well, especially when applied on geometrically complex problems. To remedy this problem, various techniques have been developed. The Multi-level WBM (ML-WBM) [133] was originally developed to efficiently model acoustic multiple scattering problems, later it has been extended to acoustic inclusion problems [136] and plate bending problems with holes [142]. The ML-WBM is reviewed in detail in Chapter 4, while the symmetric boundary conditions are derived for the method in the same chapter. The hybrid Finite Element-Wave Based Method (FE-WBM) [137] couples the FEM and the WBM in order to model bounded acoustic problems with fine details on the boundaries. The FEM's ability to model complex details is used on the detailed boundaries, while the efficiency of the WBM is exploited by creating large, simple acoustic cavities inside the FEM domain. The method is extended to unbounded problems by using the unbounded WBM as an absorbing boundary condition to the FEM domain [11]. The hybrid FE-WBM is also applied on vibro-acoustic problems [135], where the FEM is used to model structural vibrations and the WBM is used to model the acoustic field. The modal

reduction techniques can be applied on the FEM part [134]. The method is extended to poro-elastic materials that are coupled to the acoustic domains as well [76].

An overview of the enhancements and recent applications of the WBM can be found in [33].

2.5 Comparison of the WBM and element based methods

The WBM belongs to the family of deterministic approaches together with the FEM and the BEM. Nevertheless, due to the fundamentally different choice of approximation functions and domain/boundary discretizations, a different modeling procedure and different properties are obtained. This subsection briefly compares the WBM modeling approach with the FEM and the BEM and highlights the advantages and disadvantages. It should be noted that all the methods are considered in their conventional forms, i.e. without recent enhancements listed in Sections 2.2.2 and 2.2.4. The main motivation here is to give an overview of the working principles of the methods.

Problem discretization and degrees of freedom The FEM divides the problem domain into a large number of small elements. The DoFs in a FEM model are the nodal values of the field variables, and inside the elements, the dynamic field is approximated using simple polynomial shape functions. The BEM discretizes the boundaries instead of the domain. Depending on the formulation (direct or indirect), the DoFs can be the nodal values of the field variables or the potentials. Compared to the FEM, the number of elements is smaller, however the system is still composed of a large number of small elements. As frequency increases and wavelengths shorten, the FEM and BEM meshes need to be refined to retain a similar accuracy as driven by interpolation and pollution errors [17, 52]. Contrarily, the WBM partitions the domain into a small number of large subdomains, which are frequency independent. The only prerequisite is that the bounded subdomains have to be convex [38]. The general strategy in the partitioning process is to divide the domain into the smallest number of convex subdomains, while avoiding steep changes in boundary conditions within a subdomain. The selected wave functions are frequency dependent, and they are exact solutions of the governing equations. The DoFs are the contribution factors of each of the wave functions and do not have a direct physical meaning. To obtain a finer spatial resolution of the dynamic field, the number of wave functions is increased, without changing the domain decomposition.

Problem geometrical complexity Due to the fine discretization, the FEM and the BEM have almost no restrictions regarding the geometrical complexity.

For the WBM on the other hand, all bounded domains need to fulfill the convexity requirement or that they have to be divided into convex subdomains. As the number of subdomains increases, so does the number of interfaces and consequently the integration length, leading to an increase in computational load. Consequently, the WBM shows its full efficiency for moderately complex geometries.

System matrix properties In general, the system matrices of the FEM are real-valued, large, frequency independent and sparsely populated with a banded structure. These properties allow for an efficient solution, and a reuse of the matrices for different frequencies. Nevertheless, for practical applications with absorptive materials, the material properties are complex and frequency dependent. In this case, the FEM matrices, which are complex, have to be recalculated for each frequency, hampering the efficient solution and also the straightforward applicability of modal reduction schemes. In contrast to FEM matrices, the BEM and WBM matrices are always complex, frequency dependent and fully populated. The BEM matrices are smaller compared to the FEM matrices and the WBM ones are even smaller than the BEM's. On the other hand, both for the BEM and the WBM, the matrices need to be reconstructed for every frequency of interest. As is common for Trefftz approaches, also the WBM yields ill-conditioned matrices [73, 152]. However, Desmet [38] has shown that, despite this ill-conditioning, an accurate solution can be obtained by applying direct solution methods if the WBM matrices satisfy both Picard conditions [140, 141].

Accuracy of derived variables The FEM has primary and secondary response variables and since simple polynomial shape functions are used in general to represent primary variables, the higher order derived quantities are approximated less accurately, e.g. velocity. Although the BEM also uses simple polynomial shape functions for the primary response variables, the derived variables can be calculated by analytical derivation without losing accuracy. When it comes to the WBM, since derivatives of wave functions are again wave functions, with the same spatial resolution, derived variables are predicted with the same spatial resolution as the primary variables.

Construction of the system matrices Building the WBM models involves the evaluation of integrals of highly oscillatory functions and building the BEM models requires computation of singular integrals. They both need extra care as compared to the construction of the FEM matrices, which only requires the integration of simple polynomial functions. For the BEM, coordinate transformations or special integration rules are used to avoid the singularities. Construction of the non-singular (off-diagonal) parts is more straightforward, however the computational load is still high because of the calculation of Green's function for all the possible interactions of the elements. In the end, although the system matrices are smaller than FEM's, constructing them is

computationally more demanding. For the WBM, due to the ill-conditioning of the WBM matrices, the integrations must be performed carefully to obtain a sufficient accuracy of the matrix coefficients. Numerical integration, by applying the Gauss-Legendre integration rule was shown to be the most efficient for the kind of integrals to be solved for a WBM scheme, since an efficient matrix multiplication [34] can be applied. This numerical integration technique is applied with a fixed number of quadrature points per smallest wavelength resulting from the selected wave number components in the wave function sets. Even so, the system building takes typically more time as compared to the FEM.

Solution of the system matrices Although the FEM matrices are in general sparse and symmetric, because of the large number of FEM degrees of freedom, the solution of the FEM matrices is the computationally most demanding part of its process. When compared with the solution of the BEM matrices, it is still faster because the reduction in the size of the matrix is not enough to overcome the difference between solving a fully populated and a sparse matrix. When it comes to the WBM, this statement is not valid anymore because the reduction in the size of the matrix is substantially higher as compared to the BEM, therefore the solution of the WBM matrices becomes the fastest among the three.

Overall computational performance Considering all of the above statements, it can be concluded that all three methods have their advantages and disadvantages and defining a clear winner is not possible. This is mainly due to the fact that the overall computational performance will mainly depend on the application. Therefore, without making bold statements, a general overview can be given as follows. The FEM and the BEM have advantages for highly complex geometries such that they don't have restrictions regarding the problem geometry. The WBM, on the other hand, shows its efficiency for moderately complex geometries and loses its edge when applied on highly complex ones. With that stated, the WBM is more efficient than the FEM and the BEM when used for the right application. It also has a better convergence rate which allows the method to tackle a higher frequency range than the others. Besides the complexity of the problem, another important factor is the type of the problem, i.e. if it is bounded or unbounded. As a general rule, the FEM is better suited for the bounded problems and the BEM is for the unbounded, because the FEM needs special treatments to be able to solve the unbounded problems. This extra step typically makes it lose its appeal against the BEM. As for the WBM, the efficiency is not affected by the type of the problem as it can inherently solve the unbounded problems. Last but not least, the WBM has an easy preprocessing and refinement procedure, because it is a meshless method. The element based methods need remeshing of the domain/boundary for higher frequencies, which leads to a considerably long preprocessing time. All the aforementioned properties make the WBM an appealing alternative for both the FEM and the BEM for moderately complex geometries. It is because

of this appeal that the method has been applied to various fields and extended to different forms, e.g. the hybrid and multi-level approaches, which are detailed in the following sections and chapters.

2.6 Conclusion

This chapter presents a short survey on the state-of-the-art in deterministic modeling of acoustic problems. The mathematical description of the considered problem is given first. The most commonly used element based methods, i.e. the FEM and the BEM are reviewed, together with various recent enhancements to their conventional forms. A brief overview of the Trefftz methods is presented, which is followed by a detailed description of the WBM. Finally, a comparison of the WBM and element based methods is provided.

The state-of-the-art review shows that, even though there are various enhancements to the element based methods, no method has emerged to cover the mid-frequency range without introducing certain disadvantages. While the computational performance of the numerical methods is a key aspect, the practical applicability of the methods is affected with other issues as well. User friendliness, the ease of preprocessing and refinement procedures also play important roles. As such, critical research efforts are being spent in developing alternative methods. The WBM belongs to that category and is a deterministic method that has shown great potential as a mid-frequency method. However, because of the geometrical requirements, the method has not fulfilled its full potential yet.

Considering the need for new methods for mid-frequency problem, the main goal of this work is set as extending the possible problem configurations where the WBM can be applied. Moreover, assessment of the WBM for new application areas is considered.

Chapter 3

Application of the WBM on a room acoustics case

In this chapter, the performance of the WBM is assessed by means of a room acoustics application. The main aim is to demonstrate the efficiency of the method in its pure form. This way, the motivation is also set for using the WBM and its extensions in the more complex configurations for the following chapters, i.e. inclusion and multiple scattering problems.

Numerical simulations on room acoustics typically aim at the prediction of the impulse response (IR) between source and receiver. The IR lies on the basis of calculations of room acoustical quantities such as the reverberation time, the sound pressure level, the clarity and the speech intelligibility which are used for room acoustical assessment and can be used as well as for acoustical visualization, e.g. auralization of a site. However, the main aim of this section is to assess the performance of the WBM and its applicability for tackling acoustic problems involving large problem domains, i.e. rooms. As such, transfer functions between a source location and several receiver points are calculated and compared with measurements. Furthermore, as the WBM is being developed to provide an alternative to deterministic methods, the WBM prediction results are benchmarked with the Fast Multipole Boundary Element Method (FM-BEM) [51], another mid-frequency prediction technique. Next to the large dimensions of the considered room, the frequency range of the steady-state analysis is determined as the 125 Hz, 250 Hz, 500 Hz and the 1 kHz octave bands. This means, the highest frequency to be calculated is 1420 Hz. As a result, the simulations become a real challenge for the deterministic methods in terms of computational times.

In the comparison of the WBM results with measurements, a typical room acoustics prediction method is also included. The most popular algorithms for room acoustics simulations are based on the Image Source Method (ISM) [54], Ray-Tracing Method (RTM) [144] and on the Beam-Tracing Method

(BTM) [53]. It is known that each of these approaches has its advantages and disadvantages. Thus, a combination of methods is very common, enabling the improvement of the accuracy and speed of the calculation. In this work, one such hybrid method, implemented in the ODEON software [117], is used. For the sake of brevity, the hybrid method facilitated by ODEON is addressed as a conventional ray tracing method in the rest of the study. The main simplification made in ray-based methods, i.e. replacing waves by rays, is typically compensated by ad hoc introduced scattering. An international round robin test on acoustical numerical simulation has shown that only simulation algorithms that include scattering can provide reliable results [147]. A second round robin test in the year 2000 has shown that most of the already existing simulation software has similar accuracy and the main problem lies in the prediction of low frequencies [16]. This leads to the motivation of adding a ray tracing method to the comparison of the WBM and the measurements, as the deterministic methods are meant to yield higher accuracy in the low-frequency range, whereas the ray-tracing method is expected to only become accurate at higher frequencies.

The following sections give a description of the room under investigation, elaborate on the details of the numerical models used and present the comparisons of the FM-BEM and the WBM. Comparison to ray tracing simulations and measurements is also presented.

3.1 Geometry description and source information

The room under consideration has a width of 7.65 m, a depth of 6.25 m and a height of 2.35 m as shown in Figure 3.1. The acoustic source is represented as S in Figure 3.1(a) while the 11 receiver points are represented with R1 to R11. All the receiver points and the source are at 1.2 m above the floor level. The room has 4 windows and 1 door as well as two pieces of furniture. The absorption coefficients of the different surfaces of the room are given in Table 3.1. These values are obtained by updating the standard material values. The absorption of the interior surfaces are updated so that the corresponding reverberation time calculated by the ray tracing method matches the measured reverberation time.

The room resembles an L-shape structure with one small part and a big main part. In the small part, there are 3 receivers, namely receiver points R9, R10, R11. These points are in the indirect sound field and make the simulations more interesting as they provide a more challenging geometry and make the effects of absorption and diffraction more emphasized.

The source is considered as an omni-directional point source and the sound pressure levels at 1m distance from the source in a free field are given in Table

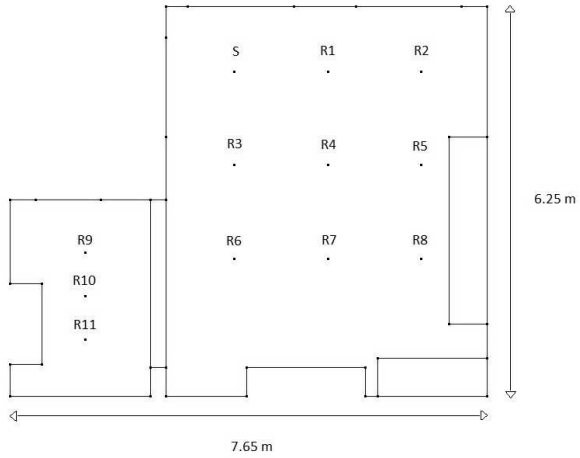

(a) Top-view

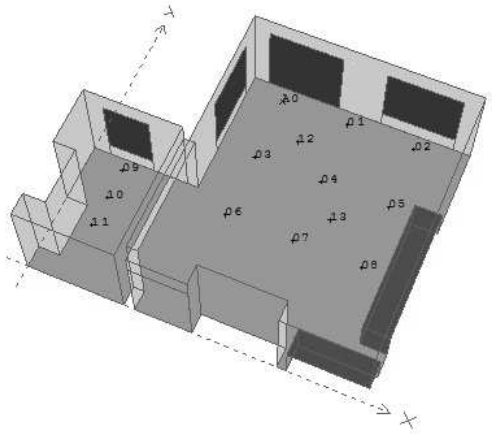

(b) Iso-view

Figure 3.1: Geometry of the room

3.2. The point source assumption is valid as long as the dimensions of the loudspeaker are small with respect to the acoustic wavelengths.

3.2 Deterministic models information

To represent the absorption on the surfaces in the deterministic models, acoustic impedance values are required as inputs. A general formulation known

Table 3.1: Absorption values

absorption - α_i [%]	125 Hz	250 Hz	500 Hz	1 kHz
furniture	10	10	10	10
ceiling	20	30	45	45
wall	2	2	2	3
door	13	10	9	10
windows	10	10	10	10
floor	4	4	4	5

Table 3.2: Point source characteristics

Octave bands	125 Hz	250 Hz	500 Hz	1 kHz
SPL at 1m	59 dB	62 dB	65 dB	68 dB

for the relation of the absorption coefficient and the acoustic impedance is [102]:

$$\alpha_i(\varphi) = 1 - \frac{(Z'\cos(\varphi) - 1)^2}{(Z'\cos(\varphi) + 1)^2}, \qquad Z' = Z_n/Z_0, \tag{3.1}$$

where Z_0 is the characteristic impedance of air, Z_n is the acoustic impedance of the material and φ is the incidence angle of the sound waves. This relation holds as long as $Z_n >> Z_0$ and for all the materials used in this study, equation (3.1) is valid. Since the absorption coefficient values given in Table 3.1 are random incidence absorption coefficients, one more step is needed to have a direct relation between the random incidence absorption coefficient and the acoustic impedance. The random incidence formulation for the absorption coefficient is [102]:

$$\alpha_{\text{random}} = \int_0^{\pi/2} \alpha_i(\varphi)\sin(2\varphi)\mathrm{d}\varphi. \tag{3.2}$$

Combining equations (3.1) and (3.2) yields the following:

$$\alpha_{\text{random}} = \frac{8Z'(2+Z')/(1+Z') - 16\log(1+Z')}{Z'^2}. \tag{3.3}$$

Having the direct relation between the random incidence absorption coefficient and the acoustic impedance in hand, it is possible to calculate Z_n values using the information in Table 3.1. A root finding algorithm, consisting of Bisection and Newton-Raphson approaches, is used for the acoustic impedance calculations.

The results presented in the latter sections for comparison of the numerical methods and the measurements are displayed in octave bands. Since the WBM has been established for steady-state problems so far, narrow band calculations

are summed up to get octave band results. The same is done for the FM-BEM predictions. To prevent critical data loss in the conversion from narrow bands to octave bands, different frequency resolutions are used for different octave bands. For the 125 Hz octave band, 1 Hz resolution is used; for the 250 Hz octave band, 5 Hz resolution is used and for the 500 Hz and the 1 kHz octave bands, 10 Hz resolution is used. The aforementioned resolutions are confirmed by a convergence analysis in rerunning calculations with smaller frequency steps for each octave band and making sure the differences between two different frequency resolutions are very small.

3.2.1 WBM model information

The considered room geometry is partitioned into 13 convex subdomains as illustrated in Figure 3.2. For the coupling of the subdomains, an impedance coupling approach as given in equation (2.28) is used with the impedance coupling factor being $Z_{int} = 41.65 + 41.65j$.

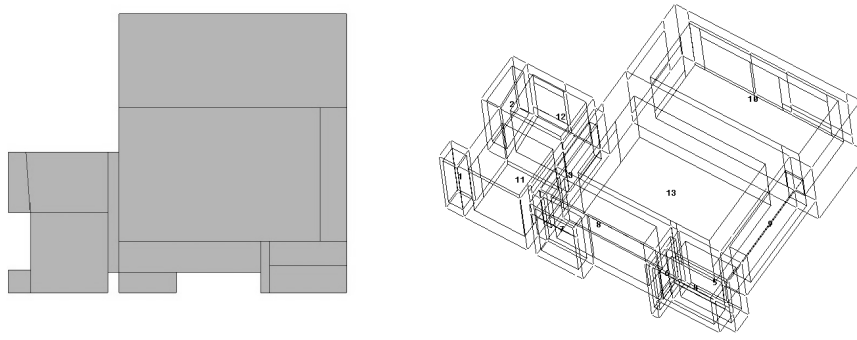

(a) Top-view (b) Iso- view

Figure 3.2: Partitioning of the WBM model into 13 subdomains

To determine the number of wave functions used in the WBM expansions, a truncation factor of T is applied (see equation (2.15) for more details) which relates the largest wave number component in the applied wave functions to the characteristic wave number. In this study, the truncation factor is chosen as $T = 4$ for the 125 Hz octave band, $T = 2$ for the 250 Hz octave band, $T = 1.3$ for the 500 Hz octave band and finally $T = 1$ for the 1 kHz octave band. In order to have a reasonable comparison with the FM-BEM with respect to the number of degrees of freedom, the mean value of the number of wave functions is calculated by averaging the maximum and minimum number of wave functions for the corresponding octave bands (see Table 3.4).

To compare the WBM calculations with measurements, the air absorption effect has to be taken into account. Adding air absorption to the WBM models is possible by adding a complex part to the speed of sound. When the air absorption data are available in dB/100 m, a conversion is required.

The conversion starts from adding an absorption term to the sound pressure formula:

$$p(x,t) = P_0 e^{-j\omega(t-x/c_0)} e^{-\alpha_n x}, \tag{3.4}$$

where α_n, the absorption coefficient, is in Nepers per meter. Rewriting equation (3.4) yields:

$$p(x,t) = P_0 e^{-j\omega t + j\omega x(1/c_0 + j\alpha_n/\omega)}, \tag{3.5}$$

which makes it possible to interpret the speed of sound c as:

$$\frac{1}{c} = \frac{1}{c_0} + j\frac{\alpha_n}{\omega}, \tag{3.6}$$

and eventually as :

$$c = \frac{c_0\,\omega^2 - j\,c_0^2\,\omega\,\alpha_n}{\omega^2 - c_0^2\,\alpha_n^2} \tag{3.7}$$

Finally, α_n in Nepers per meter should be replaced by α_i in dB/100m with the following:

$$\alpha_n = -\ln(10^{\frac{\alpha_i}{20\cdot 100}}). \tag{3.8}$$

All WBM calculations are performed with a dedicated C++/Fortran implementation.

3.2.2 FM-BEM model information

For each octave band, a different surface mesh of the room is constructed with different element size. Because the considered problem size is big and the maximum frequency calculated is very high for a deterministic method resulting in calculation times on the order of days (see Table 3.4), the validity of the surface meshes, obeying the six elements per wavelength criteria, are kept at corresponding octave band frequency limits as shown in Table 3.3. The resulting number of degrees of freedom for the FM-BEM models are presented later in this chapter, in Table 3.4 and it is apparent that they quickly exceed a number that is feasible to evaluate with a conventional BEM.

Table 3.3: Assuming 6 elements per wavelength, FM-BEM results are valid up to:

Octave bands	125 Hz Oct.	250 Hz Oct.	500 Hz Oct.
Max. Freq.	182 Hz	364 Hz	728 Hz

All FM-BEM calculations are performed using LMS/Virtual.Lab with default settings, i.e. the final normalized residual and the inner loop normalized residual are 0.001.

3.3 Measurements and ray tracing model information

3.3.1 Measurements

The L-shaped room under consideration is a living room in a student dormitory in TU Delft. The room has a suspended absorptive ceiling, a linoleum floor and hard concrete walls with painting as final layer with absorption coefficients as stated in Table 3.1. During the measurements, all the furniture was removed from the place except for a few pieces of hard wooden kitchen cupboards. Impulse response measurements have been performed according to ISO 3382 by using a dedicated Matlab routine and a logarithmic sweep as a excitation signal. Figure 3.1 displays the floor plan of the room and indicates where the source and receivers were positioned during the measurements. For the measurement, both the source and the microphones were positioned at a height of 1.2 m above the floor level. For the analysis (such as the estimation of the reverberation time and the sound pressure level) the MLaus® software, developed at TU Delft, was used.

3.3.2 Odeon simulation

In order to compare deterministic prediction results with classical room acoustics predictions, ODEON [117] ray tracing predictions are also included in the comparison. The software uses an algorithm where two geometrical methods are combined to predict the impulse response. The simulation of the room impulse response (RIR) is in principle performed for two parts of the time evolution. The early part, which contains information about early reflections, is calculated by combining the Image Source Method and Early Scattered Rays (ESR). The duration of the early part can be chosen by the user via the so-called Transition order (TO). This is the maximum number of image sources taken into account per initial ray [88]. The second and final part of the RIR, i.e. the late reflections, is calculated by a modified ray-tracing algorithm that takes into account also the scattering coefficient of the involved surfaces. At every reflection event, local diffuse secondary sources are generated that radiate sound with a directivity according to Lambert's cosine-law [27, 151].

The geometrical 3D model of the room is based on measured dimensions of the room in situ. The acoustical properties of the interior surfaces are estimated so that the corresponding reverberation time matches the measured reverberation time in the room and they are presented in Table 3.1. Simulations are performed in ODEON v.9.0 with the transition Order TO set to 2. The maximum reflection order is 2000 and the number of rays used for the simulation is 5000.

3.4 Numerical and experimental validation

As mentioned earlier, the main aim of this study is to apply the WBM for the analysis of a room acoustics case and demonstrate its efficiency. As such, performance comparison with another mid-frequency prediction technique, the FM-BEM, is presented first. Secondly, the WBM predictions are compared with measurements and ray tracing predictions. The reason why results from all four methods, i.e the WBM, the FM-BEM, the measurements and the ray tracing method are not compared at the same time is that the FM-BEM implementation does not allow the inclusion of air absorption. For the WBM, it is possible by making the speed of sound complex as described in section 3.2.1 and for the ray tracing software it is an inherent functionality.

Whereas the effect of air absorption is negligible for the 125 Hz octave band, it starts to show its significance at the 250 Hz octave band and for higher frequencies it becomes very crucial. This effect is discussed more in detail later in this chapter.

Regarding the measurement comparisons; it should be noted that there may be an inherent disadvantage for deterministic methods as compared to ray tracing. The reason is that the data available as absorption coefficients of the surfaces were obtained by matching the ray tracing results to the measurements as mentioned in Section 3.1. This issue is also discussed later on.

3.4.1 WBM vs. FM-BEM

Figure 3.3 shows the comparison of FM-BEM vs. WBM models for octave band averages. There are 3 subfigures for the results of the 125, 250 and 500 Hz octave bands, respectively. The x axis represents the predictions for 11 receiver points and the y axis gives the sound pressure levels in dB. The black bars belong to the FM-BEM results whereas the gray bars are the WBM results.

For the octave band averages, the difference between the two deterministic methods are in the order of 0.5 dB, which is a good agreement for the considered large problem. On the other hand, it is of interest to have a more detailed look at the results in order to discuss possible sources of errors.

Figure 3.4 shows the comparison of FM-BEM vs. WBM models for narrow band frequencies that are used to calculate the octave band averages. The predictions are presented for two receiver points: receiver point 7 and 9. They are chosen to represent the results for direct and indirect fields. For both points, the predictions of the WBM and the FM-BEM models are very similar. There are small discrepancies between the two that lead to the aforementioned differences on the band averages. However, the general behavior of the two models agree with each other and the results are satisfactory for the purpose of this study.

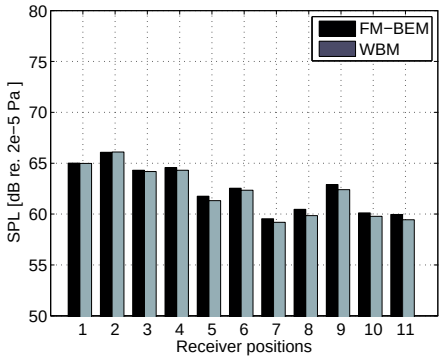

(a) 125 Hz octave band results

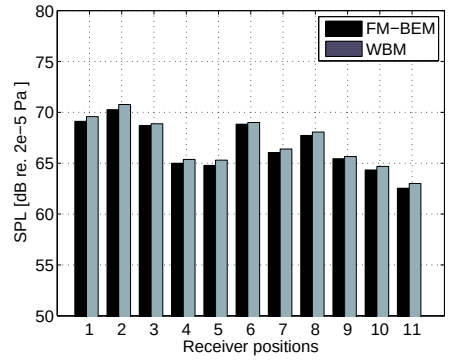

(b) 250 Hz octave band results

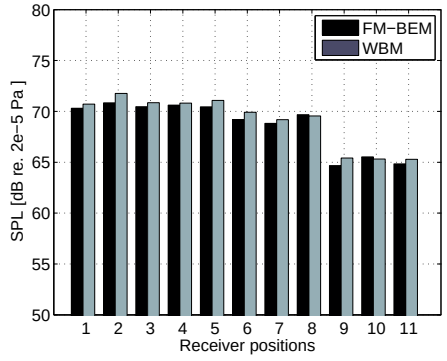

(c) 500 Hz octave band results

Figure 3.3: Octave Band average comparisons of the FM-BEM vs. the WBM

With that stated, it is still worthwhile to discuss the possible source of errors. For both points 7 and 9, the discrepancies between the two models start after around 400 Hz. While the mesh validity of the FM-BEM for the 500 Hz octave band has been configured to follow the 6 elements per wavelength rule, it has been demonstrated that when the wave field becomes more complicated, 10 elements per wavelength rule yields more reliable predictions [92]. In the presented case, the FM-BEM model mesh is valid only up to 437 Hz, if the 10 elements per wavelength rule is followed. As such, the small differences on the FRF results may stem from the FM-BEM model (a substantial refinement of the FM-BEM model was prohibited due to computational resources as explained later). It is also possible that the WBM model may be the source of the discrepancies. To test this statement, the WBM model was refined by increasing the truncation rule from $T = 1.3$ to $T = 1.5$ for the 500 Hz octave band. However, the results did not get closer to the FM-BEM results. A final remark is that the sampling rate of the 500 Hz band is adjusted to provide good accuracy for the band averages, however, it may not be good enough to provide high resolution for the narrow band comparisons. As such, the small

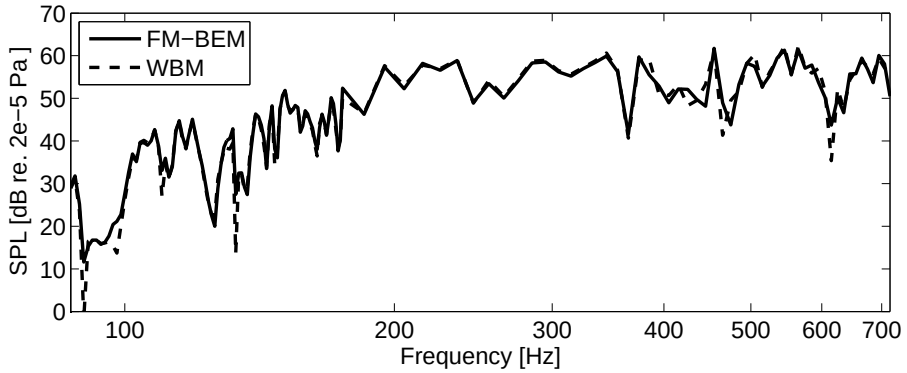

(a) Results for receiver point 7

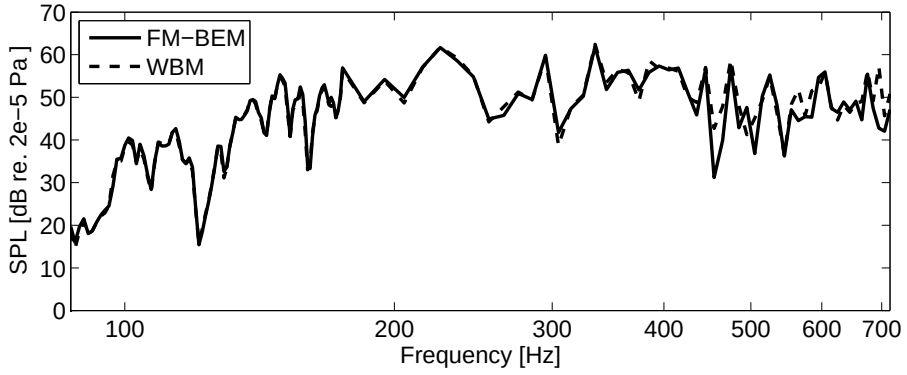

(b) Results for receiver point 9

Figure 3.4: Comparison of the FM-BEM vs. the WBM for the narrow band data used in band averaging

differences on the FRF curves may stem from rather unlucky points.

Nevertheless, both methods give similar results and it is of interest to compare the calculation times of the two. The benchmarks have been conducted on a Windows server system with eight Intel Xeon 2.8 GHz processors and 32 GB of RAM.

The CPU times, which include the system building and system solving times, are presented in Table 3.4 [1] They are given for a frequency resolution of 10 Hz for all the octave bands to present uniform data.

It is clear that the WBM has a significant advantage over the FM-BEM in terms of calculation times in the mid-frequency range. The most notable performance difference is at the 500 Hz octave band where the WBM is more than 6 times faster than the FM-BEM. It is also shown that the WBM models are always

[1]These performance figures were obtained while the WBM used 1 processor and the FM-BEM used up to 8 processors.

smaller than the FM-BEM models. These results prove that the WBM has a great potential as an alternative deterministic method for mid-frequency analysis.

Table 3.4: FM-BEM vs. WBM time and degrees of freedom comparison

	125 Hz Oct.	250 Hz Oct.	500 Hz Oct.	1 kHz Oct.
# of freq. steps	11	20	36	72
FM-BEM - CPU time	1h 11min.	9h 0min.	66h 44min.	-
WBM - CPU time	1h 6min.	2h 7min.	9h 45min.	120h 24min.
FM-BEM - nodes	4474	17890	71554	-
FM-BEM - elements	8944	35776	143104	-
WBM - DoF	4323	4591	6761	14370
[min - max # of DoF]	[2056 - 6590]	[2148 - 7034]	[3182 - 10340]	[6440 - 22300]

On a side note, a refinement on the FM-BEM mesh has been attempted, which was aimed to be used for the 1 kHz octave band and which led to 858626 DoF. However, by using the current accuracy settings for the FM-BEM, the simulations became prohibitive in terms of CPU time. To calculate the 1 kHz octave band average value, the inner residual error was decreased from 0.001 to 0.01, which led to simulations that took 13 days to calculate. Since this kind of long simulation times are not practical and the results were not reliable because of the decreased accuracy, the 1 kHz octave band simulations are omitted for the FM-BEM. The WBM model details are given in Table 3.4 to provide data for the comparison with the measurements and ray tracing results.

3.4.2 WBM vs. Measurements and Ray Tracing Method

Figure 3.5 compares the WBM results with the measurements and the results from ray tracing (ODEON), illustrating the sound pressure levels in dB for four different octave band results. In addition to the 11 points on the y axis, like with the FM-BEM comparison in Figure 3.3, an extra point 12 is added to the y axis which represents the spatial pressure average of the 11 receiver points, calculated with the following formula:

$$\mathrm{SPL}_{\mathrm{avg}} = 20 \cdot \log_{10}\left(\frac{\sum_{i=0}^{11}\left(|p_i(\vec{r})|\right)}{11 \cdot 2 \cdot 10^{-5}}\right). \tag{3.9}$$

As such, it is an indication of general energy level differences. The black bars represent the measurements, the gray bars belong to the WBM results and the white bars are for the ray tracing results.

Starting with the 125 Hz octave band results; there is a varying difference among the different receiver points when the WBM and the measurements are compared. Even though the spatial average prediction of the WBM is within 2

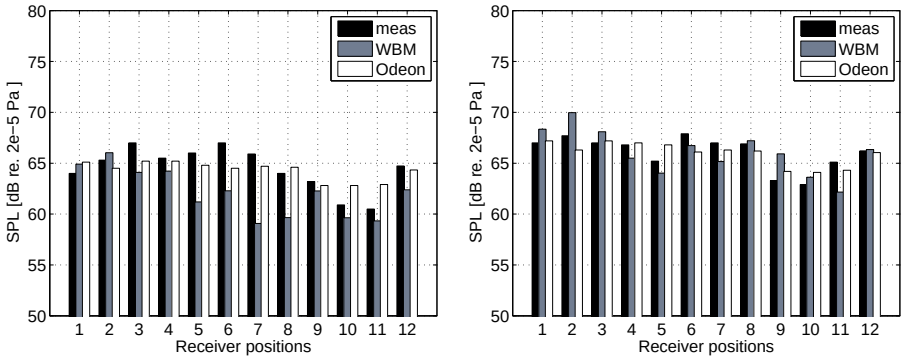

(a) 125 Hz octave band comparisons

(b) 250 Hz octave band comparisons

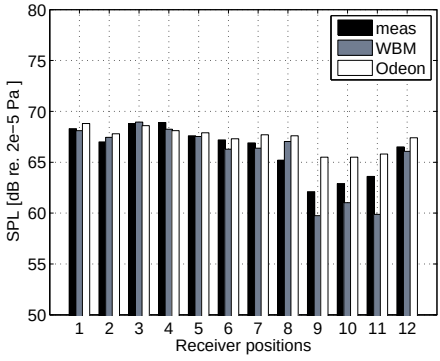

(c) 500 Hz octave band comparisons

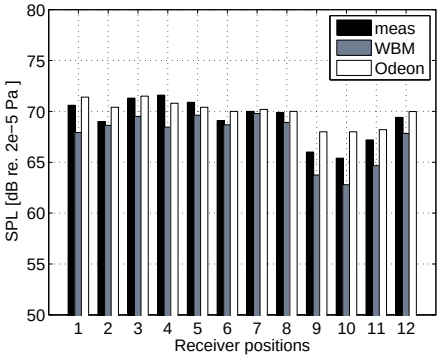

(d) 1 kHz octave band comparisons

Figure 3.5: Comparison of measurements, ODEON and WBM results

dB of the measurements, the difference in individual points can be up to 7 dB. On the other hand, for most of the points, the ray tracing predictions are closer to the measurements. This is a surprising result as the expected behavior of the WBM is to be more accurate at low- to mid-frequencies whereas the ray tracing method might experience some problems because of the possibility of a non-diffuse wave field. To make sure the inaccuracy of the WBM does not stem from the method itself or its application manner but from the general behavior of the deterministic methods, some other numerical models are included in the comparison in Figure 3.6. The methods applied are the FM-BEM, the conventional indirect BEM and the conventional linear FEM. It should be noted that, such a comparison is only possible for the 125 Hz octave band, because the air absorption effect is negligible (so that the FM-BEM can be included) and solving large models is still feasible (so that FEM and BEM can be included). It is clear that all the deterministic methods, including the WBM, give nearly the same results while these results are still considerably different from the measurements. Thus, one can deduce that the considered difference of the WBM results (and of the other deterministic methods) and the measurements

follows from a discrepancy in the deterministic numerical modeling of the room.

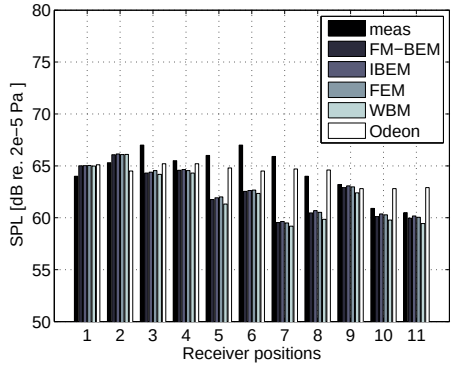

Figure 3.6: Comparison with other deterministic methods for 125 Hz octave band

Looking at the 250 Hz and the 500 Hz octave bands, the WBM performs on average within 2 dB of the measurements for the individual receiver points. Moreover, the spatial averaged results are as close as 0.5 dB to the measurements. The ray tracing results illustrate a similar performance. Both methods have problems in accurately predicting the response in points 9, 10 and 11, i.e. the points in the indirect sound field.

Finally for the 1 kHz octave band, the individual receiver point results of the WBM vary within 3 dB of the measurements while the spatial average is within 1.5 dB. Compared to ray tracing results, it is apparent that the ray tracing predictions are slightly better than the WBM predictions with individual receiver differences being within a 2.5 dB error band.

Considering that the 1 kHz octave band's upper limit is 1420 Hz, the predictions and the measurements are getting more sensitive to a variety of effects. These include the errors from both the measurement side and the numerical methods side. First of all, there is the assumption of using a point source in numerical models from the very beginning as mentioned in Section 3.1, while in reality a bulky omni-directional loudspeaker was used. As such, at higher frequencies, the acoustic wavelenght is getting closer to the size of the loudspeaker and the point source representation looses its validity. Other than that, there is the sensitivity of the receiver positions which in reality can deviate several centimeters. By adding extra receiver positions in the WBM calculations, which are 10 cm away from the original points, Figure 3.7 is attained. The extra receiver points are included in all four directions of the original points by keeping the same height. The resulting difference is for most points within 1.5 dB. However, for some points and directions, it can be as high as 4 dB. These results illustrate that another source of error can be the deviations in the exact receiver positions.

Even though the sensitivity of the receiver positions and the point source

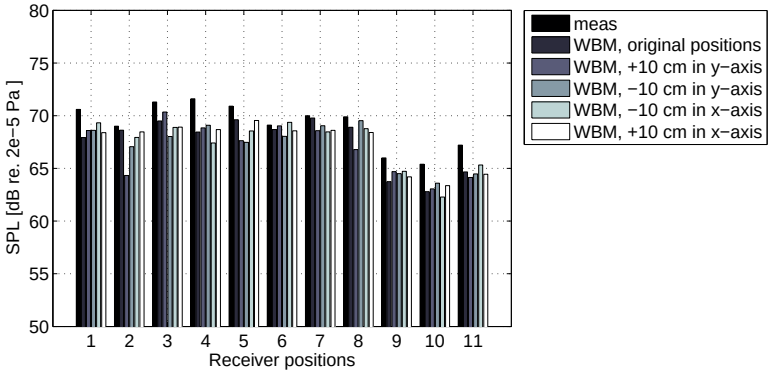

Figure 3.7: Sensitivity of the positions for 1 kHz octave band

assumption play an important role on the variance of the results, surely they are not the only factors. One can check the WBM results for the 1kHz octave band in Figure 3.8, where the only difference is the air absorption addition to the model and see that the difference can be up to 7 dB. Moreover, the measured values always stay between the values given by the two WBM models, demonstrating that updating the WBM model with better air absorption values would yield better results. As such, it is crucial to point out the assumptions behind the added air absorption effect. Besides assuming the humidity as 60% and the temperature as 20 degrees Celsius, the air absorption has been assumed as constant within each octave band for the WBM models. In other words, for the 1 kHz octave band, the air absorption at 710 Hz and 1420 Hz are the same, while in reality they are different. This assumption might be one of the sources of errors as well.

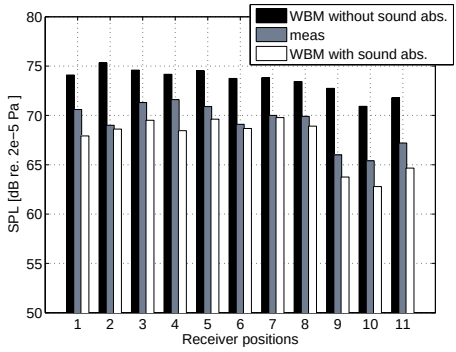

Figure 3.8: Comparison of WBM models with and without air absorption for 1 kHz octave band

Last but not least, it is important to note that the absorption coefficients in Table 3.1 are the values that are retrieved from an updated ray tracing model. As such, the updated values may not be representing the actual physical

problem accurately anymore, but may be serving to match ray tracing results to the measurements, especially for low frequencies. However, even with the boundary conditions favoring ray tracing results, the WBM predictions match the measurements in mid-frequency range with a good accuracy.

3.5 Conclusion

Comparison of the WBM and the FM-BEM results yields that the two deterministic methods provide very similar results. The WBM is shown to be considerably faster than the FM-BEM for the presented case.

Comparison with measurements show that the WBM predicts the overall energy levels of the measurements within 2 dB. A surprising outcome is the significant difference between the measurements, the ray tracing results and the WBM for the 125 Hz octave band of up to 7 dB . It has been illustrated that other deterministic prediction techniques yield results similar to the WBM, which hints at a problem in the deterministic modeling of the problem with regard to the definitions of the boundary conditions and the source.

A last observation is that the effect of air absorption on room acoustics simulations is very strong, even at lower frequencies. Illustrated with the WBM simulations, the effect can be as high as 7 dB, making accurate modeling of the air absorption crucial for good predictions.

In the end, this chapter illustrated the WBM's great potential as a mid-frequency analysis method once more, when applied on a suitable geometry. It is because of this potential that the following chapters focus on extending the problem configurations WBM can be applied on, either through the Multi-level concept or through hybrid schemes.

Chapter 4

The Multi-level Wave Based Method

This chapter starts with a review of one of the major extensions to the WBM called Multi-level WBM (ML-WBM) [133]. The ML-WBM allows the WBM framework to be efficiently used for multiple scattering and inclusion problems. One application area that is highly suitable for the ML-WBM is the numerical modeling of sonic crystals, which are defined as periodically distributed scatterers in a fluid. They mostly consist of a large number of scatterers that have a symmetric distribution. The computational cost of solving such problems can be too high, even for an efficient method like the ML-WBM. To remedy this, symmetric boundary conditions for the ML-WBM are derived for 2D and 3D multiple scattering problems. By exploiting the symmetry of the problem configuration, the limits of the addressable problem size are increased. The benefits of using symmetric boundary conditions are demonstrated in the following chapter, in the context of acoustic lens designs.

The chapter is organized as follows: the critical modeling steps that differentiate the ML-WBM from the WBM are presented first. It is followed by the derivation of the symmetric boundary conditions for 2D problems and the resulting weighted residual formulation. Finally, the symmetric boundary conditions are extended to 3D problems.

4.1 Modeling principle

As stated in the previous chapters, a sufficient condition for the WBM to converge for the bounded problems is the convexity of the considered domain or that the domain is divided into convex subdomains [38]. This inherent property of the WBM for bounded domains also affects the unbounded problems,

because the strategy for the modeling of unbounded problems involves the decomposition of the field into bounded and unbounded domains.

The main strategy in the partition process of the WBM is to end up with a rather small number of large subdomains in order for the WBM to show its full efficiency [105]. While for many applications, it is possible to use the WBM efficiently in its pure form, there are various configurations where it loses its efficiency. For certain configurations, the use of the WBM can even be unfeasible. One such challenging configuration is the multiple scattering problem. The conventional WBM uses one global truncation circle/sphere (for 2D/3D problems) that encloses all the geometry at once to partition the domain to bounded and unbounded subdomains. When the scatterers are well separated from each other, the necessity to model the vast area in between the scatterers hampers the efficiency of the WBM. To remedy this problem, a multi-level framework for the WBM has been proposed for multiple scattering problems [133].

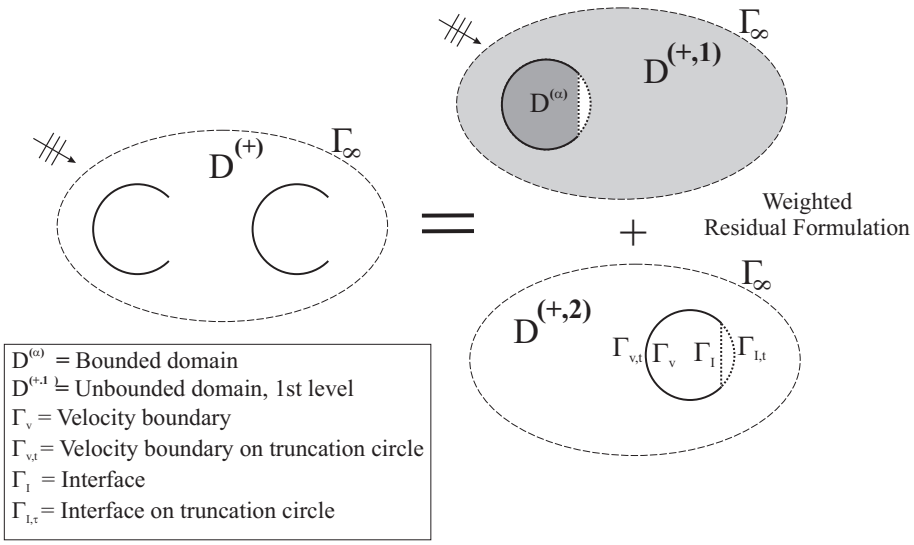

Figure 4.1: Graphic representation of the multi-level modeling concept, together with the definitions for subdomains and boundaries. Definition for a bounded subdomain is shown on the first scatterer (the upper one) and definitions for boundaries are shown on the second scatterer (the lower one).

The main idea of the Multi-level WBM approach for unbounded problems is to consider the multiple objects in the problem as different 'levels' of the problem, as shown in Figure 4.1. As such, instead of using one global truncation circle/sphere Γ_t^g enclosing all the scatterers, every object is enclosed by a close fitting truncation boundary and each one of these truncation boundaries represents a level. The incident field for any level in the problem domain is the scattered field from the other levels and possible external excitation (e.g. plane wave or point source). The levels are combined in a weighted residual manner

to build up the system of equations and the resulting system is solved at once to obtain the weighting factors associated with all the levels. As such, the four main steps of the WBM modeling procedure are updated for the ML-WBM as follows:

A. Definition of the levels and partitioning into subdomains.

B. Selection of the appropriate wave functions in the pressure expansion.

C. Construction of the system of equations and coupling of the levels via a weighted residual formulation of the boundary and continuity conditions.

D. Solution of the system of equations and postprocessing of the dynamic variables.

The procedure of using levels and modeling each scatterer in its close fitting truncation reduces the model size, saves modeling effort and makes the ML-WBM better suited for multiple scattering problems as compared to the WBM.

The ML-WBM has also been applied to bounded problems with inclusions [136]. The existence of inclusions within bounded domains violates the convergence criteria. With the ML-WBM, the bounded domains with inclusions can be modeled like two separate problems: a bounded domain without inclusion and an inclusion without the bounded domain. Removing the necessity to partition the space around the inclusion brings a great performance advantage and extends the possible range of configurations that can be tackled with the WBM. The modeling steps, as they are described above, stay the same for bounded problems.

The review of the ML-WBM in this chapter is given only for unbounded problems, since the application cases presented in the next chapter are multiple scattering cases. More details on the application of the ML-WBM to bounded problems can be found in [136].

4.1.1 Field variable expansion

In the considered problem, the primary field variable is the steady-state acoustic pressure $p(\vec{r})$ and it is approximated by a solution expansion $\hat{p}^{(\bullet)}(\vec{r})$. The selection of the wave functions differs for bounded and unbounded subdomains. Moreover, the solution expansions are also defined differently. For a field point within a bounded domain, $D^{(\alpha)}$, the acoustic pressure is approximated as:

$$\hat{p}^{(\alpha)}(\vec{r}) = \sum_{w=1}^{n_w^{(\alpha)}} \Phi_w^{(\alpha)}(\vec{r})\, t_w^{(\alpha)} + \hat{p}_f^{(\alpha)}(\vec{r}) = \Phi^{(\alpha)}(\vec{r})\, t^{(\alpha)} + \hat{p}_f^{(\alpha)}(\vec{r}), \quad \vec{r} \in D^{(\alpha)}. \tag{4.1}$$

In this expression, α is the corresponding number of the bounded WBM subdomain. The functions $\Phi_w^{(\alpha)}$ represent *a priori* defined bounded wave

functions, $t_w^{(\alpha)}$ are their corresponding contribution factors and $n_w^{(\alpha)}$ is the number of wave functions within subdomain $D^{(\alpha)}$. The term $\Phi^{(\alpha)}$ is the row vector collecting bounded wave functions and $t^{(\alpha)}$ is the column vector collecting weighting factors.

For a field point that is located in the unbounded domain $D^{(+)}$, the solution expansion is defined as the sum of pressure values coming from each level (See Figure 4.1 for the concept and domain definitions). Subsequently, the exterior acoustic pressure is approximated as:

$$\begin{aligned}\hat{p}^{(+)}(\vec{r}) &= \sum_{i=1}^{n_\lambda} \sum_{w=1}^{n_w^{(i)}} \Phi_w^{(+,i)}(\vec{r})\; t_w^{(+,i)} + \hat{p}_f^{(+)}(\vec{r}) \\ &= \sum_{i=1}^{n_\lambda} \Phi^{(+,i)}(\vec{r})\; t^{(+,i)} + \hat{p}_f^{(+)}(\vec{r}), \qquad \vec{r} \in D^{(+)},\end{aligned} \tag{4.2}$$

where n_λ is the total number of levels and i is the corresponding number of the considered level. In a similar manner with bounded domains, the functions $\Phi_w^{(+,i)}$ represent *a priori* defined unbounded wave functions and $t_w^{(+,i)}$ are their corresponding contribution factors. The term $\Phi^{(+,i)}(\vec{r})$ is the row vector collecting unbounded wave functions within level i and $t^{(+,i)}$ is the column vector collecting weighting factors. Finally, $\hat{p}_f^{(\bullet)}$ represents a particular solution resulting from acoustic source terms q in the right hand side of the inhomogeneous Helmholtz equation (2.1).

The wave function selections for the bounded and unbounded subdomains are identical to the conventional WBM and can be found in Section 2.4.1.

4.1.2 Evaluation of boundary and interface conditions

To build up the system of algebraic equations, a weighted residual formulation is enforced on the boundary and interface conditions. The interface conditions are needed to satisfy the continuity among interfaces and couple acoustic subdomains. For the boundary residuals, equations (2.3), (2.4) and (2.5) are used. For the interface residuals, various coupling algorithms are available in the WBM literature [105]. As an alternative to equation (2.28), a pressure-velocity coupling condition is given in this chapter. An interface residual, $R_I^{(\gamma,\beta)}$, between two subdomains γ and β can be defined as :

$$\vec{r} \in \Gamma_I : R_I^{(\gamma,\beta)}\left(p^{(\gamma)}(\vec{r}), p^{(\beta)}(\vec{r})\right) = \begin{cases} p^{(\gamma)}(\vec{r}) - p^{(\beta)}(\vec{r}) = 0, & \vec{r} \in \{\Gamma_{Ip}\}, \\ \mathcal{L}_v(p^{(\gamma)}(\vec{r})) + \mathcal{L}_v(p^{(\beta)}(\vec{r})) = 0 & \vec{r} \in \{\Gamma_{Iv}\}, \end{cases} \tag{4.3}$$

where Γ_{Ip} and Γ_{Iv} represent interfaces with enforced pressure and velocity continuities, respectively. In addition, γ and β represent a general subdomain

definition, which can be replaced by bounded subdomains, α, or unbounded subdomains, $+, i$. Therefore, the given continuity condition can be used for both bounded-bounded and bounded-unbounded subdomain interfaces. The pressure-velocity coupling is defined such that either a pressure continuity or a velocity continuity can be defined for one side of the interface. Moreover, if one side is assigned a pressure continuity, the other should have velocity continuity and vice versa.

With boundary and interface conditions defined, the weighted residual formulation can be formed. The key point for the ML-WBM is that the coupling of the different levels happens on the truncation circles. For this reason, a distinction for the residuals on truncation circles should be made. By representing the boundaries that are on the truncation as $\Gamma_{\bullet,t} = \Gamma_{v,t} \cup \Gamma_{p,t} \cup \Gamma_{Z,t}$ and the interfaces as $\Gamma_{I,t}$ (see Figure 4.1) the Multi-Level residuals are defined as:

$$R_{\bullet}^{ML(\gamma)}(p^{(\gamma)}(\vec{r})) =$$

$$\begin{cases} R_{\bullet}^{(+)}\left(\sum_{i=1}^{n_\lambda} \Phi^{(+,i)}(\vec{r})\, t^{(+,i)}\right), & \vec{r} \in \{\Gamma_{\bullet,t}\}, \\ R_{\bullet}^{(\alpha)}(\Phi^{(\alpha)}(\vec{r})\, t^{(\alpha)}), & \vec{r} \notin \{\Gamma_{\bullet,t}\}, \end{cases} \quad \text{with } \bullet = v,\ p \text{ or } Z, \tag{4.4}$$

$$R_I^{ML(\gamma,\beta)}\left(p^{(\gamma)}(\vec{r}),\, p^{(\beta)}(\vec{r})\right) =$$

$$\begin{cases} R_I^{(+,\beta)}\left(\sum_{i=1}^{n_\lambda} \Phi^{(+,i)}(\vec{r})\, t^{(+,i)},\, \Phi^{(\beta)}(\vec{r})\, t^{(\beta)}\right), & \vec{r} \in \{\Gamma_{I,t}\}, \\ R_I^{(\alpha,\beta)}\left(\Phi^{(\alpha)}(\vec{r})\, t^{(\alpha)},\, \Phi^{(\beta)}(\vec{r})\, t^{(\beta)}\right), & \vec{r} \notin \{\Gamma_{I,t}\}. \end{cases} \tag{4.5}$$

For each subdomain, the residual functions are orthogonalized with respect to a weighting function $\tilde{t}^{(\gamma)}$ or its derivative. For N_D number of subdomains and $N_I^{(\gamma)}$ number of interfaces for each subdomain, the weighted residual formulation is written as:

$$\begin{aligned} \sum_{\gamma=1}^{N_D} \Big[& \int_{\Gamma_v^{(\gamma)}} \tilde{t}^{(\gamma)}(\vec{r})\, R_v^{ML(\gamma)}(p^{(\gamma)}(\vec{r}))\mathrm{d}\Gamma \\ & + \int_{\Gamma_Z^{(\gamma)}} \tilde{t}^{(\gamma)}(\vec{r})\, R_Z^{ML(\gamma)}(p^{(\gamma)}(\vec{r}))\mathrm{d}\Gamma \\ & + \int_{\Gamma_p^{(\gamma)}} -\mathcal{L}_v^{(\gamma)}(\tilde{t}^{(\gamma)}(\vec{r}))\, R_p^{ML(\gamma)}(p^{(\gamma)}(\vec{r}))\mathrm{d}\Gamma \\ & + \sum_{\beta=1,\beta\neq\gamma}^{N_I^{(\gamma)}} \int_{\Gamma_I^{(\gamma,\beta)}} \tilde{t}^{(\gamma)}(\vec{r})\, R_I^{ML(\gamma,\beta)}\left(p^{(\gamma)}(\vec{r}),\, p^{(\beta)}(\vec{r})\right)\mathrm{d}\Gamma \Big] = 0. \end{aligned} \tag{4.6}$$

It should be noted that the last term contains non-zero elements only for subdomains that have a common interface. For the rest, it gives empty sets. Irrespective of the type of the subdomain, i.e. bounded or unbounded, the weighting functions are chosen as the same set of acoustic wave functions defined for the corresponding subdomain :

$$\tilde{t}^{(\gamma)}(\vec{r}) = \sum_{w=1}^{n_w^{(\gamma)}} \Phi_w^{(\gamma)}(\vec{r}) t_w^{(\gamma)} = \Phi^{(\gamma)}(\vec{r})\, t^{(\gamma)}. \tag{4.7}$$

Substitution of the pressure expansions (4.1) or (4.2) and the weighting function expansion (4.7) into the weighted residual formulation (4.6) yields a system of equations, of which the solution provides the unknown weighting factors of the *a priori* defined wave functions.

4.1.3 Solution and post-processing

To calculate the field variables, the pressure expansions in equations (4.1) or (4.2) are used with their calculated weighting factors. Derived quantities can be easily calculated from the analytical derivative of equations (4.1) or (4.2), without additional loss of accuracy.

4.2 The ML-WBM with symmetric boundary conditions

The symmetry conditions defined in this chapter are based on the geometrical symmetry of the scatterers relative to a certain axis/plane in Cartesian coordinates. By using symmetric boundary conditions, the model sizes can be reduced considerably. One of the application fields that benefits most from the symmetric boundary conditions is the modeling of large sonic crystals. They are, in general, composed of large number of scatterers that are distributed symmetrically. Using symmetric boundary conditions for such problems helps extending the limits of the models that are feasible to calculate, especially in the case of acoustic lens design, where huge number of function evaluations are needed.

Symmetric boundary conditions for the ML-WBM are derived for both 2D and 3D problems. The detailed derivation of the 2D models are presented first. Subsequently, symmetric boundary conditions for 3D problems are presented. Only the necessary definitions for the extension is presented to avoid repetition.

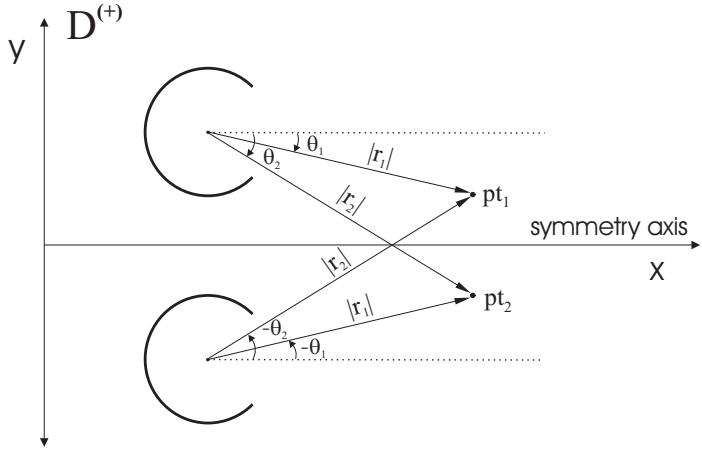

Figure 4.2: A 2D symmetric acoustic problem

4.2.1 Symmetric boundary conditions and field variables for 2D problems

Figure 4.2 shows two scatterers that are symmetric to each other. For the sake of clarity, the symmetric boundary conditions are derived for this system first and then generalized. It should be noted that, in order for symmetric boundary conditions to work, the excitation to the system should be symmetric as well. In such a configuration, two arbitrary points pt_1 and pt_2 (see Figure 4.2), that are symmetric to each other have the same pressure values. If they are in the exterior domain, $D^{(+)}$, they can be written in terms of pressure approximations given in equation (4.2). The pressure expansions for two symmetric points, in terms of c- and s-sets from equation (2.17) are written as follows:

$$
\begin{aligned}
&\sum_{w_c=0}^{n_{w_c}^{(1)}} \Phi_{w_c}^{(+,1)}(r_1,\theta_1)t_{w_c}^{(+,1)} + \sum_{w_s=1}^{n_{w_s}^{(1)}} \Phi_{w_s}^{(+,1)}(r_1,\theta_1)t_{w_s}^{(+,1)} + \\
&\sum_{w_c=0}^{n_{w_c}^{(2)}} \Phi_{w_c}^{(+,2)}(r_2,\theta_2)t_{w_c}^{(+,2)} + \sum_{w_s=1}^{n_{w_s}^{(2)}} \Phi_{w_s}^{(+,2)}(r_2,\theta_2)t_{w_s}^{(+,2)} = \\
&\sum_{w_c=0}^{n_{w_c}^{(1)}} \Phi_{w_c}^{(+,1)}(r_2,-\theta_2)t_{w_c}^{(+,1)} + \sum_{w_s=1}^{n_{w_s}^{(1)}} \Phi_{w_s}^{(+,1)}(r_2,-\theta_2)t_{w_s}^{(+,1)} + \\
&\sum_{w_c=0}^{n_{w_c}^{(2)}} \Phi_{w_c}^{(+,2)}(r_1,-\theta_1)t_{w_c}^{(+,2)} + \sum_{w_s=1}^{n_{w_s}^{(2)}} \Phi_{w_s}^{(+,2)}(r_1,-\theta_1)t_{w_s}^{(+,2)},
\end{aligned}
\tag{4.8}
$$

where the left hand side of the equation represents the pressure at pt_1, the right hand side represents the pressure at pt_2 and each row represents the pressure contribution from one scatterer. Assigning the same number of wave functions to each scatterer makes $n_{w_c}^{(1)} = n_{w_c}^{(2)}$ and $n_{w_s}^{(1)} = n_{w_s}^{(2)}$. On a side note, this choice is not strictly mandatory for a ML-WBM model. However, considering the symmetry of the pressure fields, it is the most convenient one.

Using negative angle identities of the cosine and sine functions makes it possible to relate the wave functions as follows, provided that the values for w_c and w_s for two subdomains are the same:

$$\Phi_{w_c}^{(+,1)}(r_1,\theta_1) = \Phi_{w_c}^{(+,2)}(r_1,-\theta_1) \quad , \quad \Phi_{w_s}^{(+,1)}(r_1,\theta_1) = -\Phi_{w_s}^{(+,2)}(r_1,-\theta_1). \tag{4.9}$$

By using the above relations, it is possible to rearrange equation (4.8) as follows:

$$\begin{aligned}
&\sum_{w_c=0}^{n_{w_c}^{(1)}} \left[\Phi_{w_c}^{(+,1)}(r_1,\theta_1)\left(t_{w_c}^{(+,1)} - t_{w_c}^{(+,2)}\right)\right] + \sum_{w_s=1}^{n_{w_s}^{(1)}} \left[\Phi_{w_s}^{(+,1)}(r_1,\theta_1)\left(t_{w_s}^{(+,1)} + t_{w_s}^{(+,2)}\right)\right] + \\
&\sum_{w_c=0}^{n_{w_c}^{(1)}} \left[\Phi_{w_c}^{(+,1)}(r_2,\theta_2)\left(t_{w_c}^{(+,2)} - t_{w_c}^{(+,1)}\right)\right] + \sum_{w_s=1}^{n_{w_s}^{(1)}} \left[\Phi_{w_s}^{(+,1)}(r_2,\theta_2)\left(t_{w_s}^{(+,2)} + t_{w_s}^{(+,1)}\right)\right] \\
&= 0.
\end{aligned} \tag{4.10}$$

For the above equation to hold for any given two symmetric points, the unknown contribution factors should satisfy the following statement:

$$t_{w_c}^{(+,1)} = t_{w_c}^{(+,2)} \quad \bigcup \quad t_{w_s}^{(+,1)} = -t_{w_s}^{(+,2)}. \tag{4.11}$$

It is possible to generalize equation (4.11) to any number of symmetric scatterers.

The exterior pressure expansion (4.2) can be rewritten by taking advantage of equation (4.11). Firstly it is written as the sum of pressure values coming from the scatterers in the upper symmetry plane and the lower symmetry plane:

$$\begin{aligned}
\hat{p}^{(+)}(\vec{r}) = \hat{p}_f^{(+)}(\vec{r}) \; &+ \sum_{i=1}^{n_\lambda/2} \left[\sum_{w_c=0}^{n_{w_c}^{(i)}} \Phi_{w_c}^{(+,i)}(\vec{r})\, t_{w_c}^{(+,i)} + \sum_{w_s=1}^{n_{w_s}^{(i)}} \Phi_{w_s}^{(+,i)}(\vec{r})\, t_{w_s}^{(+,i)}\right] \\
&+ \sum_{i=(n_\lambda/2)+1}^{n_\lambda} \left[\sum_{w_c=0}^{n_{w_c}^{(i)}} \Phi_{w_c}^{(+,i)}(\vec{r})\, t_{w_c}^{(+,i)} + \sum_{w_s=1}^{n_{w_s}^{(i)}} \Phi_{w_s}^{(+,i)}(\vec{r})\, t_{w_s}^{(+,i)}\right].
\end{aligned} \tag{4.12}$$

By renaming the wave functions that correspond to the scatterers on one side of the symmetry axis as $\Phi_{w_c}^{(+,i)sym} = \Phi_{w_c}^{(+,i+n_\lambda/2)}$, $\Phi_{w_s}^{(+,i)sym} = \Phi_{w_s}^{(+,i+n_\lambda/2)}$ and

using equation (4.11), the above equation can be rewritten as:

$$\hat{p}^{(+)}(\vec{r}) = \hat{p}_f^{(+)}(\vec{r}) \; + \sum_{i=1}^{n_\lambda/2} \left[\sum_{w_c=0}^{n_{w_c}^{(i)}} \left(\Phi_{w_c}^{(+,i)}(\vec{r}) + \Phi_{w_c}^{(+,i)sym}(\vec{r}) \right) \; t_{w_c}^{(+,i)} \right. \\ \left. + \sum_{w_s=1}^{n_{w_s}^{(i)}} \left(\Phi_{w_s}^{(+,i)}(\vec{r}) - \Phi_{w_s}^{(+,i)sym}(\vec{r}) \right) \; t_{w_s}^{(+,i)} \right]. \tag{4.13}$$

Finally, the exterior pressure expansion can be written in the vector format as:

$$\hat{p}^{(+)}(\vec{r}) = \hat{p}_f^{(+)}(\vec{r}) \; + \sum_{i=1}^{n_\lambda/2} \left(\Phi^{(+,i)}(\vec{r}) + \Phi^{(+,i)sym}(\vec{r}) \right) \; t^{(+,i)}. \tag{4.14}$$

For writing the bounded pressure expansion (4.1) using symmetry conditions, a similar reasoning can be followed by choosing two symmetric points within bounded subdomains. However, since the pressure values within a bounded domain are not directly subject to the pressure values coming from the other levels, the definition given in equation (4.1) does not change. The effect of symmetric boundary conditions on the bounded subdomains happens through the interfaces that couple bounded and unbounded subdomains.

4.2.2 Evaluation of boundary and interface conditions

The boundary residuals defined for ML-WBM can be rewritten by using equation (4.14) as follows:

$$R_\bullet^{MLsym(\gamma)}(p^{(\gamma)}(\vec{r})) = \\ \begin{cases} R_\bullet^{(+)} \left(\sum_{i=1}^{n_\lambda/2} \left(\Phi^{(+,i)}(\vec{r}) + \Phi^{(+,i)sym}(\vec{r}) \right) \; t^{(+,i)} \right), & \vec{r} \in \{\Gamma_{\bullet,t}\}, \\ R_\bullet^{(\alpha)}(\Phi^{(\alpha)}(\vec{r}) \; t^{(\alpha)}), & \vec{r} \notin \{\Gamma_{\bullet,t}\}, \end{cases} \tag{4.15}$$

where $\bullet = v$, p or Z. The interface residual can be rewritten as follows:

$$R_I^{MLsym(\gamma,\beta)} \left(p^{(\gamma)}(\vec{r}), p^{(\beta)}(\vec{r}) \right) = \\ \begin{cases} R_I^{(+,\beta)} \left(\sum_{i=1}^{n_\lambda/2} \left(\Phi^{(+,i)}(\vec{r}) + \Phi^{(+,i)sym}(\vec{r}) \right) \; t^{(+,i)}, \Phi^{(\beta)}(\vec{r}) t^{(\beta)} \right), & \vec{r} \in \{\Gamma_{I,t}\}, \\ R_I^{(\alpha,\beta)} \left(\Phi^{(\alpha)}(\vec{r}) t^{(\alpha)}, \Phi^{(\beta)}(\vec{r}) t^{(\beta)} \right), & \vec{r} \notin \{\Gamma_{I,t}\}. \end{cases} \tag{4.16}$$

Subsequently, the weighted residual formulation can be written for $N_D/2$ number of subdomains, instead of N_D as:

$$\begin{aligned}
&\sum_{\gamma=1}^{N_D/2} \Big[\int_{\Gamma_v^{(\gamma)}} \tilde{t}^{(\gamma)}(\vec{r})\, R_v^{MLsym(\gamma)}(p^{(\gamma)}(\vec{r}))\mathrm{d}\Gamma \\
&+ \int_{\Gamma_Z^{(\gamma)}} \tilde{t}^{(\gamma)}(\vec{r})\, R_Z^{MLsym(\gamma)}(p^{(\gamma)}(\vec{r}))\mathrm{d}\Gamma \\
&+ \int_{\Gamma_p^{(\gamma)}} -\mathcal{L}_v^{(\gamma)}(\tilde{t}^{(\gamma)}(\vec{r}))\, R_p^{MLsym(\gamma)}(p^{(\gamma)}(\vec{r}))\mathrm{d}\Gamma \\
&+ \sum_{\beta=1,\beta\neq\gamma}^{N_I^{(\gamma)}} \int_{\Gamma_I^{(\gamma,\beta)}} \tilde{t}^{(\gamma)}(\vec{r})\, R_I^{MLsym(\gamma,\beta)} \left(p^{(\gamma)}(\vec{r})\,,\, p^{(\beta)}(\vec{r})\right) \mathrm{d}\Gamma \Big] = 0.
\end{aligned} \tag{4.17}$$

The choice of weighting functions does not change, such that equation (4.7) stays the same. Consequently, construction of the weighted residual formulation yields a system of equations, of which the solution provides the unknown weighting factors.

4.2.3 Solution and post-processing

The total system matrix size changes from $N \times N$ to $N/2 \times N/2$. For post-processing points in unbounded domains, equation (4.14) is used. For the points in bounded subdomains, equation (4.1) is the one. However, one should be careful about the definition of the coordinate system for the bounded subdomains below the symmetry axis. The coordinate system should be defined as being symmetric to the ones in the upper plane, in order to be able to use the same weighting factors for the wave functions.

4.2.4 Extension of symmetric boundary conditions to 3D problems

The symmetry in 3D space can be exploited in two axes at the same time, i.e. relative to a plane, as compared to a single axis in 2D problems. As mentioned before, the symmetry conditions derived here refer to the symmetry in Cartesian coordinates. As it can be seen from Figure 2.3, y axis symmetry can be obtained by writing the position vector with $-\phi$ and z axis, with $-\theta$. The pressure expansion can be rewritten by using the y axis symmetry and z axis symmetry, which results in the expansion to have four elements, including

the contribution from scatterers that have both y and z axes symmetries:

$$\hat{p}^{(+)}(r,\theta,\phi) = \sum_{i=1}^{n_\lambda/4} \left(\sum_{l=0}^{l_{max}^{(i)}} \sum_{m=-l}^{l} \Phi_{lm}^{(+,i)}(\boldsymbol{r}) + \Phi_{lm}^{(+,i)\ y\text{-}sym}(\boldsymbol{r}) + \Phi_{lm}^{(+,i)\ z\text{-}sym}(\boldsymbol{r}) + \Phi_{lm}^{(+,i)\ yz\text{-}sym}(\boldsymbol{r}) \right) t_{lm}^{(+,i)}, \tag{4.18}$$

where,

$$\Phi_{lm}^{(+,i)\ y\text{-}sym}(\boldsymbol{r}) = (-1)^m \ \Phi_{lm}^{(+,i+n_\lambda/4)}(\boldsymbol{r}), \tag{4.19}$$

$$\Phi_{lm}^{(+,i)\ z\text{-}sym}(\boldsymbol{r}) = \begin{cases} \Phi_{lm}^{(+,i+n_\lambda/2)}(\boldsymbol{r}) & \text{if} \quad P_l^m(\sin(-\theta)) = P_l^m(\sin(\theta)), \\ -\Phi_{lm}^{(+,i+n_\lambda/2)}(\boldsymbol{r}) & \text{if} \quad P_l^m(\sin(-\theta)) = -P_l^m(\sin(\theta)), \end{cases} \tag{4.20}$$

$$\Phi_{lm}^{(+,i)\ yz\text{-}sym}(\boldsymbol{r}) = \begin{cases} (-1)^m \ \Phi_{lm}^{(+,i+3n_\lambda/4)}(\boldsymbol{r}) & \text{if} \quad P_l^m(\sin(-\theta)) = P_l^m(\sin(\theta)), \\ -(-1)^m \ \Phi_{lm}^{(+,i+3n_\lambda/4)}(\boldsymbol{r}) & \text{if} \quad P_l^m(\sin(-\theta)) = -P_l^m(\sin(\theta)). \end{cases} \tag{4.21}$$

An important assumption for the above expressions is the numbering of the corresponding levels. From the first level to the level number $n_\lambda/4$, are the scatterers that form the basis. From $n_\lambda/4+1$ to $n_\lambda/2$ are the levels with y axis symmetry with respect to the basis set. From $n_\lambda/2+1$ to $3n_\lambda/4$ are the levels with z axis symmetry and finally, from $3n_\lambda/4+1$ to n_λ are the levels with both y and z axes symmetries. It should also be noted that, when the corresponding number of the level changes, the coordinate system shifts accordingly, to be able to write the wave functions correctly. This is because all wave functions are defined in the local coordinates of the corresponding level.

By using equation (4.18), the symmetric ML-WBM model can be formed in a same manner with the 2D problems. The difference is that the loop over the levels for residuals are decreased from $n_\lambda/2$ to $n_\lambda/4$ and the loop over the domains are decreased from $N_D/2$ to $N_D/4$. In other words, the system building time reduces to one-fourth as compared to the full model. In addition, the system matrix size reduces from $N \times N$ to $N/4 \times N/4$, where N is the total number of degrees of freedom for the full model.

4.3 Conclusion

The ML-WBM modeling principles are reviewed in this chapter. The ML-WBM brings more flexibility to the WBM framework by decomposing the problem domain to different levels. For multiple scattering problems, this alleviates the requirement to model the vast area between scatterers, which eventually leads to smaller models and needs less modeling effort.

After the review of the method, symmetric boundary conditions are derived for 2D and 3D multiple scattering problems. As such, the efficiency of the ML-WBM is increased further for symmetric problems. The importance of symmetric boundary conditions and how they extend the limits of the ML-WBM is demonstrated in the next chapter, where the ML-WBM is used for acoustic lens designs.

Chapter 5

Optimization of Acoustic Lenses using the ML-WBM

This chapter presents a novel application of the ML-WBM on the design of acoustic lenses. The lens designs are based on sonic crystals (SCs), which are defined as periodically distributed scatterers in a fluid. As such, the considered problem is a multiple scattering problem with large number of scatterers. Problem settings of these kind create challenging cases in terms of numerical modeling. When optimization of acoustic lenses is added to the context, the problem becomes even more demanding and presents a good application case to test the ML-WBM's capabilities.

What follows is three sections, where the motivation for the acoustic lens designs is given and two different optimization procedures are presented. The first design procedure is based on optimizing the shape of unit scatterers. The second design procedure is based on creating vacancies on predefined grids of scatterers.

5.1 Motivation

The field of acoustic metamaterials has attracted considerable attention in recent years. Manipulating the properties of materials in ways that are not possible through conventional constructions opens ways to new applications and devices. This has been the case for the applications of SCs. An interesting property of SCs is that they create band gaps, where the transmission of sound is blocked or limited. These band gaps can be obtained either through a Bragg scattering mechanism, where half the wavelength fits the distance between the periodic scatterers to form the first band gap, or by utilizing local resonances. Such band gaps lead to applications of sound barriers, sound filters etc. [84, 113, 95, 25, 89, 111]. Another interesting property of SCs is

their ability to focus sound. This can happen in various ways. Firstly; in the long wave regime, they act as homogeneous materials with high density and low speed of sound. As such, they can be used to create acoustic lenses with high positive refraction index [21, 83, 61]. Secondly; superlenses can be created with negative refraction index [150, 60]. This happens before the second band gap for sonic crystals that have local resonances. A third way is to focus sound by changing the local density within the SCs and tunnel the waves to focus. Such lenses are called gradient index lenses [29, 94, 126]. Finally, acoustic lenses can be created by using the complex multiple scattering properties of scatterers, where the distribution of scatterers is not following a strict periodicity. These types of configurations are referred to as scattering acoustical elements (SAEs) [62, 63, 64, 114]. Because of the complex nature of these lenses, they are created through an inverse design procedure. The idea is to create vacancies on a predefined grid of periodic scatterers to generate topologies that focus sound at a given frequency and focal point. A genetic algorithm (GA) is used to search the possible configurations and eventually decide on the positions of the scatterers. The focus of this chapter is on the first and fourth family of lenses, as described above. Three main innovations are proposed for those.

The first innovation is related to the first family of acoustic lenses with high positive refraction index. In recent articles, most of the acoustic lenses have been based on closed geometries, such as circular or spherical scatterers and in some cases, on scatterers with small apertures. With the new design procedure presented in the next section that optimizes the shape of the unit scatterer, innovative lens designs are obtained, which comprise structures with large apertures, i.e. scatterers that resemble satellite dishes, in addition to scatterers with small apertures.

The second and third innovations are related to SAEs. Similar to the first family of acoustic lenses, SAE designs have also been based on closed scatterers so far. In a first step, innovative designs for 2D SAEs that use Helmholtz resonators as unit scatterers are presented in Section 5.3. The new designs are compared to the ones that use circular scatterers and it is demonstrated that the former perform considerably better, especially at low frequencies, where the local resonances are utilized. The benefits of using the ML-WBM are also demonstrated in this design context. In a second step, the acoustic lens designs are extended to 3D problems. Lenses that are based on spherical scatterers and cup shaped scatterers are designed directly in 3D space, which establishes the last innovation. They are presented as an alternative to the lenses in literature, where the designs have been done in 2D space and rotated in z axis to create 3D lenses.

The ability of the ML-WBM to efficiently model moderately complex geometries plays an important role in the exploration of the aforementioned innovations. The modeling of acoustic lenses is not trivial, especially when they are based on Helmholtz resonators. This is mainly because of the high number of scatterers and the resulting large system of equations. The main trend in modeling SCs is to use multiple scattering theory [128], yet this is only possible

if the scatterer shapes allow analytical solutions. For more complex shapes, the Finite Element Method [153] in frequency domain or the Finite Difference Method [70] in time domain has been used. However, both of them need special boundary conditions to be able to solve unbounded problems. Moreover, in the context of a design procedure, creating vacancies on the predefined topologies or changing the shape of the unit scatterers needs re-meshing of the domain for every iteration of the optimization since both are domain discretization methods. Considering that thousands of function evaluations are needed in such cases, these methods become impractical. An option might be to use the Boundary Element Method [149] because of its inherent ability to solve unbounded problems and that it is a boundary discretization method. On the other hand, it can be still expensive to solve because of the large problem size.

The ML-WBM suits very well for the considered multiple scattering problem. It is more efficient as compared to the Boundary Element Method for multiple scattering problems with moderately complex scatterers [133]. It also inherently satisfies the Sommerfeld radiation condition. In the context of design of SAEs, the ML-WBM becomes even more attractive. Building up a model which has vacancies on predefined SC grids only needs a subset of the full grid model. In other words, constructing the system of equations is not needed for every iteration. This property of the ML-WBM brings a huge performance boost in the optimization concept, both because there is no time lost for constructing the system of equations and because the number of unknowns are rather low compared to element based methods [105].

5.2 Acoustic lens designs through shape optimization of unit scatterer

In this section, a new optimization procedure is proposed for designing acoustic lenses. Firstly, the effect of different closure angles of circular scatterers on the focusing frequencies are examined. The examined scatterers with large closure angles are similar to the ones examined by Hu *et al* [72] and have local resonances. Scatterers that are highly open are investigated as well. These scatterers are circle segments that resemble satellite dishes and they have no local resonance effect. After observing the effect of different closure angles on the focusing frequencies, this feature is exploited for designing acoustic lenses. A design procedure where the design variable is chosen as the degree of openness/closedness of the scatterer is proposed. Subsequently, the procedure is improved by adding the lattice parameters, i.e. the spacing of the scatterers in x and y directions, to the design variables. Figure 5.1 shows a representative configuration of periodic scatterers and the corresponding WBM model.

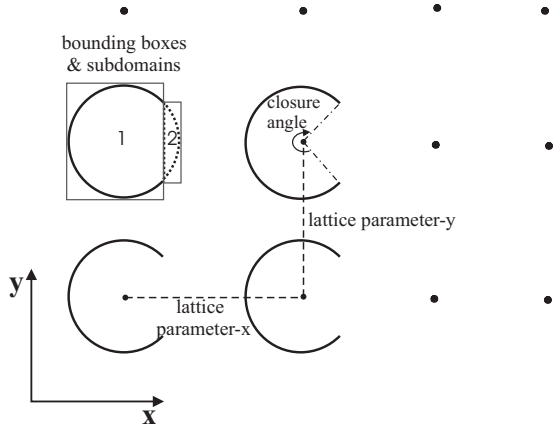

Figure 5.1: Graphic representation of periodic scatterers. The WBM bounding boxes and subdomains are shown for the top left scatterer. The design variables are also shown: lattice parameters in x and y directions and the closure angle of a unit scatterer.

5.2.1 Investigation on the effect of different closure angles on the focusing frequencies

Before discussing the optimization procedure, it is important to examine the effect of different closure angles of the scatterers on the focusing frequency. This provides a better understanding of what one can expect from the optimization. Figure 5.2 shows the observations on using four different acoustic lenses with unit scatterers of varying closure angles. A fully closed scatterer (a cylinder) and scatterers of 270°, 180° and 100° closure are used as unit scatterers. The radius of the scatterers is 0.02 m while the lattice parameter is chosen to be 0.05 m. All scatterers are rigid and the thickness of the walls is assumed to be zero.

Each subfigure contains a band structure figure and a FRF figure. Band structure figures illustrate the wave propagation characteristics of the infinite periodic structure with the corresponding unit scatterer. These curves are calculated by a unit cell modeling strategy, i.e. Bloch-Floquet periodic boundary conditions are applied on a FEM model of the unit scatterer [28]. They provide information on the frequencies and the directions the waves are allowed to travel within the SC or the frequencies the waves are blocked. The dot-dashed curves on these figures illustrates how the sound travels in air. Having a slope smaller than the slope of the air means that the speed of sound within the SC is lower as compared to air. Adjacent to the band structure figures are the FRF curves, calculated for a finite number of scatterers as seen in Figure 5.3. There are in total 45 scatterers with 5 columns and 9 rows. The excitation to the system is a plane wave traveling in the negative x direction. The post-processing points are chosen as 100 equally spaced points from 0.05

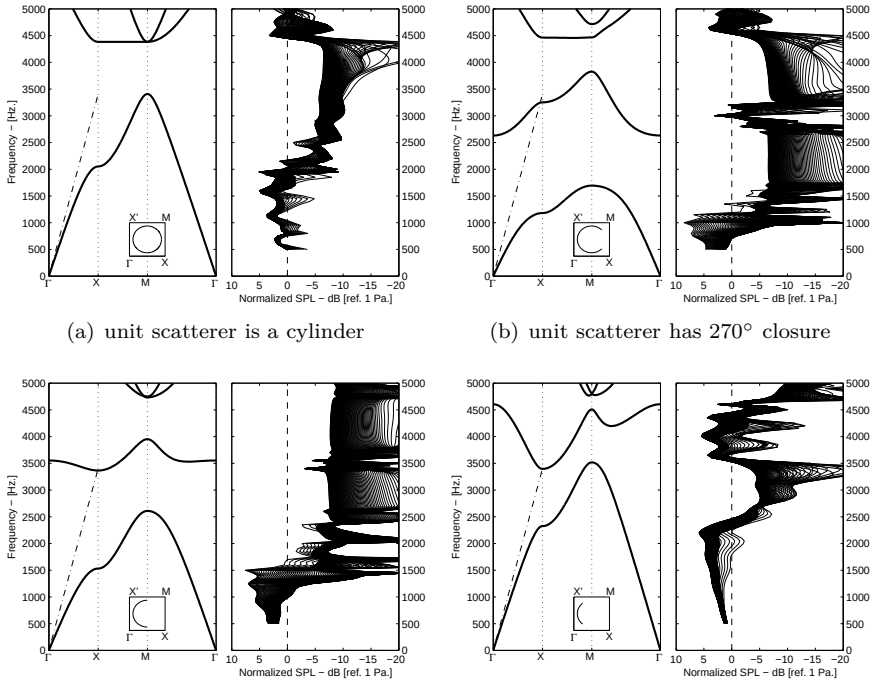

(a) unit scatterer is a cylinder

(b) unit scatterer has 270° closure

(c) unit scatterer has 180° closure

(d) unit scatterer has 100° closure

Figure 5.2: Band structure curves are presented next to FRF curves with 100 post-processing points for 45 scatterers (9 rows and 5 columns). The dot-dashed curves on the band structure figures represent the dispersion curve of sound traveling in air. The geometry of the unit scatterer is presented as inlet figures, together with the path followed for band structure curves for ease of visualization.

m to 2.05 m in front of the acoustic lens on the y axis.

The indirect variational BEM is used to model the 45 scatterer configuration. These models are later used to have a reference for the ML-WBM calculations. For all configurations, the BEM models are using linear elements and are valid up to 30 kHz by using the 10 elements per wavelength rule.

The normalized sound pressure level (SPL) in dB is defined as follows:

$$P(\vec{r}) = 20 \log_{10} \left(\frac{|p(\vec{r})|}{|p_0(\vec{r})|} \right), \tag{5.1}$$

where $|p_0(\vec{r})|$ is the amplitude of the pressure at the given position without the acoustic lens and $|p(\vec{r})|$, with the lens. It is equal to 1 Pa with plane wave excitation for all cases in this section.

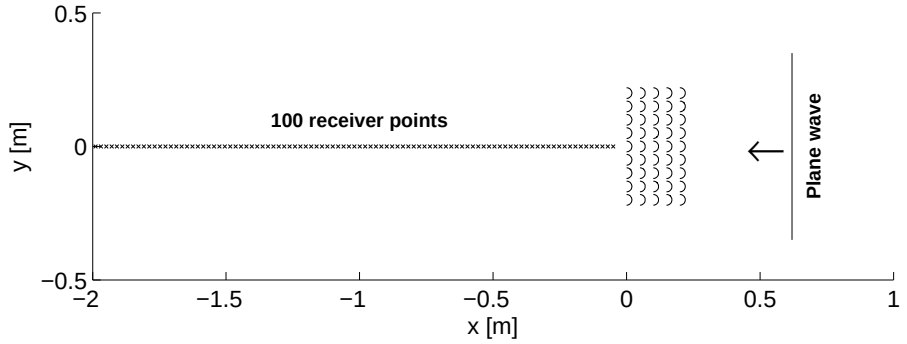

Figure 5.3: The problem setting for FRF calculations with 45 scatterers and 100 receiver points.

The main goal of presenting the band structure and FRF figures side-by-side is to observe how the wave propagates within the SC and see the end result on a finite configuration. For instance, looking at Figure 5.2(a), one can see that at 3500 Hz, band structure figure indicates there is no wave propagation inside the SC for any direction. This can be observed on the adjacent FRF curve as well. At 3000 Hz, the wave propagation is allowed within the SC, however not for the $\Gamma-X$ interval. Since the FRF curves are obtained with an excitation in the x direction (this corresponds to the $\Gamma-X$ interval on the band structure figure), the sound is blocked as well for the finite configuration. Finally, at 1500 Hz, the wave propagation is allowed on the $\Gamma-X$ interval, however the speed of sound is lower than the air. As such, a focusing behavior is observed for the finite configuration.

Having a look at different subfigures, it can be observed that the focusing frequencies move with different closure angles. Case (a) does not have any local resonances and the focusing effect comes just before the first Bragg scattering region, i.e. when the half wave length is equal to the distance between the scatterers and the wave propagation is prohibited. Cases (b) and (c) have local resonances and create strong focusing effects in lower frequencies. When it comes to case (d), it is hard to see any local resonance effect and the focusing effect happens again just before the first Bragg scattering region (in the form of a directional band gap). In the end, whether it is because of local resonances or the Bragg-scattering-type mechanism, the different closure angles of scatterers affect the focusing frequencies for the acoustic lenses and this property can be used for optimization of acoustic lenses.

5.2.2 Optimization of acoustic lenses

In a first step, the closure angle of a unit scatterer is defined as the design variable. The other factors, such as the lattice parameter, the number of

scatterers, scatterer size etc. are kept constant. The objective function is defined as the sound amplification at a given position and frequency as defined in equation (5.1). On a side note, the design variable is defined in a way such that the resulting unit scatterer geometries have self symmetry with respect to their local y axes.

For each iteration, the shape of the scatterers changes which leads to rebuilding of the ML-WBM system. The most suitable strategy for modeling the given scatterer shape is to divide the bounded part of a scatterer into two subdomains (see Figure 5.1). By this way, a steep change in the boundary conditions of the bounded domains is avoided. Consequently, the bounding boxes and the corresponding wave functions are also redefined for each iteration. Since the size of a unit scatterer (and consequently the size of the bounding boxes) is relatively small as compared to the acoustic wavelength, it is not possible to use the typical values for the truncation rule given in equation (2.15). A truncation factor of $T = 50$ is chosen. The full grid models are compared with the reference BEM models defined in the previous subsection for various frequencies and shapes and a relative error less than 1 % is obtained at the focal points by using the following formula:

$$\epsilon(p(\vec{r})) = \frac{|p(\vec{r}) - p_{ref}(\vec{r})|}{|p_{ref}(\vec{r})|}. \tag{5.2}$$

A GA is used as the optimization algorithm. However, the defined procedure can be used with other optimization algorithms as well.

To demonstrate how effective the optimization procedure is, three different frequencies are chosen with three different focal points, resulting in nine different optimization cases. The configuration of 45 scatterers, which is detailed in the previous section, is used for the calculations. Figure 5.5 shows the pressure fields that are obtained through the mentioned optimization cases; namely for the frequencies of 1000 Hz, 1500 Hz and 2000 Hz and for the focal points of 0.1 m, 0.3 m and 0.6 m. The inset texts show the amplification in normalized SPL at the given points. Subsequently, Figure 5.4 shows the resulting shapes for the unit scatterers with the same tabular format of the Figure 5.5. The values are given in degrees that represent how closed the circular geometry is.

For this problem setting, it should be noted that the diffraction effect at the corners of the lens possibly dominates the refraction of the waves for the focusing of sound, in a similar manner as discussed in [65]. This, however, is not a concern here, as the optimization algorithm finds the best topology for focusing, regardless of the underlying mechanism. The obtained amplification levels vary from 4.0 dB to 7.4 dB for different cases, while the resulting scatterer closures vary from 116° to 269°. The scatterers become more closed for the lower frequencies and tend to get more open with increasing frequency. This is expected and it is in agreement with the results given in Figure 5.2. While the change of the focal length can be observed for all the cases, it is more apparent when the focal point is changed from 0.1 m to 0.3 m, as compared to when

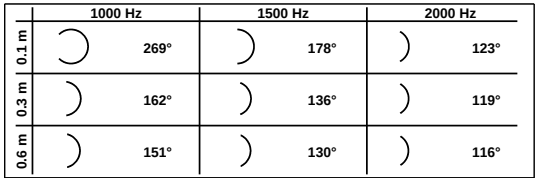

Figure 5.4: The optimization results. The values represent how closed the unit scatterer shape is.

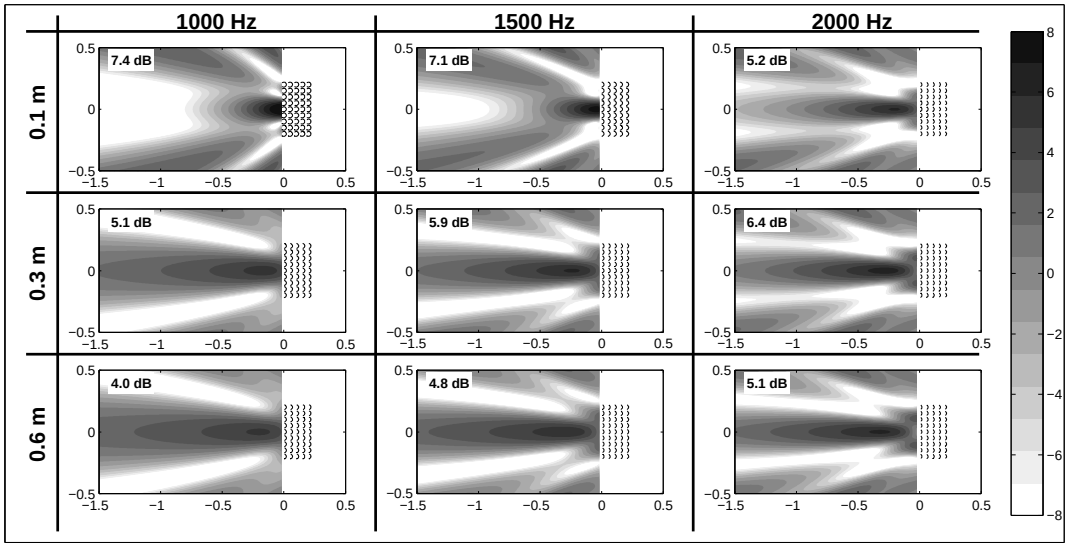

Figure 5.5: Sound pressure fields generated through the design outcomes. The x and y axes of each subfigure are given in meters. The gray scale bar shows the normalized SPL [dB] values (ref. 1 Pa).

it is changed from 0.3 m to 0.6 m. Consequently, this subtle change for the focal lengths of 0.3 m and 0.6 m leads to inefficient designs for the latter, as the values at 0.6 m drop significantly and hint at the limits of the given design procedure.

Being aware of the fact that the focal length depends on various parameters, such as the lattice parameters, exterior shape of the lens etc., it is expected that changing only the unit cell shape would have its limits for acoustic lens design. To provide more freedom to the designs and extend the limits of the procedure, the lattice parameters in x and y direction are casted as design variables, in addition to the unit scatterer shape.

Figure 5.7 shows the resulting pressure fields and the normalized SPL at the focal points using the new approach. Figure 5.6 shows the values for the design variables. In addition to the unit cell geometry information, the lattice parameters in x and y directions are also given.

The normalized SPL values vary from 5.8 dB to 7.7 dB. For every single case, providing more freedom in the design variables results in better outcomes. The improvement can be as high as 1.8 dB, as observed at 1000 Hz with 0.6 m focal length. More importantly, with this new approach, the focal length of the acoustic lens is clearly following the objective points with more accuracy. This leads to better designs with better focusing effects. It can be observed that changing focus from 0.3 m to 0.6 m does not result in significant drops in focusing anymore.

Looking at the unit cell shapes in Figure 5.6, one can see that the resulting shapes are more closed as compared to Figure 5.4. This means that the local resonances are more utilized for the designs, which is in agreement with the better focusing effect in general.

Upper and lower bounds are used for the x and y lattice parameters to limit the search space for the optimization calculations and to converge faster. The values chosen for this case are 0.041 m and 0.2 m, such that the scatterers barely touch each other at the lower bound. As for the upper bound, the value chosen is an arbitrary one, since no space limitations are taken into account. On the other hand, if one has limitations on the space, the upper bound can be lowered as well. To demonstrate this, the cases at 1500 Hz with focal points of 0.3 m and 0.6 m are recalculated with decreased upper bounds. In the first case, the optimized values for x parameters were 0.147 m and 0.181 m and y parameters were 0.069 m and 0.074m. When the upper bound is decreased to 0.1 m, the values for x parameters become 0.052 m and 0.063 m and the values for y parameters become 0.073 m and 0.082 m. The results are summarized in Figure 5.8. Although the normalized SPL values drop as compared to the previous cases, the differences are very small. As such, the proposed design procedure is flexible and allows the consideration of limited spaces.

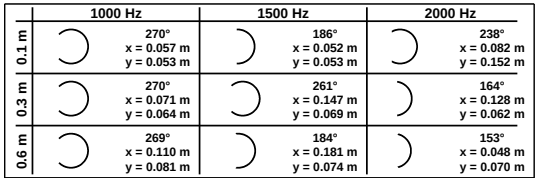

Figure 5.6: The optimization results. The values represent how closed the unit scatterer shape is and the lattice parameters.

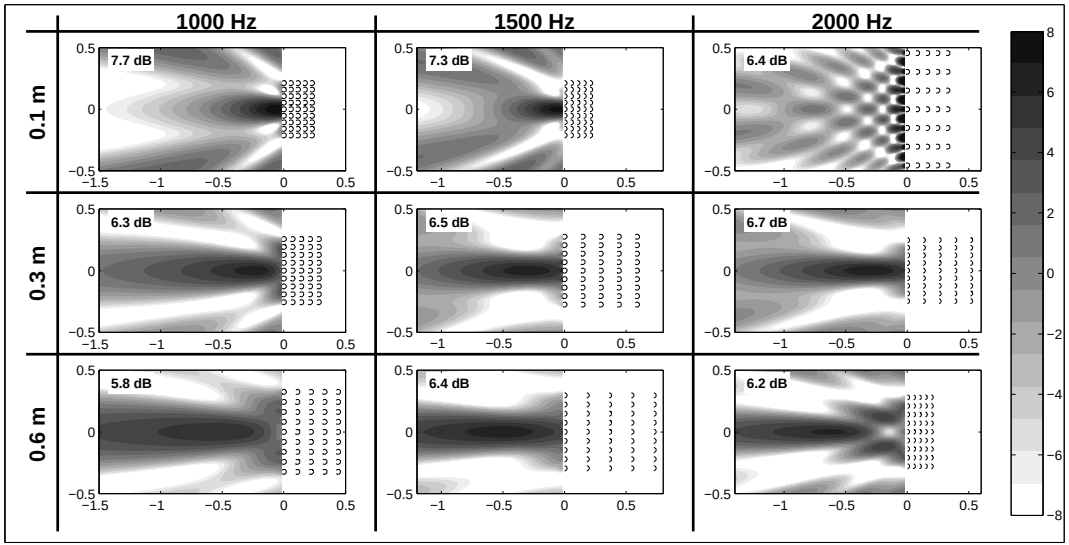

Figure 5.7: Sound pressure fields generated through the design outcomes. The x and y axes of each subfigure are given in meters. The gray scale bar shows the normalized SPL [dB] values (ref. 1 Pa).

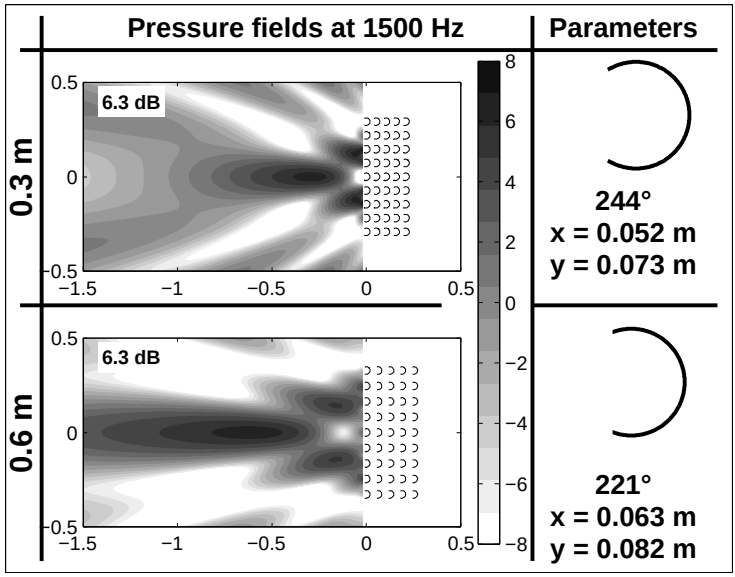

Figure 5.8: On the left: Sound pressure fields. On the right: corresponding optimization results.

5.2.3 Discussion on the results

Various design results are obtained that comprise scatterers with small openings, where the local resonances drive the focusing effect, as well as highly open structures where the local resonances either do not exist or are not dominant. The former has been well documented in literature, while the latter makes an unconventional and interesting case. The main reason that it is interesting is because, in various papers after 2002, the focusing effect is related to the filling fraction of the SCs [21, 61, 72, 126]. While this holds for the corresponding examples in the mentioned papers, the filling fraction for highly open structures is almost zero because of the thin walls. As such, filling fraction does not help in understanding the focusing effect.

While popular recent publications favor relating the focusing effect to filling fraction, there are papers existing in literature that are somewhat less noticed and give a more general explanation for the focusing behavior of periodic scatterers. The paper by Kock and Harvey from the year 1949 [80] investigates various acoustic lens designs, where they demonstrate the focusing effect of arrays of spheres, circular disks and strips among others. In addition, another paper by Amram and Stern [3] extensively investigates the refraction effect of a prism shaped network of rigid strips, where they also present an elaborate theory for the refractive effect of such acoustic devices.

It is known that the refraction/focusing stems from different particle velocities between two media, as it is in optics. The explanations given by Cervera *et al.* [21] and Kock and Harvey [80] for the slow particle velocity within the

SCs are similar. As such, both agree that the reason is the increased effective inertia or density of the fluid, when an array of rigid scatterers exists. Moreover, both explain the increased inertia or density by first examining the case of a moving obstacle in a fluid at rest. In such a case, the obstacle acquires an effective increased inertia which depends on the mass of the fluid displaced by the obstacle (e.g. the increased inertia of a sphere is $\frac{1}{2}$ the mass of the displaced fluid and the increased inertia of a cylinder is equal to the mass of the displaced fluid [85]). If, instead, the obstacle is fixed and the fluid is in motion, the fluid acquires the increased mass by using the same relation, which leads to increased effective density.

The difference is that, Cervera *et al.* keep the explanation of the increased density to the cylinders. As such, the effective increased density is formulated by considering the mass of the fluid displaced by a moving cylinder, which is equal to $\pi\rho_0 r^2$. This relation is equal to the cross section of the cylinder and eventually, it leads to the definition of effective density in terms of filling fraction. On the other hand, Kock and Harvey give a more general explanation. They define refraction index of various obstacles such as spheres, discs and strips. In that, the effective density is not always related to filling fraction. For instance, the mass of the displaced fluid by a moving strip is equal to $\pi\rho_0 b^2$, where b is the half-breadth of the strip. This is followed by the definition of effective density, which is related to the number of strips per unit area and not to the volumetric filling fraction. In short, the more general explanation given by Kock and Harvey covers open structures and states that the increased effective density of the fluid is not always related to the filling fraction.

Applying the same reasoning to come up with an analytical representation for the effective density and eventually refraction index for the presented design outcomes are not trivial, because of the complex shapes. Hence, the choice of the unit scatterer shape is made through optimization. On the other hand, the numerical and experimental examinations of open structures such as strips, which are also studied in [3], give us a deeper understanding of underlying physics and support the presented design outcomes.

On a side note, the proposed design procedure can be used in the context of acoustic filters and sound barriers. An acoustic barrier that uses multiple local resonances can be designed to block the sound in a wide frequency range. This can be achieved by assigning the shape of the scatterers in each row as a separate design variable.

5.3 Acoustic lens designs through vacancy optimization

The acoustic lens design procedure used in this section follows the same principles proposed by Håkansson *et al.* [66]. The objective is to find the most suitable topology of a SC that focuses sound at a given focal point and

frequency. The designs are done by creating vacancies, i.e. removing scatterers, on a predefined grid of scatterers. As such, the size and shape of the scatterers and the lattice parameter are kept constant. A GA is used to decide on the position of the vacancies, by assigning the existence of a scatterer to a design variable. The quantity that is used to evaluate the performance of a lens is the same as defined in equation (5.1). The excitation to the system is a plane wave propagating along the x axis with an amplitude of 1 Pa.

5.3.1 Genetic algorithm

Since the optimization problem at hand is defined by existence of scatterers, it is a combination of discrete problems, where each discrete problem has two possibilities. Consequently, every scatterer is assigned to a one-bit gene, i.e. 1 or 0. An array of genes forms a chromosome, which represents the topology for the problem at hand. For a system of 40 scatterers, the number of possible topology configurations is 2^{40}. Executing such a huge number of function evaluations is not feasible. This is where the use of GA brings a big advantage. Using GA, it is possible to search the solution space very effectively with rather low number of function evaluations. The search is executed through arrays of chromosomes called generations. With each generation, the chromosomes mutate, crossover with each other or survive as they are. As the generations pass, the best chromosomes survive and the weak ones are eliminated which eventually leads to the optimal solution. The disadvantage of GA is that finding the global optimum is not always guaranteed. Therefore, one should be cautious when using GA. With that stated, getting a solution that is representative, if not the optimum, is enough for demonstrating the purposes of this section. The results presented in the next subsections are obtained by running the GA multiple times with large generation sizes (for instance, each generation consists of 500 chromosomes, which comprise 40 one-bit genes for the 2D examples) and by making sure every run is converged within themselves. The convergence criteria for all the simulations are based on the weighted average change in the fitness function. The algorithm stops once the change is below a certain threshold, i.e. when all the chromosomes become similar. The GA used in this paper is based on the GA toolbox of the Matlab 2010 software [96]. The threshold value is kept at Matlab's default, i.e. "function tolerance = 10^{-6}". With these settings, good convergence behavior is observed. Convergence curves of the considered problem are presented later in this chapter, in Section 5.3.3.

Matlab allows the use of parallel computing. Since the system size for one iteration is rather small and does not require large RAM, the parallelization of GA is possible even with a standard desktop computer. Needless to say, this brings a big advantage for the considered problem.

5.3.2 The use of ML-WBM with genetic algorithm

The use of ML-WBM is very advantageous for the considered optimization problem. Especially when using symmetric boundary conditions. The main advantage is that the system of equations for the full model has to be built only once. For each iteration, vacancies are being created in the full grid. These iterations can be modeled by selecting a subset of the full model. This is possible because the coupling matrix of any two scatterers is free of the terms that come from the other scatterers. Consequently, if a scatterer is removed from the system, removing the row and column vectors that correspond to the wave functions of that scatterer is enough to represent the rest of the system. For a configuration of $2 \times n_s$ scatterers in a 2D problem with symmetric boundary conditions (or $4 \times n_s$ scatterers in a 3D problem with symmetric boundary conditions), the system of equations looks as follows:

$$
\begin{bmatrix}
\boldsymbol{A}_1^{(B)} & \emptyset & \cdots & \emptyset & \boldsymbol{C}_{1,1}^{(B,U)} & \boldsymbol{C}_{1,i}^{(B,U)} & \cdots & \boldsymbol{C}_{1,n_s}^{(B,U)} \\
\emptyset & \boldsymbol{A}_i^{(B)} & & \emptyset & \boldsymbol{C}_{i,1}^{(B,U)} & & & \\
\vdots & & \ddots & \vdots & \vdots & & \ddots & \vdots \\
\emptyset & & \cdots & \boldsymbol{A}_{n_s}^{(B)} & \boldsymbol{C}_{n_s,1}^{(B,U)} & & \cdots & \boldsymbol{C}_{n_s,n_s}^{(B,U)} \\
\boldsymbol{C}_{1,1}^{(U,B)} & \emptyset & \cdots & \emptyset & \boldsymbol{A}_1^{(U)} & \boldsymbol{C}_{1,i}^{(U,U)} & \cdots & \boldsymbol{C}_{1,n_s}^{(U,U)} \\
\emptyset & \boldsymbol{C}_{i,i}^{(U,B)} & & \emptyset & \boldsymbol{C}_{i,1}^{(U,U)} & \boldsymbol{A}_i^{(U)} & & \\
\vdots & & \ddots & \vdots & \vdots & & \ddots & \vdots \\
\emptyset & & \cdots & \boldsymbol{C}_{n_s,n_s}^{(U,B)} & \boldsymbol{C}_{n_s,1}^{(U,U)} & & \cdots & \boldsymbol{A}_{n_s}^{(U)}
\end{bmatrix}
\begin{bmatrix}
\boldsymbol{t}^{(1)} \\
\boldsymbol{t}^{(i)} \\
\vdots \\
\boldsymbol{t}^{(n_s)} \\
\boldsymbol{t}^{(+,1)} \\
\boldsymbol{t}^{(+,i)} \\
\vdots \\
\boldsymbol{t}^{(+,n_s)}
\end{bmatrix}
=
\begin{bmatrix}
\boldsymbol{F}^{(1)} \\
\boldsymbol{F}^{(i)} \\
\vdots \\
\boldsymbol{F}^{(n_s)} \\
\boldsymbol{F}^{(+,1)} \\
\boldsymbol{F}^{(+,i)} \\
\vdots \\
\boldsymbol{F}^{(+,n_s)}
\end{bmatrix},
\tag{5.3}
$$

where $\boldsymbol{A}_i^{(B)}$ represents the matrix for the bounded domain of the i^{th} scatterer and $\boldsymbol{A}_i^{(U)}$ represents the matrix for the unbounded one. These terms are written in local coordinates and stay the same irrespective of existence of other scatterers. The coupling matrices between the bounded and unbounded domains are given by $\boldsymbol{C}_{\bullet,\bullet}^{(B,U)}$ and $\boldsymbol{C}_{\bullet,\bullet}^{(U,B)}$, where the former represents the contribution from unbounded to bounded domains and the latter represents the contribution from bounded to unbounded. The coupling matrices between two

unbounded domains are given by $\boldsymbol{C}_{\bullet,\bullet}^{(U,U)}$. Finally, $\boldsymbol{F}^{(\bullet)}$ represent the excitation terms resulting from acoustic sources or boundary conditions.

As long as the dimensions and positions of the scatterers stay the same, the coupling matrices stay the same as well. Consequently, if a scatterer is removed from the system, the other terms are not affected. If the system given above is needed to be reduced to two scatterers, the system matrix looks as follows without recalculation of the terms :

$$\begin{bmatrix} \boldsymbol{A}_1^{(B)} & \emptyset & \boldsymbol{C}_{1,1}^{(B,U)} & \boldsymbol{C}_{1,2}^{(B,U)} \\ \emptyset & \boldsymbol{A}_2^{(B)} & \boldsymbol{C}_{2,1}^{(B,U)} & \boldsymbol{C}_{2,2}^{(B,U)} \\ \boldsymbol{C}_{1,1}^{(U,B)} & \emptyset & \boldsymbol{A}_1^{(U)} & \boldsymbol{C}_{1,2}^{(U,U)} \\ \emptyset & \boldsymbol{C}_{2,2}^{(U,B)} & \boldsymbol{C}_{2,1}^{(U,U)} & \boldsymbol{A}_2^{(U)} \end{bmatrix} \begin{bmatrix} \boldsymbol{t}^{(1)} \\ \boldsymbol{t}^{(2)} \\ \boldsymbol{t}^{(+,1)} \\ \boldsymbol{t}^{(+,2)} \end{bmatrix} = \begin{bmatrix} \boldsymbol{F}^{(1)} \\ \boldsymbol{F}^{(2)} \\ \boldsymbol{F}^{(+,1)} \\ \boldsymbol{F}^{(+,2)} \end{bmatrix}. \tag{5.4}$$

By examining the structure of the ML-WBM system matrices, one can see that the matrix is not fully populated. The upper left part, which consists of matrices of bounded subdomains, $\boldsymbol{A}_{\bullet}^{(B)}$, and the lower left part which comprises coupling matrices $\boldsymbol{C}_{\bullet,\bullet}^{(U,B)}$ have a sparse structure. It is possible to take advantage of this property by exploiting the efficiency of sparse matrix solvers. It should be noted that, such an advantage would work in special cases, where the sparsity is pronounced. For the problem at hand, this is the case since a large number of scatterers is considered. It should also be noted that, only one of the sparse sub-matrices can take advantage of sparse solvers. For the considered problem, the number of bounded wave functions is higher than the unbounded ones, therefore the upper left part of the matrix is chosen to be used with a sparse solver. A three step procedure is used for this purpose, which is detailed in [135]. Here, only a brief explanation is given. The main idea is to write the unknowns of bounded subdomains as a function of the unknowns of unbounded subdomains and rearrange the system such that a sparse solver can be used to calculate the relations. Subsequently, a dense solver is used to find unknowns of the unbounded domains. The unknowns for bounded domains are calculated with a matrix multiplication. The advantage of such a procedure is that it reduces the total number of CPU operations. For the considered case, it especially brings an advantage when it is used in conjunction with parallel computing. As such, each single CPU is able to solve the system of equations easier when compared to solving the whole system with a dense solver.

5.3.3 Optimization of 2D acoustic lenses

The full grid model that acts as a template for the acoustic lens designs in this subsection consists of 80 scatterers, on a square lattice of 5 columns and 16 rows as shown in Figure 5.9. The scatterers are distributed symmetrically, where 40 (5 columns and 8 rows) of them are above the x axis and 40 of them are below. All the acoustic lenses use lattice parameter of 0.05 m. Two types of lenses are considered; the ones based on cylinders and the ones based on

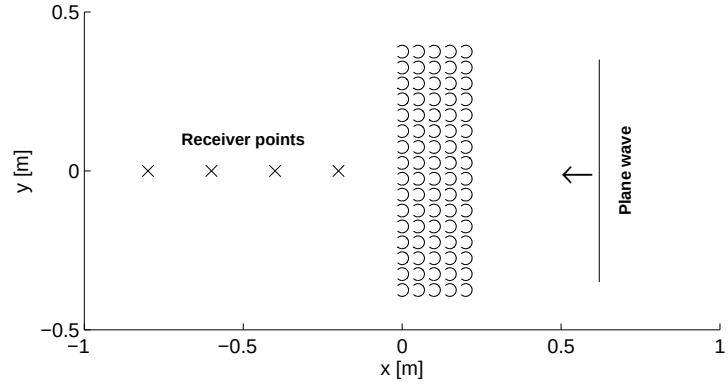

Figure 5.9: The geometry of the full grid for the acoustic lens made up of Helmholtz resonators with a plane wave excitation and the position of receiver points. The same setting is used for lenses made up of cylinders.

Helmholtz resonators. For acoustic lenses based on cylinders, the radius of one scatterer is 0.02 m. For the lenses based on Helmholtz resonators, the opening of a scatterer is 90°, while the radius is again 0.02 m. The dimensions are chosen similar to the values in literature [21, 61, 66]. The thickness of the walls of Helmholtz resonators are assumed to be zero. Rigid boundary conditions are used for all the examples, i.e. $\overline{v}_n = 0$ m/s. For all the simulations, air with properties of 340 m/s for speed of sound and 1.225 kg/m^3 for the fluid density is used.

The optimization calculations are run for three different frequencies, where the Helmholtz resonator based acoustic lenses are compared with cylinder based acoustic lenses. The three different frequencies are chosen as 2300 Hz, 1500 Hz and 1000 Hz, in order to make a comparison over a wide frequency range. In addition, these frequencies represent three different wave propagation characteristics for the SCs when they are in their full grid configurations. At 2300 Hz, both of the SCs exhibit a stop band. At 1500 Hz, cylinder based SCs exhibit refractive properties and Helmholtz resonator based ones exhibit again a stop band. Finally, at 1000 Hz, both of them have refractive characteristics (See Figure 5.2 for band structure figures, calculated by using Bloch-Floquet periodic boundary conditions on a unit cell). For each frequency, the optimization calculations are run for four different focusing points to show the responsiveness of the design procedure. The points are chosen as 0.2 m, 0.4 m, 0.6 m and 0.8 m away from the acoustic lenses. The figures are organized in a tabular format to visualize the moving focal points in the column vector and compare the Helmholtz based and cylinder based lenses side by side. The inset texts for each contour plot shows the normalized SPL at the desired focusing point in dB, which is defined in equation (5.1).

The model details for the three frequencies are given in table 5.1 for the full

grid models. A truncation factor of $T = 50$ is used for all simulations. The accuracy of the optimized topologies are checked against an Indirect Variational Boundary Element Method model. The reference models are valid up to 30 kHz by using the 10 linear elements per wavelength rule. For all the ML-WBM models, the absolute values of the relative pressure error at the focusing points are below 1 %, given by equation (5.2).

	1000 Hz	1500 Hz	2300 Hz
Helmholtz res. based SCs : # of Unbounded WFs	1560	2280	3480
Helmholtz res. based SCs : # of Bounded WFs	2720	4000	6080
Cylinder based SCs : # of Unbounded WFs	280	440	600

Table 5.1: Model information for the full grid models

One should be careful about giving specific details on calculation times for the optimization process. The main reason is that, the number of scatterers changes for different chromosomes. Although the chromosomes eventually become very similar for a generation, early generations have a varying composition that affects the calculation time, i.e. one chromosome might be composed of a couple of scatterers, while another can be the full model. Averaging the calculation times can be misleading as well, because depending on the focusing point, the majority of the generation can comprise dense or sparse populations. Therefore, the calculation times given here are case dependent and only given to provide a general sense for the size of the problem. All the simulations are run on a Windows server machine with 8 Intel Xeon X5650, 2.67 GHz Cpus and 32 GB RAM. By using 8 parallel Matlab workers, the average computation time for one iteration at 1000 Hz yields 0.96 seconds for the Helmholtz resonator based SCs. The same parameter for 2300 Hz is 2.16 seconds. When it comes to the cylinder based SCs, the model sizes are considerably smaller and the average computation times are 0.003 seconds and 0.009 for 1000 Hz and 2300 Hz, respectively.

Figure 5.10 shows the results for 2300 Hz. At this frequency, both SCs experience a stop band in their full grid configurations. The minor difference is that, the cylinder based SCs experience a directional stop band while the Helmholtz resonator based SCs have a full stop band. As both of them behave similarly, the difference is expected to be minor. When the results are examined, this seems to be the case. Only for the 0.2 m point, the Helmholtz resonator based SC has a more pronounced advantage. However, this advantage is not repeated for other focusing points. Therefore, having stop band characteristics for both SCs gives similar results, irrespective of the type of the stop band, i.e. a directional or a full stop band. On a side note, one can see that the resulting topologies have rather sparse populations, which confirms that the SCs in their dense forms have stop bands. As such, the focusing mechanisms seem more related to diffraction and multiple scattering. A very clear example of this can be seen for the case of 0.8 m with cylinder based SC.

Figure 5.11 shows the results for 1500 Hz. For all focal points, the Helmholtz

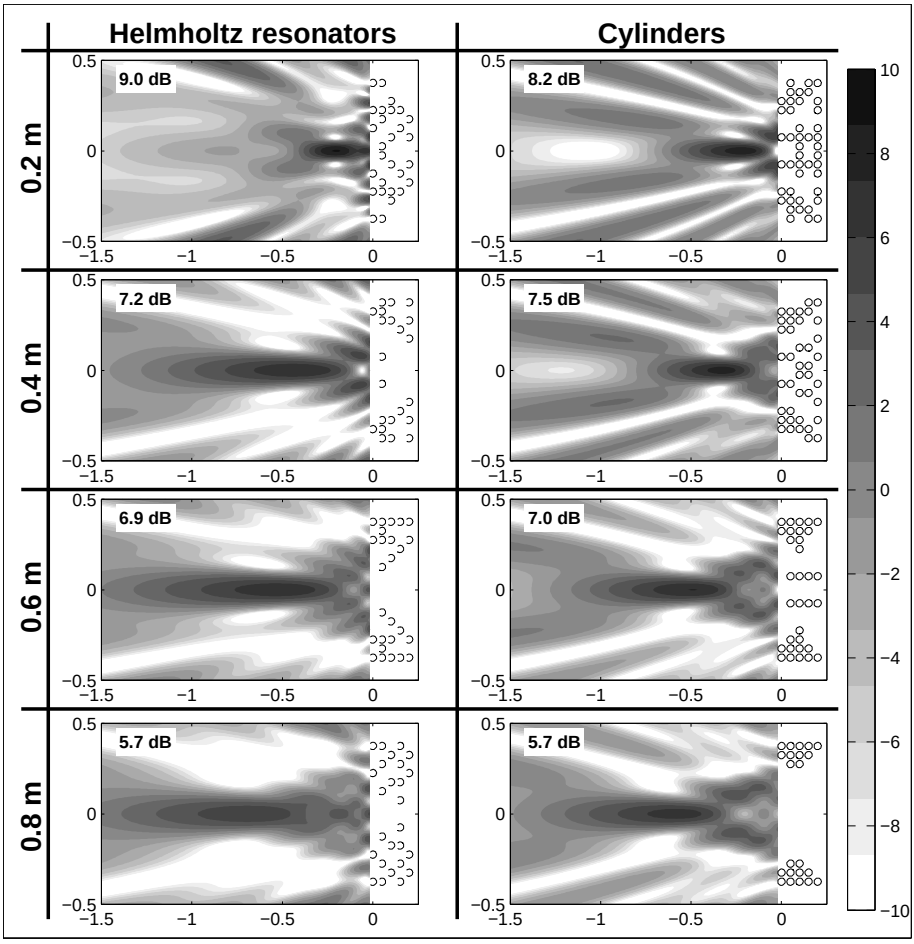

Figure 5.10: The results of the optimization at 2300 Hz for Helmholtz resonator based and cylinder based acoustic lenses. The gray scale bar is given in dB. The x and y axes of the subfigures are given in m. The inset text shows the normalized SPL for the corresponding focusing point.

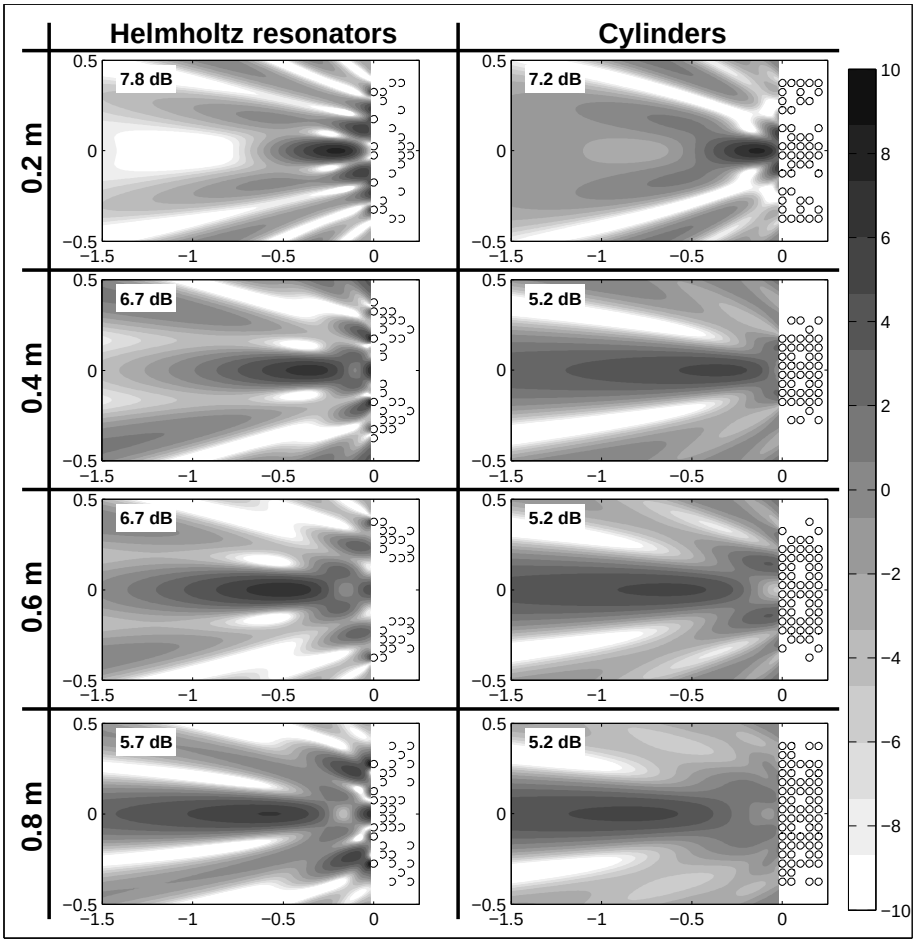

Figure 5.11: The results of the optimization at 1500 Hz for Helmholtz resonator based and cylinder based acoustic lenses. The gray scale bar is given in dB. The x and y axes of the subfigures are given in m. The inset text shows the normalized SPL for the corresponding focusing point.

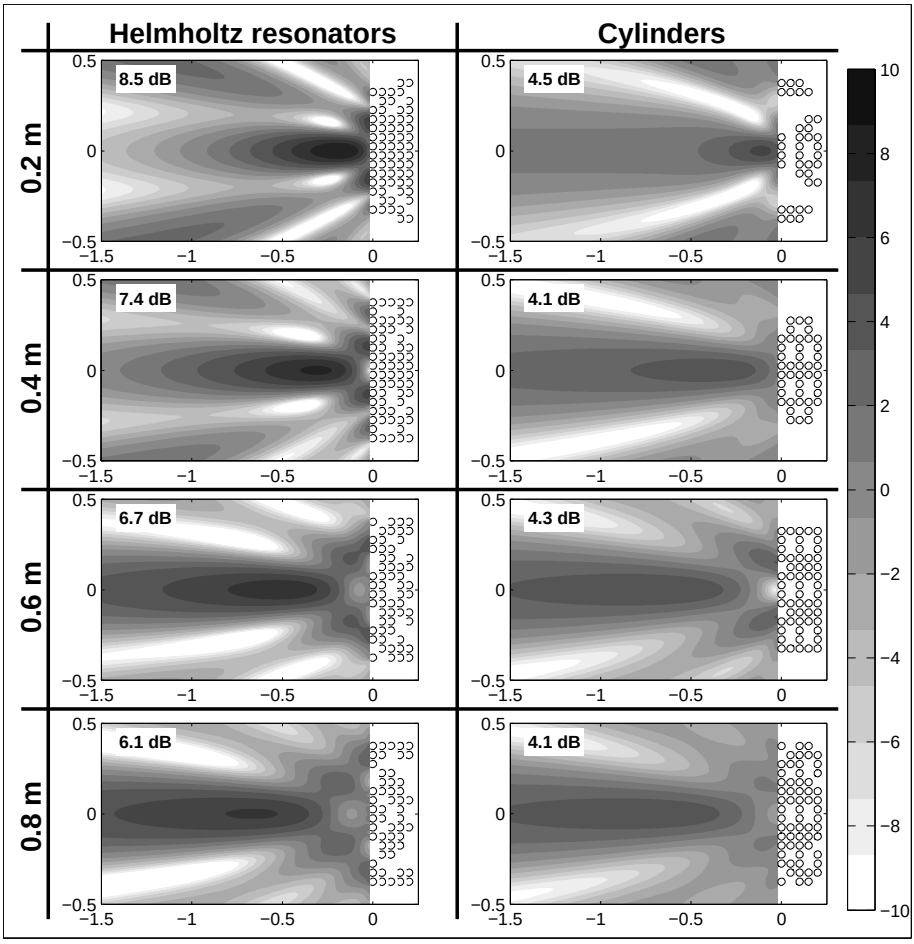

Figure 5.12: The results of the optimization at 1000 Hz for Helmholtz resonator based and cylinder based acoustic lenses. The gray scale bar is given in dB. The x and y axes of the subfigures are given in m. The inset text shows the normalized SPL for the corresponding focusing point.

based lenses perform better than the cylinder based ones. The maximum difference between the two lenses is 1.5 dB, while the minimum difference is 0.5 dB. By looking at the resulting topologies, one can see that this is indeed a frequency where the wave propagation characteristics are different for the two lenses. For the cylinder based lenses, the topologies are shaped more densely, so that the wave travels within the SC and are refracted to focus sound at the given position. On the other hand, the Helmholtz resonator based lenses have less dense topologies, as such they mainly take advantage of multiple scattering. This can be observed especially for the 0.4 m and 0.6 m cases. Nevertheless, the better performance of Helmholtz based lenses is apparent for all the positions.

Finally, Figure 5.12 shows the results for 1000 Hz, where both SCs experience refractive characteristics. The Helmholtz based lenses once again perform better than the cylinder based ones. That being stated, this time the difference is more pronounced. It can be as high as 4.0 dB, while the minimum difference is 2.0 dB. By looking at the resulting dense topologies, it is possible to see that both lenses are mainly using the refraction mechanisms to focus the sound. However, the Helmholtz based lenses are more efficient because of their high refraction index at this frequency. This difference emphasizes the biggest advantage of the Helmholtz resonator based lenses. By using the local resonances, efficient acoustic lenses can be designed in low frequencies without occupying large spaces. This is not possible with a cylinder based lens. The refraction mechanism for cylinder based lenses is best experienced just before the Bragg scattering related stop band. As such, the lattice parameter and the acoustic lens size should be large to create a stop band in low frequencies, where half wavelength should fit the lattice parameter size.

It should be noted that the dissipation is not taken into account for the presented simulations. In the numerical experiment presented by Hu *et al.* [72], Helmholtz resonators with aperture of 36°and radius of 1.36 cm are considered and the absorption is predicted as 0.17% at its peak at around 1300 Hz. For larger apertures, e.g. the presented ones with 90°, the effect of viscious losses is less pronounced. Hence, it is considered negligable for the presented cases.

In order to show the convergence behavior of the presented problem, two typical convergence curves are given in Figure 5.13. They correspond to the simulations presented in Figure 5.12 at 0.2 m and demonstrate the efficiency and convergence of GA.

To sum up, for almost all cases, the Helmholtz based resonators perform better than the cylinder based ones. This was expected and can be explained by the use of their higher refraction index or the use of strong local resonances for stop bands. Therefore, their advantages over cylinder based SCs for the acoustic lens designs are demonstrated.

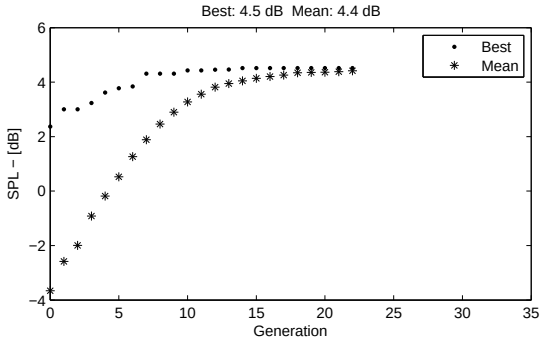

(a) Unit scatterer: cylinder

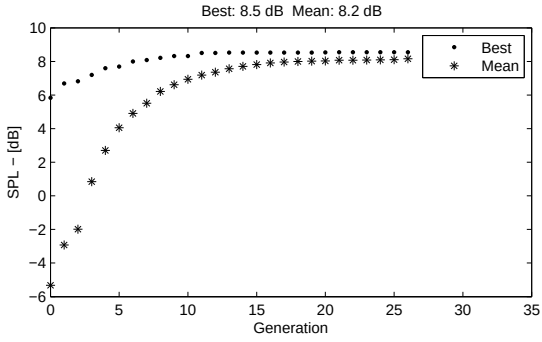

(b) Unit scatterer: Helmholtz resonator

Figure 5.13: The evolution of the normalized SPL for cylinder and Helmholtz resonator based acoustic lenses at 1000 Hz with 0.2 m focal point. One generation consists of 500 chromosomes. "Best" refers to the highest sound amplification value given by the best chromosome and "Mean" refers to the average SPL of all the chromosomes of the generation.

5.3.4 Optimization of 3D acoustic lenses

Two different sets of lenses are presented in this subsection. The first set is based on spherical scatterers. In order to use acoustic local resonances and create compact lenses, a second set is presented based on cup shaped scatterers. For all the calculations, air with properties, $c = 340$ m/s and $\rho_0 = 1.225$ kg/m^3, is used as the fluid. The scatterers are rigid for all the cases, i.e. $\bar{v}_n = 0$ m/s. The normalized sound pressure level(SPL) value used to evaluate the performance of the lenses is again calculated by equation (5.1). The excitation to the system is a plane wave propagating from the positive x axis to the negative x axis with an amplitude of 1 Pa. All the design simulations are run on a Windows server machine with 12 Intel Xeon X5650, 2.67 GHz Cpus and 64 GB RAM.

Lenses based on spheres

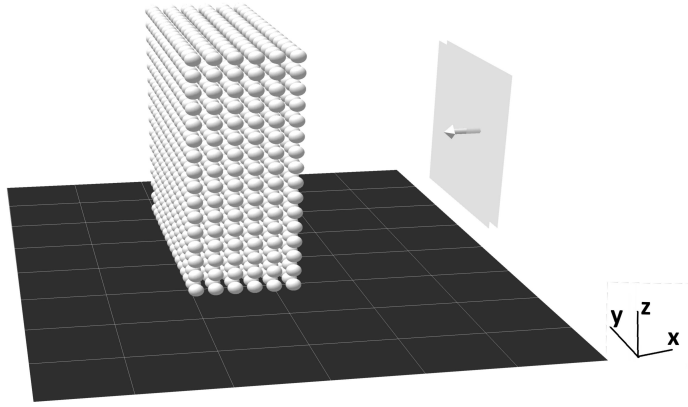

Figure 5.14: The geometry of the full grid for the acoustic lens made of spheres with a plane wave excitation (The SC is in free space and the ground sketch is only included for the ease of visualization).

The first set of acoustic lens designs are based on rigid spheres. The full grid model, which can be seen in Figure 5.14, consists of 1536 spheres. They are distributed symmetrically on a grid of $6 \times 16 \times 16$ in x, y and z axes, respectively. In that, the unit cell has a primitive cubic (also referred as simple cubic) system distribution. The radius and lattice parameter are chosen similar to the previous sections as 0.02 m and 0.05 m, respectively. Symmetric boundary conditions are used on the y and z axes. This reduces the number of scatterers that are numerically modeled to one-fourth of the full model, including 384 scatterers.

The lenses are designed for two different frequencies and two different focal points for each frequency, to demonstrate the responsiveness of the designs. The working frequencies are chosen as 2200 Hz and 2500 Hz, with focal points of 0.5 m and 0.75 m. Both frequencies are below the first Bragg scattering gap, where the SC exhibit slower speed of sound as compared to air.

For both frequencies, the truncation parameter T as defined in equation (2.23) is set to 1. This makes the maximum degree, $l_{max} = 2$ and the number of wave functions per scatterer, 9. As such, the full grid symmetric model has 3456 unknowns. The accuracy of the models are verified against a finer ML-WBM model, with $l_{max} = 4$ and number of wave functions per scatterer, 25. For all the ML-WBM models, the absolute values of the relative pressure error at the focusing points are below 1 %, given by equation (5.2).

The results for the acoustic lens designs are given in Figures 5.15-5.22. The topologies are presented first, followed by the pressure fields given by equation (5.1). In the topology figures, each subfigure shows the topology of a layer of the lenses in y-z plane, with the x coordinates given in the captions. As

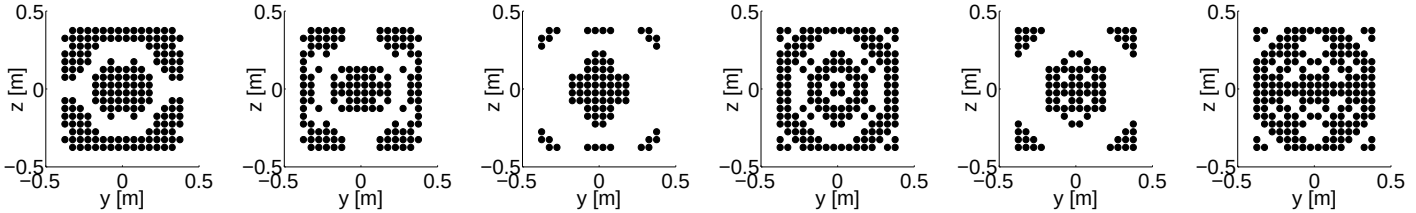

(a) x = -0.25 m (b) x = -0.20 m (c) x = -0.15 m (d) x = -0.10 m (e) x = -0.05 m (f) x = 0 m

Figure 5.15: The design results showing the topology of the lens optimized for 2200 Hz and 0.75 m. Each subfigure corresponds to one layer of the lens at the given x coordinate.

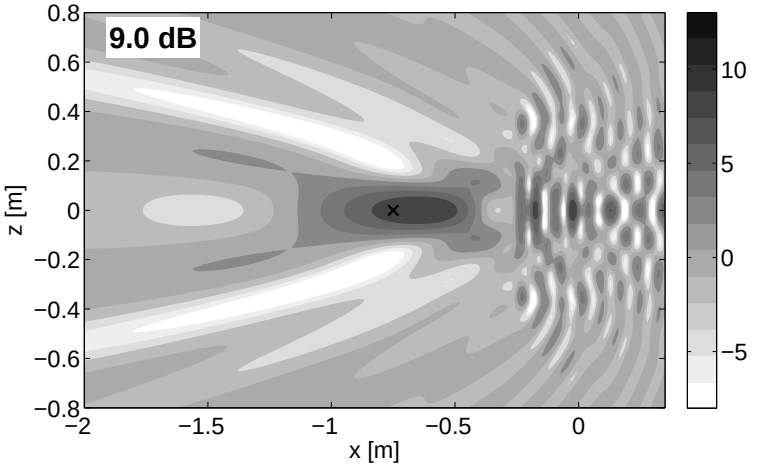

Figure 5.16: The acoustic pressure field given in normalized SPL value - [dB]. The field is generated by the lens optimized for 2200 Hz and 0.75 m. The x marker shows the location of the focal point.

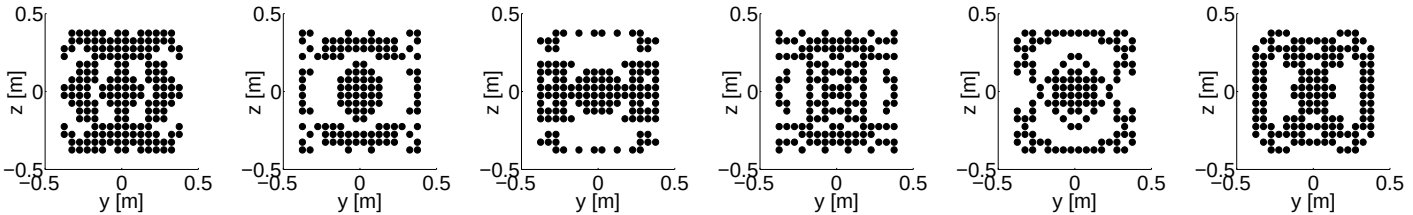

(a) x = -0.25 m (b) x = -0.20 m (c) x = -0.15 m (d) x = -0.10 m (e) x = -0.05 m (f) x = 0 m

Figure 5.17: The design results showing the topology of the lens optimized for 2200 Hz and 0.5 m. Each subfigure corresponds to one layer of the lens at the given x coordinate.

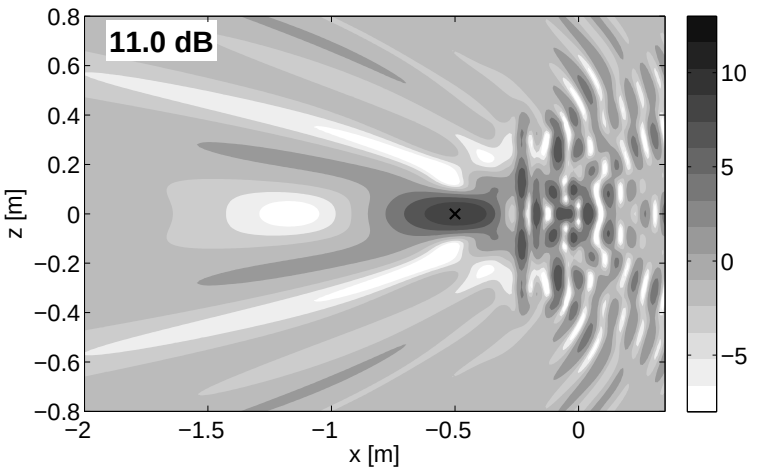

Figure 5.18: The acoustic pressure field given in normalized SPL value - [dB]. The field is generated by the lens optimized for 2200 Hz and 0.5 m. The x marker shows the location of the focal point.

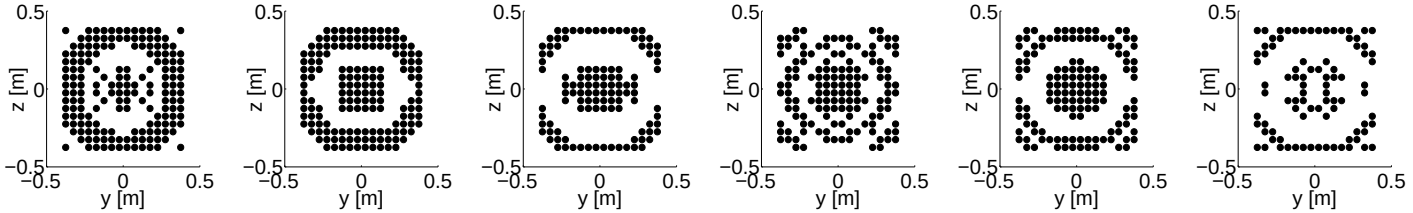

(a) x = -0.25 m (b) x = -0.20 m (c) x = -0.15 m (d) x = -0.10 m (e) x = -0.05 m (f) x = 0 m

Figure 5.19: The design results showing the topology of the lens optimized for 2500 Hz and 0.75 m. Each subfigure corresponds to one layer of the lens at the given x coordinate.

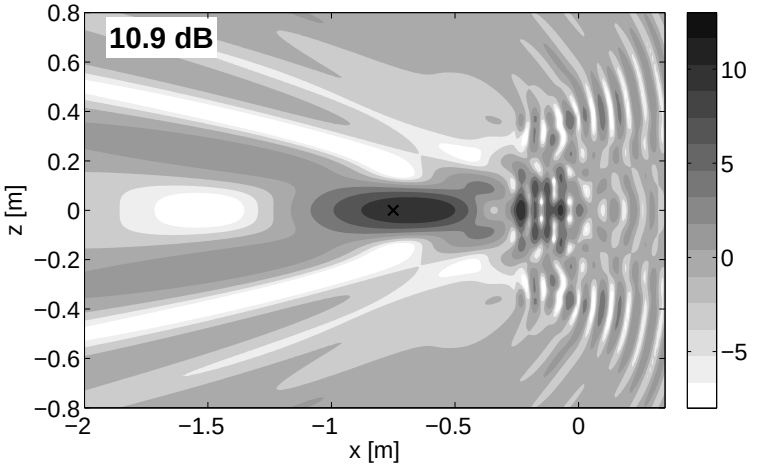

Figure 5.20: The acoustic pressure field given in normalized SPL value - [dB]. The field is generated by the lens optimized for 2500 Hz and 0.75 m. The x marker shows the location of the focal point.

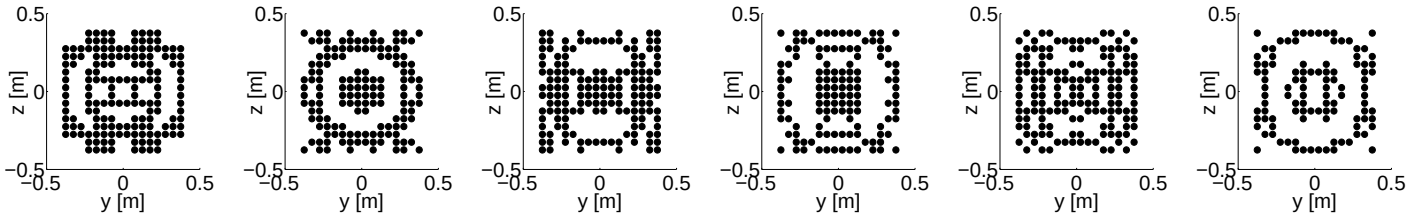

(a) x = -0.25 m (b) x = -0.20 m (c) x = -0.15 m (d) x = -0.10 m (e) x = -0.05 m (f) x = 0 m

Figure 5.21: The design results showing the topology of the lens optimized for 2500 Hz and 0.5 m. Each subfigure corresponds to one layer of the lens at the given x coordinate.

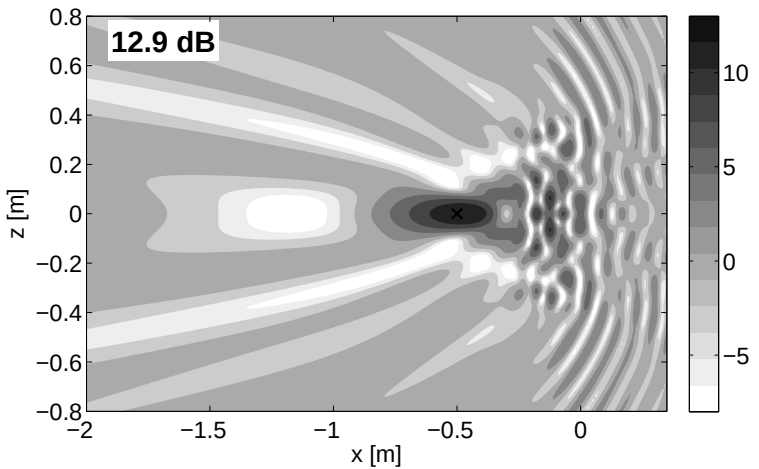

Figure 5.22: The acoustic pressure field given in normalized SPL value - [dB]. The field is generated by the lens optimized for 2500 Hz and 0.5 m. The x marker shows the location of the focal point.

such, the plane wave is hitting the layer on the right ones first and propagate through each one to create the lens effect. The normalized SPL values at the focal points are given as inset text on the pressure field figures.

The sound amplification at the focal points varies between 9 dB to 12.9 dB for the given cases. One can clearly observe how well the focal points move for different cases and how they follow the given objective points.

The complex nature of the topologies shows that the focusing does not occur as a result of a pure refraction mechanism. One can see that the sound waves are bent by passing through narrow and wide passages. As such, the waves are scattered and collide with each other. It is a complex mechanism because parts of the SC can refract the waves and parts of it can diffract and scatter. The advantage of using the inverse design through GA is that no matter how complex the scattering within the SC is, the algorithm always choose the better configurations. As such, the incoming wave is collected at the given focal point.

The average computation time for one iteration for the given designs is 0.68 seconds, by using 12 parallel Matlab jobs. One should be careful about how to interpret this value, as it is with the previous section. This value is case dependent and is affected by how crowded the generations are. On the other hand, it is averaged for the four cases presented and can be a good indicator to give a sense of the efficiency of the ML-WBM. Considering that the presented acoustic lenses are large systems with a high number of scatterers, being able to solve it with only 3456 unknowns for the full system and with the given computational time shows once again how much the ML-WBM fits to a lens design procedure. To give a sense of the problem size, it is also of interest to detail the number of iterations per case. The average number of iterations per design case is 127500 for the presented designs.

Lenses based on cup shaped scatterers

While it is possible to gain powerful focusing effect with the rigid spheres, they only act as scattering objects. On the other hand, it has been demonstrated with 2D examples that using the local resonances of the scatterers leads to better designs. As such, using cup shaped scatterers is proposed in this section. The geometry of the full grid of scatterers can be seen in Figure 5.23. The scatterers, which are referred to as cup shaped scatterers, are created from half spherical shells. The inside of each shell is empty such that it forms a cavity. The thickness of the walls is neglected for the numerical models. The radius of the half spheres and the lattice parameter are kept the same as in the previous examples, i.e. 0.02 m and 0.05 m, respectively. The number of scatterers is reduced to 320, in order to create compact lenses. They are symmetrically distributed on a $5 \times 8 \times 8$ grid. In addition, the distribution of the scatterers in a unit cell is using a primitive cubic system as before.

The reason that the cup shaped scatterers are chosen is because of their simplicity. While, from a manufacturing point of view, they are easy to produce,

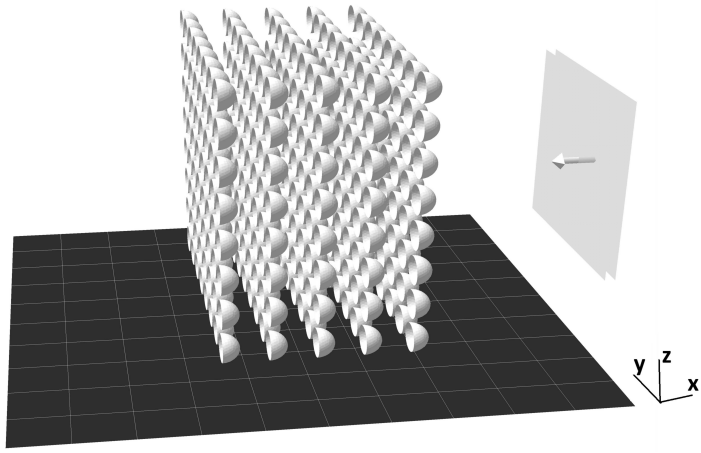

Figure 5.23: The geometry of the full grid for the acoustic lens made of cup shaped scatterers with a plane wave excitation (the SC is in free-space and the ground sketch is only included for the ease of visualization).

they still have local resonances that change the wave propagation properties within SCs.

The same working frequencies (2200 Hz and 2500 Hz) and focal points (0.5 m and 0.75 m) as in the previous case are chosen, in order to make a valid comparison. For both frequencies, the truncation parameter T is set to 3 for the ML-WBM model. This leads to 84 bounded wave functions and 25 unbounded wave functions for each scatterer. As such, the total number of unknowns is 8720 for a full grid model, by using the y and z axes symmetries. The accuracy of the model is compared to a Fast-Multipole BEM model. The full grid model of the FM-BEM has 141440 elements and 76160 nodes. It uses linear triangular elements and is valid up to 6.6 kHz, according to the 10 elements per wavelength rule. For all the ML-WBM models, the absolute values of the relative pressure error at the focusing points are around 1 %, given by equation (5.2).

The results for the acoustic lens designs are given in Figures 5.24-5.31. As it is with the previous subsection, the topologies are presented first, followed by the pressure fields given by equation (5.1). The average computation time for one iteration for the given designs is 2.29 seconds and the average number of iterations per design case is 17000. These are averaged values over the four cases presented in this section. As indicated before, the values are case dependent and are given to provide a sense of the problem size.

The sound amplification at the focal points varies between 9.2 dB and 10.9 dB. For the 2200 Hz case, the difference between using spheres and cups is negligible. This is remarkable, considering that the size of the acoustic lens is reduced considerably. The acoustic lenses based on cups occupy half the space in y and z axes and one layer less in x axis. As such, the size is almost 1/4 of

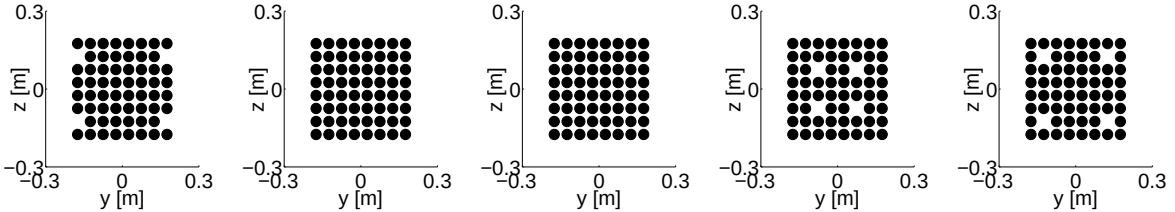

(a) x = -0.20 m (b) x = -0.15 m (c) x = -0.10 m (d) x = -0.05 m (e) x = 0 m

Figure 5.24: The design results showing the topology of the lens optimized for 2200 Hz and 0.75 m. Each subfigure corresponds to one layer of the lens at the given x coordinate.

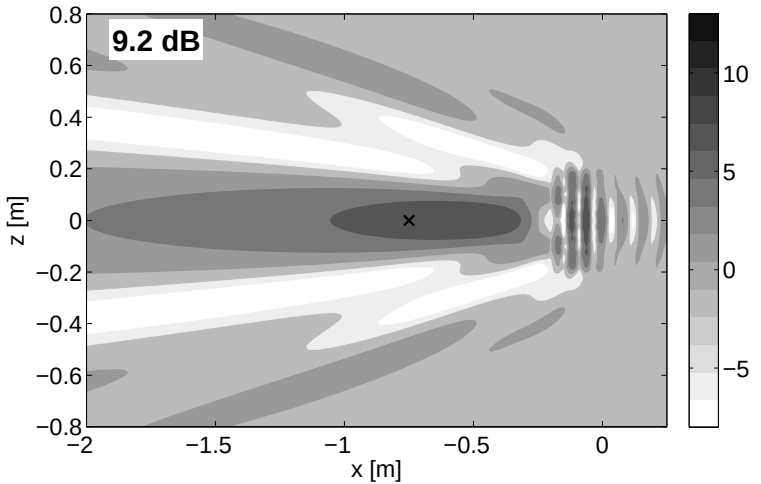

Figure 5.25: The acoustic pressure field given in normalized SPL value - [dB]. The field is generated by the lens optimized for 2200 Hz and 0.75 m. The x marker shows the location of the focal point.

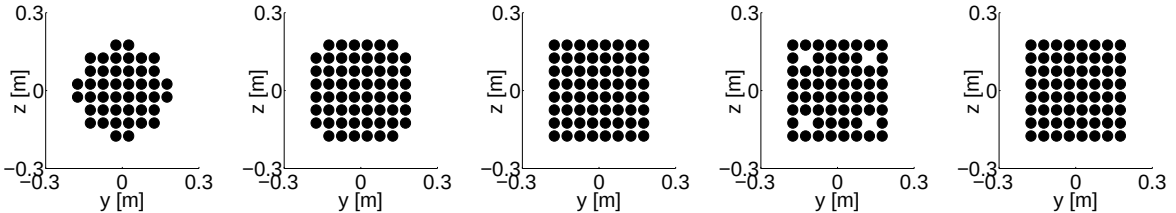

(a) x = -0.20 m (b) x = -0.15 m (c) x = -0.10 m (d) x = -0.05 m (e) x = 0 m

Figure 5.26: The design results showing the topology of the lens optimized for 2200 Hz and 0.5 m. Each subfigure corresponds to one layer of the lens at the given x coordinate.

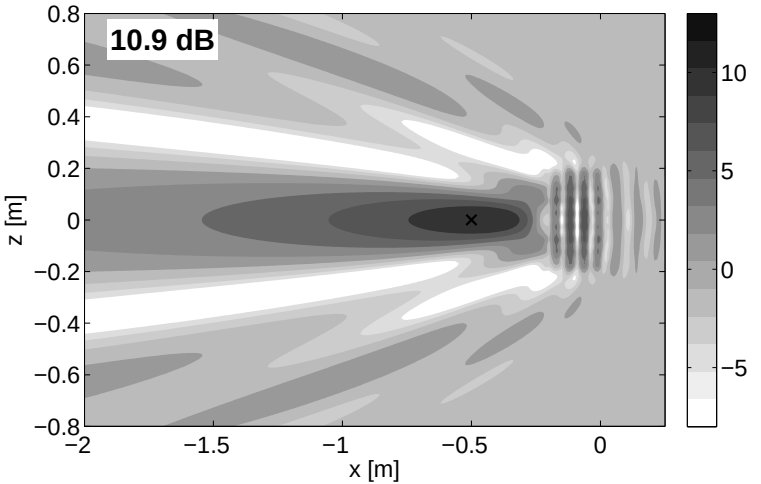

Figure 5.27: The acoustic pressure field given in normalized SPL value - [dB]. The field is generated by the lens optimized for 2200 Hz and 0.5 m. The x marker shows the location of the focal point.

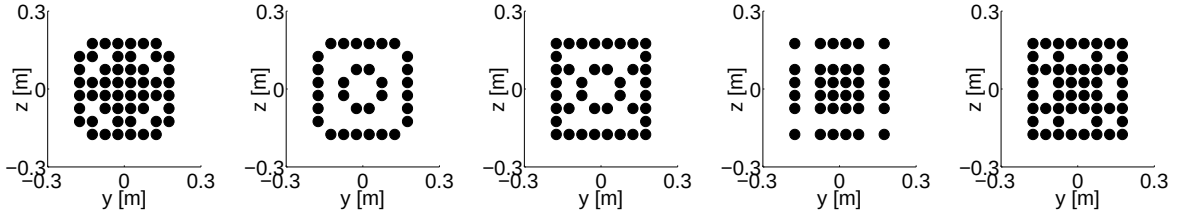

(a) x = -0.20 m (b) x = -0.15 m (c) x = -0.10 m (d) x = -0.05 m (e) x = 0 m

Figure 5.28: The design results showing the topology of the lens optimized for 2500 Hz and 0.75 m. Each subfigure corresponds to one layer of the lens at the given x coordinate.

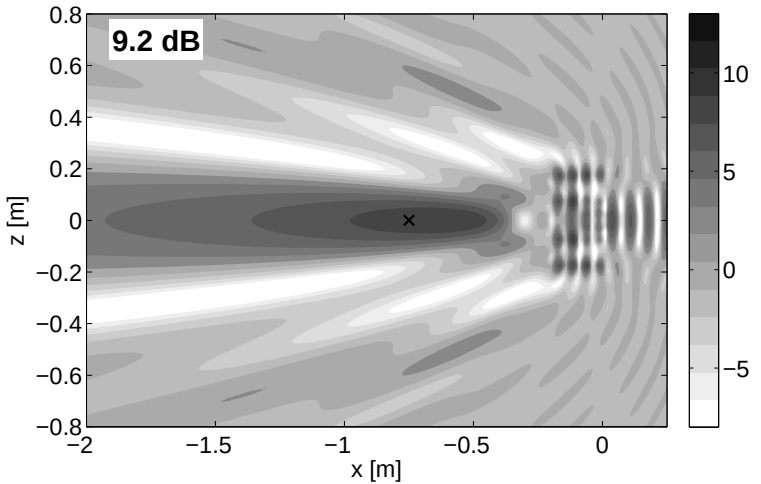

Figure 5.29: The acoustic pressure field given in normalized SPL value - [dB]. The field is generated by the lens optimized for 2500 Hz and 0.75 m. The x marker shows the location of the focal point.

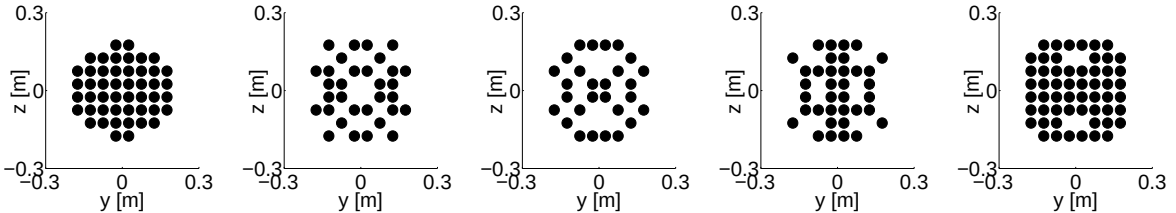

(a) x = -0.20 m (b) x = -0.15 m (c) x = -0.10 m (d) x = -0.05 m (e) x = 0 m

Figure 5.30: The design results showing the topology of the lens optimized for 2500 Hz and 0.5 m. Each subfigure corresponds to one layer of the lens at the given x coordinate.

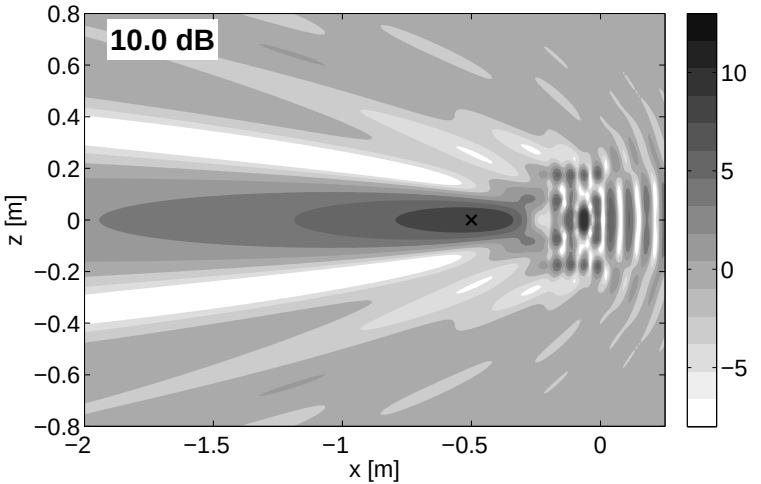

Figure 5.31: The acoustic pressure field given in normalized SPL value - [dB]. The field is generated by the lens optimized for 2500 Hz and 0.5 m. The x marker shows the location of the focal point.

the previous one.

When it comes to the 2500 Hz case, the differences become noticeable. For the 0.5 m focal point, the difference is 2.9 dB. This shows that, having local resonances do not always guarantee a better focusing effect, such that they should be tuned for the right frequency. Still, if one has space constraints, a smaller lens can be preferred with a small compensation on the focusing effect.

An alternative way of comparing the two lenses is by equalizing their sizes. In order to do so, lenses based on spherical scatterers are designed, starting from a full grid of 320 scatterers (see Appendix A). At 2200 Hz and 0.5 m, the lens based on spheres provides sound amplification of 6.7 dB, which is 4.2 dB lower than the lens based on cup shapes. At 2500 Hz and 0.5m, the lens based on spheres provides sound amplification of 4.5 dB, which is 5.5 dB lower than the lens based on cup shapes. Having such differences between two lenses shows once more the efficiency of using local resonances in acoustic lens designs.

It is of interest to compare the presented lenses with the ones in literature. Sanchis *et al.* [114] presented 3D acoustic lenses with axial symmetry. The lens that was physically feasible to be constructed was tuned for 0.5 m at the working frequency of 2200 Hz. They predicted theoretically the normalized SPL as 13.25 dB. For the presented compact lens, it is 10.9 dB for the same focal point and frequency. While the difference is noticeable, one should decide on the type of lens to use by considering practicalities. The lens presented in [114], has 1.165 m diameter, while the lens with the cup shapes has 0.39 m width and height. As such, the lenses presented here become alternatives to the ones in literature as compact lenses.

5.4 Conclusion

The ML-WBM is applied to acoustic lens designs in this chapter. Being the efficient tool as it is, the ML-WBM opens doors to explore innovative acoustic lens designs.

Firstly, a new acoustic lens design procedure is presented, which utilizes the degree of openness/closedness of the unit scatterer shape as the design variable, together with the lattice parameters in x and y directions. Through nine different cases, which consist of three different frequencies and three different focal lengths, the effectiveness of the procedure is demonstrated.

Secondly, the local resonator based SCs are introduced for acoustic lens designs, which use a vacancy optimization procedure. The advantage of using the ML-WBM in this context is demonstrated. It is shown that the system of equations has to be built once for the full grid. For each iteration, a subset of the full matrix is needed without having to calculate new terms. The simulations are run for 2D and 3D problems. It is shown that the 2D Helmholtz based SCs give better focusing effect than the cylinder based ones for almost all the tested cases.

They perform especially well at low frequencies by using their local resonances. This is the case for 3D problems as well. As an alternative to lenses based on rigid spheres, compact lenses that are based on cup shaped scatterers are designed. It is shown that the lenses based on cup shaped scatterers are capable of giving the same focusing power by using their local resonances, while only occupying 1/4 of the space that the spheres occupy.

Chapter 6

Hybrid Boundary Element - Wave Based Method

This chapter presents the coupling of the Wave Based Method and the Boundary Element Method. The motivation for the development of the hybrid method is given first. The superposition principle that is in the heart of the hybrid method is explained by defining the domain decomposition and field variable. The details for building the coupling matrices and the hybrid system are presented. Finally, the modeling principles and the properties of the hybrid method are discussed.

6.1 Motivation

There have been two major extensions to the WBM in the past in order to relax the geometrical requirements of the method, i.e. the ML-WBM and the hybrid FE-WBM.

The ML-WBM is a very useful extension to the WBM due to the fact that it relaxes the geometrical limitations of the method for the inclusion and multiple scattering problems. However, the method loses its efficiency when there is a geometrically complex scatterer or inclusion in the system. Even though it is possible to consider that object in an isolated level, the bounded domain division inside the truncation circle reduces the efficiency or in some cases even makes it unfeasible to apply the ML-WBM, because of the convex subdomain necessity.

The hybrid FE-WBM also brings flexibility to the WBM framework and has been applied on bounded [137] and unbounded problems [11]. The hybrid FE-WBM for bounded problems is aimed for large cavities that have fine geometrical details on the boundaries. The details on the boundaries are

modeled with the FEM submodel and simple-shaped subdomains are created inside to be efficiently modeled with the WBM submodel. However, this approach does not provide an efficient solution when there is an inclusion in the cavity. In such a case, the large subdomains that are modeled with the WBM have to be further divided into small subdomains and the method loses its efficiency. For unbounded problems, the hybrid FE-WBM works similar to Dirichlet-to-Neumann map (DtN) for FEM. The WBM submodel, which uses the unbounded wave function set, surrounds the FEM submodel to simulate the radiation of the waves to infinity. While providing a good alternative to DtN conditions, the necessity to mesh the domain between the outer truncation and the physical boundaries of the geometry causes impracticalities on certain configurations. This is the case for multiple scattering problems, where the scatterers can be well separated.

The ML-WBM and the hybrid FE-WBM indeed brings flexibility to the WBM framework and extends the possible range of applications where the efficiency of the WBM can be exploited. Nevertheless, they fail to efficiently address multiple scattering and inclusion problems when there are complex scatterers or inclusions in the problem.

Considering the limitations and advantages of the hybrid FE-WBM and the ML-WBM, a new hybrid approach to couple the BEM and the WBM is proposed in this chapter. The hybrid Boundary Element - Wave Based Method (BE-WBM) targets two specific problem settings: multiple scattering problems where simple and complex scatterers co-exist and inclusion problems where the cavity has a moderately complex geometry and the inclusions have highly complex geometry. Both problem settings are common and used in various fields. Multiple scattering problems with scatterers of varying complexity are encountered in acoustic imaging and radar applications, in underwater acoustics and urban sound propagation examples. Complex inclusion problems are common in acoustic engineering and room acoustics fields. Loudspeaker cabins with diffusers and rooms with acoustic panels are some examples.

The hybrid BE-WBM embraces the philosophy of combining the best of the two worlds. In other words, the efficiency of the WBM is exploited for moderately complex geometries and the flexibility of the BEM is used for complex geometries. The superposition principle is used to couple the two methods.

It should be noted that, for inclusion problems, the simple inclusions can still be modeled by using the unbounded WBM, following the principles of the ML-WBM. However, the focus here is on extending the ML-WBM framework for geometrically complex inclusions. As such, the WBM submodel for modeling inclusions is omitted for the following formulas to have a better readability.

6.2 Domain decomposition and field variable definition

The first step in deriving the hybrid method is the decomposition of the problem domain. The primary field variable, which is pressure in this case, is defined afterwards; in accordance with the decomposition process.

The domain decomposition and the definition of the main field variable differ for bounded and unbounded problems. As such, they are again presented in different subsections.

In order to have a better readability on the upcoming hybrid BE-WBM formulas, the BEM boundaries are represented with S, while the WBM boundaries are represented with Γ.

6.2.1 Bounded problems

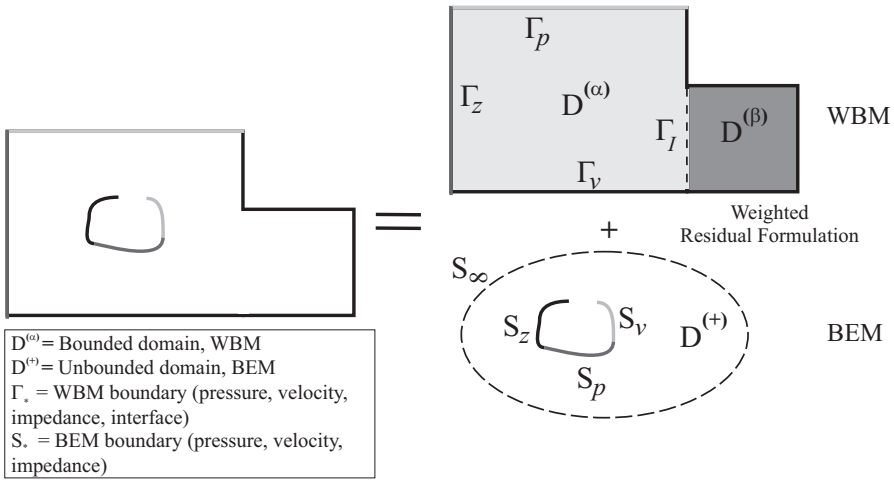

Figure 6.1: Graphical representation of the hybrid modeling concept for bounded problems, together with the definitions of subdomains and boundaries. The term $D^{(\bullet)}$ is used for the domains, $\Gamma_\bullet$ is for the WBM boundaries and interfaces and $S_\bullet$ is for the BEM boundaries.

The concept for the decomposition of the domain into bounded and unbounded domains is illustrated in Figure 6.1. The bounded domain is associated with the WBM and the unbounded domain is associated with the BEM. In order to couple the two domains, one should first examine the decoupled problems on their own. The WBM pressure field is governed by:

$$\nabla^2 p_w^{(\alpha)}(\vec{r}_w) + k^2 p_w^{(\alpha)}(\vec{r}_w) = 0, \qquad \vec{r}_w \in D^{(\alpha)}, \tag{6.1}$$

where, $D^{(\alpha)}$ represents a bounded WBM domain. The BEM pressure field is governed by:

$$\nabla^2 p_b(\vec{r}_b) + k^2 p_b(\vec{r}_b) = 0, \qquad \vec{r}_b \in D^{(+)}, \tag{6.2}$$

where $D^{(+)}$ is an unbounded BEM domain. In addition, the BEM inherently satisfies the Sommerfeld radiation condition for 2D and 3D problems as follows:

$$\lim_{|\vec{r}_b|\to\infty} \left(|\vec{r}_b|^{\frac{n-1}{2}} \left(\frac{\partial p_b(\vec{r}_b)}{\partial |\vec{r}_b|} + jk p_b(\vec{r}_b) \right) \right) = 0, \qquad \text{with: n} = 2, 3. \tag{6.3}$$

In their decoupled forms, $p_w^{(\alpha)}(\vec{r}_w)$ and $p_b(\vec{r}_b)$ are entirely determined by the conditions imposed on their own boundaries, $\Gamma_\bullet$ and $S_\bullet$. To retrieve the total pressure $p_{tot}^{(\alpha')}(\vec{r})$, where α' indicates combined fields, $p_w^{(\alpha)}(\vec{r}_w)$ and $p_b(\vec{r}_b)$ are coupled by matching $p_w^{(\alpha)}(\vec{r}_w) + p_b(\vec{r}_b)$ to $p_{tot}^{(\alpha')}(\vec{r})$ along the boundary $\{\Gamma_\bullet \cup S_\bullet\}$:

$$p_{tot}^{(\alpha')}(\vec{r}) = p_w^{(\alpha)}(\vec{r}) + p_b(\vec{r}), \qquad \vec{r} \in \{\Gamma_\bullet \cup S_\bullet\}. \tag{6.4}$$

In order for the above equation to hold for the combined domain, $D^{(\alpha')}$, the left hand side and the right hand side should solve the Helmholtz equation (2.1) in the field $D^{(\alpha')} = \left\{ D^{(\alpha)} \cap D^{(+)} \right\}$. Indeed, this is the case, because the BEM satisfies the Sommerfeld radiation condition and the intersection of the BEM and the WBM domains results in the domain of interest. As such, equation (6.4) can be generalized to:

$$p_{tot}^{(\alpha')}(\vec{r}) = p_w^{(\alpha)}(\vec{r}) + p_b(\vec{r}), \qquad \vec{r} \in D^{(\alpha')}, \tag{6.5}$$

where $p_w^{(\alpha)}(\vec{r})$ is the pressure contribution from the WBM submodel, representing the bounded domain and $p_b(\vec{r})$ is the pressure contribution from the BEM submodel, representing the inclusion. For the remainder of the chapter, the combined field pressure for a bounded domain, $p_{tot}^{(\alpha')}(\vec{r})$, is written as $p_{tot}^{(\alpha)}(\vec{r})$ to have a better readability.

6.2.2 Unbounded problems

The hybrid BE-WBM concept is illustrated for a simple two scatterer problem in 2D in Figure 6.2. The WBM scattering object is enclosed by its own truncation, creating one level and the BEM creates a second one. These two levels divide the exterior field $D^{(+)}$ into two; $D^{(+,1)}$ and $D^{(+,2)}$, meaning that the exterior solution field $p_{tot}^{(+)}$ is composed of two purely outgoing fields $p_w^{(+)}$ and p_b. It should be noted that the outgoing field of the WBM submodel $p_w^{(+)}$, represents the pressure field outside of the truncation circle/sphere $\Gamma_{\bullet,t}$ ($\Gamma_{\bullet,t} = \Gamma_{v,t} \cup \Gamma_{p,t} \cup \Gamma_{Z,t} \cup \Gamma_{I,t}$) in the domain $D^{(+,1)}$, since only the unbounded wave function set satisfies the Sommerfeld radiation condition.

Both subproblems solve the Helmholtz equation and the Sommerfeld radiation condition in their corresponding levels in their uncoupled forms:

$$\nabla^2 p_w^{(+)}(\vec{r}_w) + k^2 p_w^{(+)}(\vec{r}_w) = 0, \qquad \vec{r}_w \in D^{(+,1)}, \tag{6.6}$$

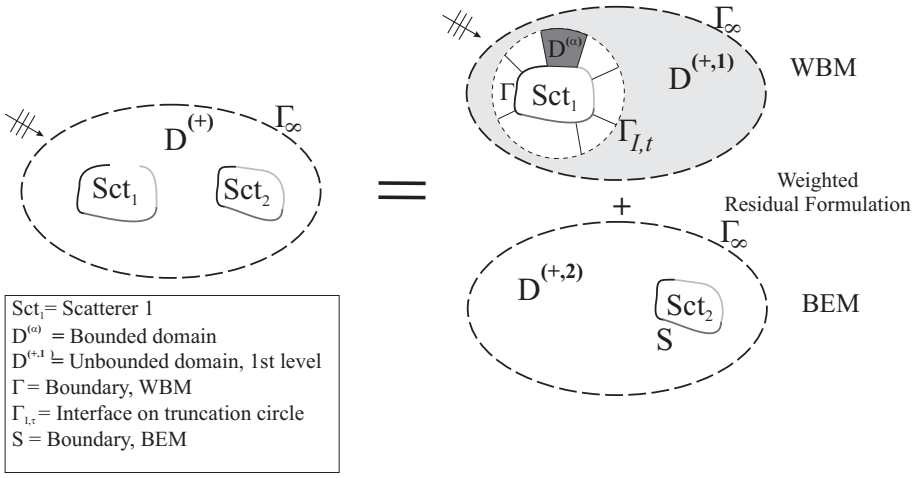

Figure 6.2: Graphical representation of the hybrid modeling concept for unbounded problems. The term $D^{(+,i)}$ is used for the domain in the ith level, $\Gamma_{I,t}$ is for the interfaces on the truncation circle.

$$\lim_{|\vec{r}_w|\to\infty}\left(|\vec{r}_w|^{\frac{n-1}{2}}\left(\frac{\partial p_w(\vec{r}_w)}{\partial|\vec{r}_w|}+jkp_w(\vec{r}_w)\right)\right)=0, \qquad \text{with: n = 2, 3.} \tag{6.7}$$

$$\nabla^2 p_b(\vec{r}_b)+k^2 p_b(\vec{r}_b)=0, \qquad \vec{r}_b \in D^{(+,2)}, \tag{6.8}$$

$$\lim_{|\vec{r}_b|\to\infty}\left(|\vec{r}_b|^{\frac{n-1}{2}}\left(\frac{\partial p_b(\vec{r}_b)}{\partial|\vec{r}_b|}+jkp_b(\vec{r}_b)\right)\right)=0, \qquad \text{with: n = 2, 3.} \tag{6.9}$$

where $p_w^{(+)}$ is determined by the conditions imposed on the $\Gamma_{\bullet,t}$ and p_b is determined by the conditions imposed on $S_\bullet$.

To retrieve the wave field of interest $p_{tot}^{(+)}$, the outgoing wave fields $p_w^{(+)}$ and p_b are coupled along $\{\Gamma_{\bullet,t}\cup S_\bullet\}$:

$$p_{tot}^{(+)}(\vec{r})=p_w^{(+)}(\vec{r})+p_b(\vec{r}), \qquad \vec{r} \in \{\Gamma_{\bullet,t}\cup S_\bullet\}. \tag{6.10}$$

In equation (6.10), both the left hand side and the right hand side solve Helmholtz equation (2.1) in the field $D^{(+)}=D^{(+,1)}\cap D^{(+,2)}$, together with the Sommerfeld radiation condition. This means, $p_{tot}^{(+)}(\vec{r})$ is equal to $p_w^{(+)}(\vec{r})+p_b(\vec{r})$ everywhere in the exterior field $D^{(+)}$ including $\{\Gamma_{\bullet,t}\cup S_\bullet\}$, which makes the initial domain decomposition valid [5]. Finally, for n_λ number of levels, equation (6.10) can be generalized to:

$$p_{tot}^{(+)}(\vec{r})=\sum_{i=1}^{n_\lambda-1}p_w^{(+,i)}(\vec{r})+p_b(\vec{r}), \qquad \vec{r} \in D^{(+)}. \tag{6.11}$$

For the proof and uniqueness of the proposed decomposition, the reader is referred to [59].

Equation (6.11) gives the field variable for the unbounded part of the problem. For the bounded domains of the WBM submodel, the pressure expansion does not include the pressure coming from the BEM submodel and written as:

$$p_{tot}^{(\alpha)}(\vec{r}) = p_{w}^{(\alpha)}(\vec{r}), \qquad \vec{r} \in D^{(\alpha)}. \tag{6.12}$$

Subsequently, a general pressure definition is given as:

$$p_{tot}^{(\gamma)}(\vec{r}) = \begin{cases} p_{tot}^{(\alpha)}(\vec{r}), & \vec{r} \in D^{(\alpha)}, \\ p_{tot}^{(+)}(\vec{r}), & \vec{r} \in D^{(+)}, \end{cases} \tag{6.13}$$

where, γ represents a general subdomain definition, which can be replaced by bounded domains α or unbounded domains $+$. Substituting equations (6.5) and (6.13) to the pressure definitions of both methods is the next step in deriving the hybrid BE-WBM system.

6.3 Boundary and interface residuals

Both WBM and BEM submodels are built through a weighted residual formulation. Therefore, a general residual definition for the hybrid method is given in this section before building the system of equations. The boundary residuals defined in equations (2.3), (2.4) and (2.5) are modified for the hybrid method. The new definitions of the residuals differ for bounded and unbounded domains as it is with the field variable definitions. As such, they are presented separately in the following two subsections. The WBM submodel uses interface residuals in addition to the boundary residuals as described in the previous chapters and any of the two as defined in equations (2.28) and (4.3) can be used.

6.3.1 Bounded problems

A general boundary residual of the hybrid method for bounded problems is defined as:

$$R_{\bullet}^{HYB(\alpha)}(p_{tot}^{(\alpha)}(\vec{r})) = R_{\bullet}^{(\alpha)}\left(p_{w}^{(\alpha)}(\vec{r}) + p_b(\vec{r})\right), \qquad \vec{r} \in \{\Gamma_{\bullet} \cup S_{\bullet}\}, \tag{6.14}$$

where $\bullet = v$, p or Z. The interface residual for the WBM submodel is defined as:

$$\begin{aligned} &R_{I}^{HYB(\alpha,\beta)}\left(p_{tot}^{(\alpha)}(\vec{r}), p_{tot}^{(\beta)}(\vec{r})\right) = \\ &\qquad R_{I}^{(\alpha,\beta)}\left(p_{w}^{(\alpha)}(\vec{r}) + p_b(\vec{r}), p_{w}^{(\beta)}(\vec{r}) + p_b(\vec{r})\right), \quad \vec{r} \in \{\Gamma_I\}. \end{aligned} \tag{6.15}$$

6.3.2 Unbounded problems

By using the total pressure definition given in equation (6.13), a general boundary residual is written as:

$$R_{\bullet}^{HYB(\gamma)}(p_{tot}^{(\gamma)}(\vec{r})) =$$

$$\begin{cases} R_{\bullet}^{(+)}\left(\sum_{i=1}^{n_\lambda-1} p_w^{(+,i)}(\vec{r}) + p_b(\vec{r})\right), & \vec{r} \in \{\Gamma_{\bullet,t} \cup S_{\bullet}\}, \\ & \text{with } \bullet = v,\ p \text{ or } Z. \\ R_{\bullet}^{(\alpha)}(p_w^{(\alpha)}(\vec{r})), & \vec{r} \notin \{\Gamma_{\bullet,t} \cup S_{\bullet}\}, \end{cases} \tag{6.16}$$

Subsequently, the interface residual is defined as:

$$R_I^{HYB(\gamma,\beta)}\left(p_{tot}^{(\gamma)}(\vec{r}), p_{tot}^{(\beta)}(\vec{r})\right) =$$

$$\begin{cases} R_I^{(+,\beta)}\left(\sum_{i=1}^{n_\lambda-1} p_w^{(+,i)}(\vec{r}) + p_b(\vec{r}), p_w^{(\alpha)}(\vec{r})\right), & \vec{r} \in \{\Gamma_{I,t}\}, \\ R_I^{(\alpha,\beta)}\left(p_w^{(\alpha)}(\vec{r}), p_w^{(\beta)}(\vec{r})\right), & \vec{r} \notin \{\Gamma_{I,t}\}. \end{cases} \tag{6.17}$$

6.4 The WBM submodel

The definition of the pressure contribution from the bounded WBM submodel, $p_w^{(\alpha)}$, is identical to the pressure expansion in equation (4.1). The pressure contribution from the WBM submodel for unbounded domains, $\sum_{i=1}^{n_\lambda-1} p_w^{(+,i)}(\vec{r})$ is given in equation (4.2).

With the boundary and interface conditions defined, the weighted residual formulation can be formed. This general expression holds for both bounded and unbounded problems. For each subdomain, the residual functions are orthogonalized with respect to a weighting function $\tilde{t}^{(\gamma)}$ or its derivative. For N_D number of subdomains and $N_I^{(\gamma)}$ number of interfaces for each subdomain, the weighted residual formulation is written as:

$$\begin{aligned}
&\sum_{\gamma=1}^{N_D} \Big[\int_{\Gamma_v^{(\gamma)}} \tilde{t}^{(\gamma)}(\vec{r})\, R_v^{HYB(\gamma)}(p_{tot}^{(\gamma)}(\vec{r}))\mathrm{d}\Gamma \\
&+ \int_{\Gamma_Z^{(\gamma)}} \tilde{t}^{(\gamma)}(\vec{r})\, R_Z^{HYB(\gamma)}(p_{tot}^{(\gamma)}(\vec{r}))\mathrm{d}\Gamma \\
&+ \int_{\Gamma_p^{(\gamma)}} -\mathcal{L}_v^{(\gamma)}(\tilde{t}^{(\gamma)}(\vec{r}))\, R_p^{HYB(\gamma)}(p_{tot}^{(\gamma)}(\vec{r}))\mathrm{d}\Gamma \\
&+ \sum_{\beta=1,\beta\neq\gamma}^{N_I^{(\gamma)}} \int_{\Gamma_I^{(\gamma,\beta)}} \tilde{t}^{(\gamma)}(\vec{r})\, R_I^{HYB(\gamma,\beta)} \left(p_{tot}^{(\gamma)}(\vec{r})\,,\, p_{tot}^{(\beta)}(\vec{r}) \right) \mathrm{d}\Gamma \Big] = 0.
\end{aligned} \tag{6.18}$$

It should be noted that the last term contains non-zero elements only for subdomains that have a common interface. A Galerkin approach is used to define the weighting functions $\tilde{t}^{(\gamma)}$. Irrespective of the type of the subdomain, i.e. bounded or unbounded, the weighting functions are chosen as the same set of acoustic wave functions defined for the corresponding subdomain:

$$\tilde{t}^{(\gamma)}(\vec{r}) = \sum_{w=1}^{n_w^{(\gamma)}} \Phi_w^{(\gamma)}(\vec{r}) t_w^{(\gamma)} = \Phi^{(\gamma)}(\vec{r})\, t^{(\gamma)}. \tag{6.19}$$

Substitution of the total pressure definition (6.5) or (6.13) and the weighting function expansion (6.19) into the weighted residual formulation (6.18) yields the first part of the system of equations for the hybrid model.

6.5 The BEM submodel

For the BEM submodel, an indirect variational formulation is used. In its indirect form, the primary variables of the boundary integral equation are defined as the difference of the pressure, and the difference of the normal gradient of the pressure between both sides of the boundary surface [149] . These variables are called the double layer potential μ and single layer potential σ, respectively.

$$\mu(\vec{r}) = p(\vec{r}^{\,+}) - p(\vec{r}^{\,-}) \qquad \vec{r} \in S, \tag{6.20}$$

$$\sigma(\vec{r}) = \frac{\partial p(\vec{r}^{\,+})}{\partial n} - \frac{\partial p(\vec{r}^{\,-})}{\partial n} \qquad \vec{r} \in S, \tag{6.21}$$

where $+$ denotes the variables on one side and $-$ on the other side as shown in Figure 6.3. By assuming a thin boundary, the single layer and double layer potentials are written for boundary conditions in equations (2.3), (2.4) and

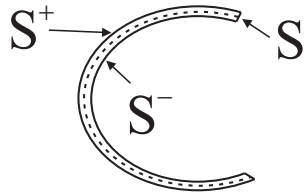

Figure 6.3: Indirect BEM's boundary definitions

(2.5) as:

$$\mu(\vec{r}) = 0, \quad \vec{r} \in S_v \; ; \qquad \sigma(\vec{r}) = 0, \quad \vec{r} \in S_p \; ; \qquad \sigma(\vec{r}) = -jk\bar{\beta}\mu, \quad \vec{r} \in S_Z, \tag{6.22}$$

where $\bar{\beta} = \rho_0 c/\bar{Z}$. The pressure contribution $p_b(\vec{r})$ from the BEM submodel, which is given by the indirect boundary integral equations is written as:

$$\begin{aligned} p_b(\vec{r}) = &- \int_{S_p} \sigma(\vec{r}_a) G(\vec{r}, \vec{r}_a) \mathrm{d}S + \int_{S_v} \mu(\vec{r}_a) \frac{\partial G(\vec{r}, \vec{r}_a)}{\partial n(\vec{r}_a)} \mathrm{d}S \\ &+ \int_{S_Z} \mu(\vec{r}_a) \left(\frac{\partial G(\vec{r}, \vec{r}_a)}{\partial n(\vec{r}_a)} + jk\bar{\beta}(\vec{r}_a) G(\vec{r}, \vec{r}_a) \right) \mathrm{d}S. \end{aligned} \tag{6.23}$$

with $\vec{r}$ being the position vector where the field variable is calculated and $\vec{r}_a$ being the position vector on the boundary of the geometry. The reader is referred to [149] for the detailed information regarding the derivation of the indirect boundary integral equation. The Green's function $G(\bullet, \bullet)$ is defined for 2D problems as:

$$G(\vec{r}, \vec{r}_a) = -\frac{j}{4} H_0^{(2)}(k \left| \vec{r} - \vec{r}_a \right|), \tag{6.24}$$

where $H_0^{(2)}$ is the zero-order Hankel function of the second kind and for 3D problems as:

$$G(\vec{r}, \vec{r}_a) = \frac{e^{-jk|\vec{r} - \vec{r}_a|}}{4\pi \left| \vec{r} - \vec{r}_a \right|}. \tag{6.25}$$

A weighted residual formulation is applied on the boundary residuals to build up the BEM submodel.

$$\begin{aligned} \forall(\delta\sigma, \delta\mu) : \quad & \int_{S_p} R_p^{HYB}(p_{tot}^{(\gamma)}(\vec{r})) \, \delta\sigma \, \mathrm{d}S + \\ & \int_{S_v} R_v^{HYB}(p_{tot}^{(\gamma)}(\vec{r})) \, \delta\mu \, \mathrm{d}S + \int_{S_Z} R_Z^{HYB}(p_{tot}^{(\gamma)}(\vec{r})) \, \delta\mu \, \mathrm{d}S = 0. \end{aligned} \tag{6.26}$$

Following a Galerkin approach, the test functions are chosen the same as the potentials. Subsequently, substitution of the pressure definition (6.5) or (6.13) to above equation gives the BEM submodel of the hybrid system.

6.6 The hybrid system

Equations (6.18) and (6.26) should be solved together to get the unknowns of the hybrid system. The numerical discretization of the system leads to the following square matrix equation of n_{tot} number of degrees of freedom, where n_{tot} is the sum of degrees of freedom in the BEM submodel and the WBM submodel:

$$\begin{bmatrix} A_W & C_{WB} \\ C_{BW} & A_B \end{bmatrix} \begin{bmatrix} t \\ b \end{bmatrix} = \begin{bmatrix} F_W \\ F_B \end{bmatrix}. \tag{6.27}$$

where A_W is the system matrix of the WBM submodel and A_B of the BEM, as they would be in their standalone forms. C_{WB} and C_{BW} are the coupling matrices resulting from the extra pressure values in the boundary residuals coming from the companion method. F_W and F_B are the forcing terms coming from the prescribed boundary conditions of the corresponding methods or possible external excitations. The terms t and b are the unknowns of the hybrid system, where t represents the unknown weighting factors of the corresponding wave functions and b represents the possible combination of the unknown potentials.

A problem with Neumann boundary conditions is assumed to demonstrate what the system of equations looks like. The following equations hold for an unbounded, 2 scatterer problem or a bounded problem with single WBM domain and a BEM inclusion. In such a case, the system matrices and the right hand sides of the hybrid model are constructed as follows:

$$A_W = \int_{\Gamma_v} \frac{j}{\rho_0 \omega} \Phi^T(\vec{r}_w)\; n^T(\vec{r}_w)\; B(\vec{r}_w)\, \mathrm{d}\Gamma, \tag{6.28}$$

$$C_{WB} = \int_{\Gamma_v} \frac{j}{\rho_0 \omega} \Phi^T(\vec{r}_w) \int_{S_v} N_\mu(\vec{r}_a) \frac{\partial G(\vec{r}_a, \vec{r}_w)}{\partial n(\vec{r}_a) \partial n(\vec{r}_w)}\, \mathrm{d}S\, \mathrm{d}\Gamma, \tag{6.29}$$

$$C_{BW} = \int_{S_v} \Phi^T(\vec{r}_a)\, N_\mu(\vec{r}_a)\, \mathrm{d}S, \tag{6.30}$$

$$A_B = \int_{S_v} \int_{S_v} N_\mu(\vec{r}_a)\, N_\mu(\vec{r}_b)\, \frac{\partial G(\vec{r}_b, \vec{r}_a)}{\partial n(\vec{r}_a) \partial n(\vec{r}_b)} \mathrm{d}S\, \mathrm{d}S, \tag{6.31}$$

$$F_W = \int_{\Gamma_v} \Phi^T(\vec{r}_w)\; \bar{v}_n(\vec{r}_w)\, \mathrm{d}\Gamma, \tag{6.32}$$

$$F_B = \int_{S_v} j \rho_0 \omega \bar{v}_n(\vec{r}_a)\; N_\mu(\vec{r}_a)\, \mathrm{d}S, \tag{6.33}$$

where $\vec{r}_a$ and $\vec{r}_b$ are the position vectors on the BEM boundaries and $\vec{r}_w$ is the position vector on the WBM boundaries. $N_\mu(\bullet)$ is the vector of global shape functions used in the discretization of the BEM boundaries. Finally, $B(\bullet)$ is the gradient of acoustic wave functions $\Phi(\bullet)$:

$$B(\bullet) = \nabla \Phi(\bullet). \tag{6.34}$$

The derivation of other boundary conditions and their combinations are straightforward and omitted here to avoid repetition.

6.7 Solution and post-processing

After the system of equations is solved, the field pressure can be calculated by using the calculated wave function contribution factors and the potentials. For bounded problems equation (6.5) is used and for unbounded problems equation (6.13) is used. Derived quantities can be calculated from analytical derivatives of the same equations.

6.8 Modeling principles and properties

For multiple scattering problems, geometrically complex scatterers are modeled with the BEM and geometrically simple scatterers are modeled with the WBM. The hybrid method does not just increase the efficiency, it also widens the possible range of applications that can be tackled by both methods with ease. Although it is possible with WBM to treat zero thickness boundaries, when the boundary shape is highly complex, the decomposition of the field to convex subdomains might be impossible or impractical. On the other hand, the zero thickness boundaries can be addressed with BEM easily by using an indirect variational (Galerkin) formulation, which is the preferred BEM formulation for the hybrid method. Another possibility that comes with the hybrid method is the ability to add piecewise continuous heterogeneities to the field by using the WBM. Using bounded subdomains is already a part of the procedure in solving unbounded problems, therefore the only requirement is to change the fluid properties of the corresponding bounded subdomain. Although adding heterogeneities with the indirect variational BEM formulation is possible through the Boundary Element Tearing and Interconnecting (BETI) Methods [86], they require special treatments for stability and the coupling of the BETI and Fast Multipole Method for Helmholtz problems is still to be done [118]. Therefore, the proposed hybrid method provides a very easy and efficient treatment of heterogenities that can co-exist with open boundaries. There are other multidomain BEM formulations available in literature to model heterogeneities [26]. However, they use direct collocation BEM formulations and they double the number of degrees of freedom which increase the computational cost substantially.

For the inclusion problems, the main idea is to use the BEM for the complex inclusions, while benefiting from the efficient solution of the WBM for moderately complex cavities. Such geometrical configurations are common in engineering applications. One prominent example is loudspeaker cabins with diffusers. Various room acoustic applications have also similar settings. In addition to the goal of having a more efficient tool than the FEM for bounded problems, the hybrid method also aims to bring certain conceptual advantages over the FEM. One of them is the ease of pre-processing, in that, refinement of the model for higher frequencies only needs a more refined discretization of the boundaries of the inclusions and an increased number of wave functions.

Another conceptual advantage of the proposed method is that, in the case of optimization problems where the topology or the position of inclusions/panels in large acoustic cavities are to be configured, the hybrid BE-WBM provides a very efficient solution. If the shape and position of the inclusions are to be optimized, the model for the cavity, i.e. the WBM submodel, can stay the same and only the BEM submodel and the coupling matrices are needed to be recalculated. If only the position needs to be changed, then only the coupling matrices are needed to be recalculated. Therefore, while the hybrid method provides a very efficient solution to forward problems, it also opens doors to efficient solving of inverse problems.

6.9 Conclusion

The theory of the hybrid BE-WBM is presented in this chapter. The method is derived for inclusion and multiple scattering problems. The domain decomposition for both applications are presented, which demonstrates the superposition principle that the hybrid method is built upon. The properties of the method are discussed. The numerical verifications to test the accuracy and the performance of the method are presented in the next chapter.

Chapter 7

Hybrid BE-WBM: numerical verifications

This chapter presents numerical verification cases for the hybrid BE-WBM method. The method is developed for inclusion and multiple scattering problems, as detailed in the previous chapter. For both problem types, 2D and 3D applications are presented here. The following sections comprise six numerical verification cases to assess the accuracy and benchmark the performance of the method against the state of the art methods like the BEM and the FEM.

7.1 Numerical verifications for multiple scattering problems

Three numerical verification cases are presented in this section to demonstrate the accuracy and the performance of the proposed hybrid method for multiple scattering problems. The first verification case is chosen such that the hybrid method can be compared to an analytical solution. Therefore, it concentrates on assessing the accuracy. The second and third verification cases tackle a more general configuration for which no exact solution exist. A fine BEM simulation is used as the reference for the accuracy while the performance of the hybrid method is assessed by comparing it to the BEM and the ML-WBM first and to the FM-BEM next. For all the simulations, air with properties of 340 m/s for speed of sound c_0, and 1.225 kg/m^3 for the fluid density ρ_0 is used.

7.1.1 Accuracy assessment

The first verification case is composed of two circular geometries in an unbounded domain with 0.5 m and 1 m radii placed at the coordinates (0,0) m and (0,3) m, respectively, as shown in Figure 7.1. The circle with 0.5 m radius is modeled with sound soft boundary conditions ($\bar{p} = 0$) and constitutes the BEM submodel of the hybrid model. The circle with 1 m radius is modeled with waves propagating through the object such that it behaves like an acoustically transparent circle and constitutes the WBM submodel. There is an external excitation as a plane wave at 45 degrees angle. As a result, the wave field created represents that of a single scatterer with plane wave excitation. In other words, a physical single scatterer problem is converted into an artificial multiple scattering configuration. The motivation behind this configuration is to create an example that can be compared with an exact solution, i.e. the Anger-Jacobi series expansion [75], to assess the accuracy of the proposed hybrid method. Figure 7.2 shows the wave field given by the analytical solution at 500 Hz.

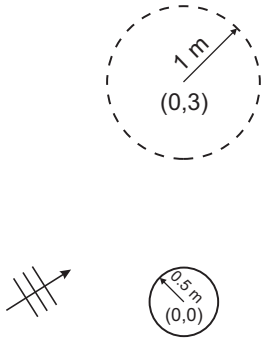

Figure 7.1: Problem definition for the first verification case. For the hybrid BE-WBM, the circle represented with the dashed line is modeled with the WBM and the other circle is modeled with the BEM.

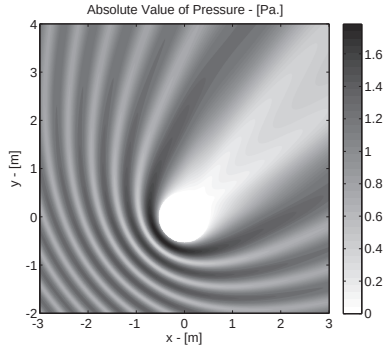

Figure 7.2: Wave field given by the analytical solution at 500 Hz

While this verification case creates a very convenient configuration for accuracy assessment, it is still not straight forward to evaluate the hybrid method because the final accuracy depends on the accuracies of the individual methods that form the hybrid method. Figures 7.3 and 7.4 show the absolute value of the relative pressure error (ref. analytical solution) given by two different hybrid BE-WBM models. The error criterion is defined as follows:

$$\epsilon(p(\vec{r})) = \frac{|p(\vec{r}) - p_{ref}(\vec{r})|}{|p_{ref}(\vec{r})|}. \tag{7.1}$$

The first model in Figure 7.3 uses 256 degrees of freedom (DoF) for the BEM submodel and 213 DoF (unbounded wave functions for this case) for the WBM submodel while the second model in Figure 7.4 uses 512 DoF for the BEM submodel and 127 for the WBM submodel. By looking at the error on the wave field in Figure 7.3, it is not possible to observe the presence of the transparent WBM circle. This is because the WBM submodel is far more accurate than the BEM submodel for the given number of DoF while in Figure 7.4, the WBM submodel becomes the bottleneck. At the end, the hybrid method is expected to be driven by the error coming from both methods and the accuracy is expected to be driven by the lowest accuracy provided from the two. Therefore, an important property to verify is if the hybrid BE-WBM can really converge to the accuracy limits drawn by its individual submodels to demonstrate whether the coupling algorithm hampers the accuracy or not.

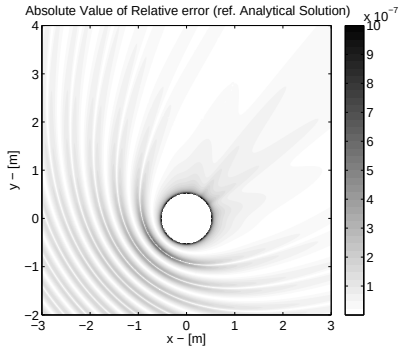

Figure 7.3: Error field at 500 Hz given by the hybrid BE-WBM with 256 DoF for the BEM submodel and 213 DoF (unbounded wave functions) for the WBM submodel.

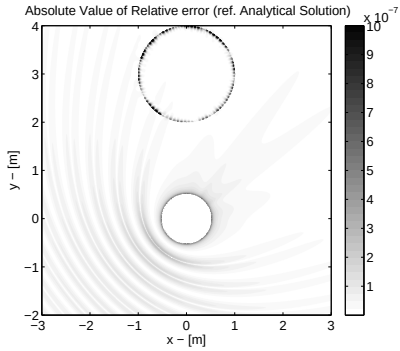

Figure 7.4: Error field at 500 Hz given by the hybrid BE-WBM with 512 DoF for the BEM submodel and 127 DoF (unbounded wave functions) for the WBM submodel.

To test this statement, a convergence analysis is performed, showing the behavior of the hybrid method with various combinations of DoF. The error criterion is defined as the spatial average of the amplitude of the relative pressure error, which is given by:

$$\epsilon_{av}(p(\vec{r})) = \frac{1}{N_{rp}} \sum_{i=1}^{N_{rp}} \frac{|p(\vec{r_i}) - p_{ref}(\vec{r_i})|}{|p_{ref}(\vec{r_i})|} \tag{7.2}$$

where N_{rp} is the number of receiver points. 14300 equally distributed receiver points from the wave field shown in Figures 7.3 and 7.4 are used for the convergence test.

First, the number of DoF of the BEM submodel is fixed and the analysis is run by increasing the number of wave functions. The results are presented in Figure 7.5. In a second step, the number of DoF of the WBM submodel is

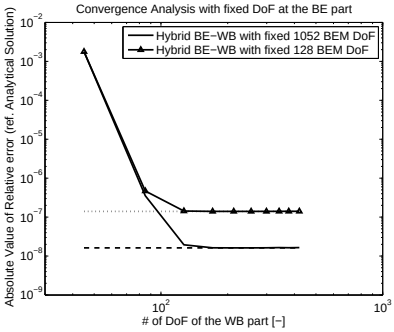

Figure 7.5: Dashed line = BEM with 1052 DoF, dotted line = BEM with 128 DoF

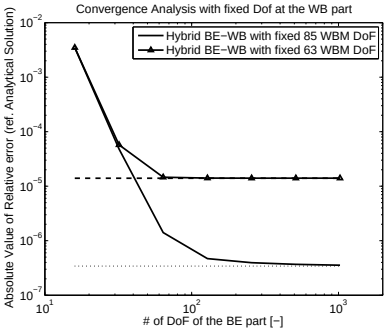

Figure 7.6: Dashed line = WBM with 65 DoF, dotted line = WBM with 85 DoF

fixed and the BEM submodel is refined which is presented in Figure 7.6. The straight dashed and the dotted lines in the figures represent the accuracy given by either BEM or ML-WBM in their pure forms where they have the same fixed number of DoF as the fixed submodel of the hybrid method. Therefore, they are representing the accuracy limits of their corresponding submodels in the hybrid method.

Looking at these figures, it is apparent that the hybrid method converges to the given limits, showing that the coupling algorithms do not hamper the accuracy. As a result, it is demonstrated that the hybrid method keeps converging as long as the contributions from the WBM and the BEM submodels are valid.

Another important demonstration through this example is that the WBM successfully simulates the propagating waves through an object in its pure and hybrid form. This inherent property of the WBM leads to the ability to model heterogeneities in the system. If one needs to model a heterogeneity, the only thing to do is to change the fluid properties of the corresponding bounded domains. Consequently, this ability opens doors to a wide range of configurations. Its importance stems from the fact that it presents a very convenient way to introduce heterogeneities to the indirect variational BEM formulation such that open boundary geometries can co-exist with permeable objects with ease.

7.1.2 Performance assessment 1

The second verification case is composed of again two scatterers, however, this time with one complex and one simple geometry. A seat shaped geometry is used to represent the complex geometry, while a circular geometry is used for the simple one as shown in Figure 7.7. Three methods are compared, namely the BEM, the ML-WBM and the hybrid BE-WBM. For the hybrid method, the circle is modeled with the WBM and the seat is modeled with the BEM. For

the ML-WBM; the truncation circle used for the seat, the subdomain division and their corresponding bounding boxes are shown in Figure 7.7.

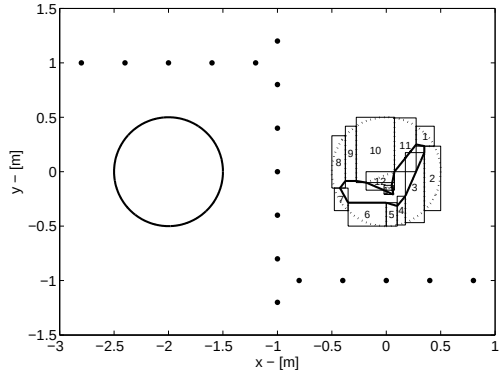

Figure 7.7: Problem definition for the second verification case: geometry of the scatterers and position of receivers (dots).

Homogeneous Dirichlet conditions are defined on the boundaries of both objects with a value of 1 Pa. The acoustic pressure field values at 500 Hz are shown in Figure 7.8 and Figure 7.9 for the hybrid BE-WBM and ML-WBM, respectively, and they are matching very well with each other.

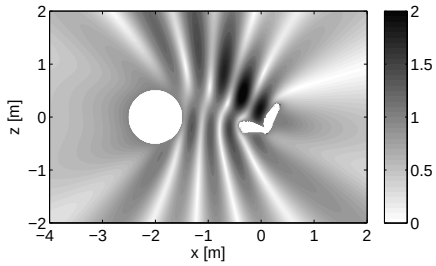

Figure 7.8: Pressure Amplitude [Pa] at 500 Hz for the hybrid BE-WBM

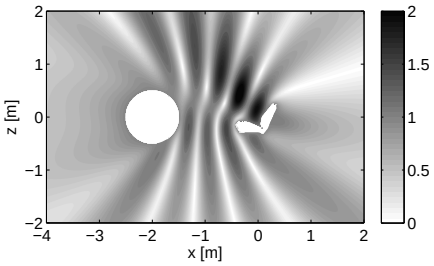

Figure 7.9: Pressure Amplitude [Pa] at 500 Hz for the ML-WBM

In addition, the frequency response function (FRF) curves of the spatial average of the sound pressure levels comparing the three methods are given in Figure 7.10 and 7.11 from 100 to 1000 Hz and 1000 to 2000 Hz. A reference BEM simulation which uses a very fine mesh is also presented. The spatial average is taken over the 17 receiver points shown with dots in Figure 7.7. The simulations are run for the frequency range from 100 to 2000 Hz with steps of 10 Hz. The detailed information about mesh validities of the models is listed in Table 7.1. For the regular BEM simulation, two different meshes are used; a coarser mesh until 1000 Hz and a finer one for the rest. The seat part of the BEM mesh is kept identical for the hybrid BE-WBM model, i.e. again a coarser and a finer mesh. The coarser mesh is expected to yield accurate predictions up to

1000 Hz and the finer mesh, up to 2260 Hz; assuming 10 linear elements per wavelength while the reference mesh is expected to be accurate up to 17 kHz using the same criterion.

A careful look at Figures 7.10 and 7.11 reveals that all three methods are in good agreement with each other on the FRF level, while they are agreeing with the reference calculation. However, a fair performance comparison requires a more detailed look on the error levels. Subsequently, the spatial average of the absolute value of the relative error as defined in equation (7.2), with taking the fine BEM solution as the reference is presented in Figure 7.12. The spatial average is again taken over 17 receiver points. For this simulation, the aim is to have all three methods to be around the engineering accuracy of 1 %. Looking at the error levels, although the hybrid BE-WBM and the pure BEM models perform slightly better than the ML-WBM model, they are mostly giving the same error level and it should be fair to check the calculation times. A small note here is that the pure BEM and the hybrid BE-WBM curves are on top of each other. This is in agreement with the statement made in the previous subsection. The accuracy bottleneck for the hybrid method for this simulation comes from the BEM submodel since the single circle solution from the WBM is highly accurate.

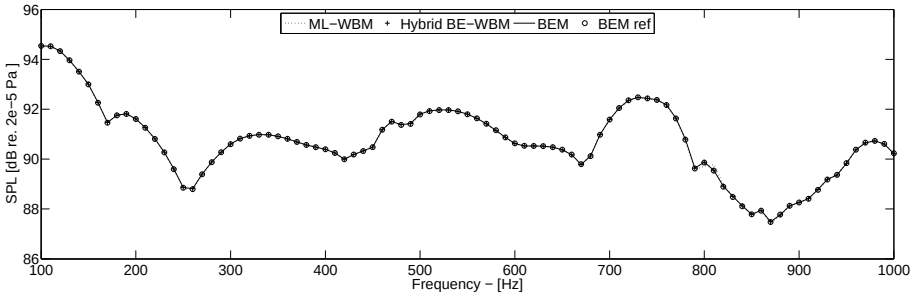

Figure 7.10: Spatial average of SPL over 17 receiver points from 100 to 1000 Hz

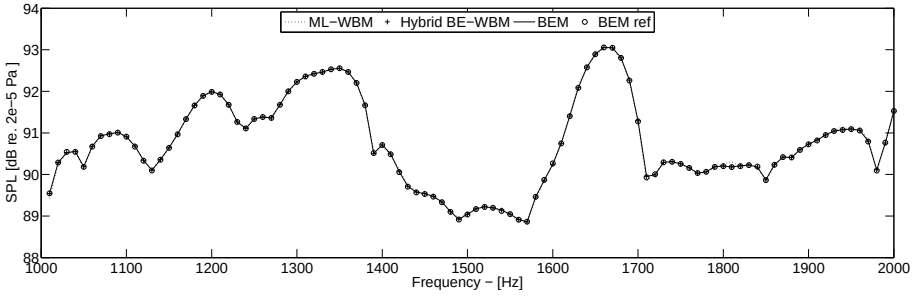

Figure 7.11: Spatial average of SPL over 17 receiver points from 1000 to 2000 Hz

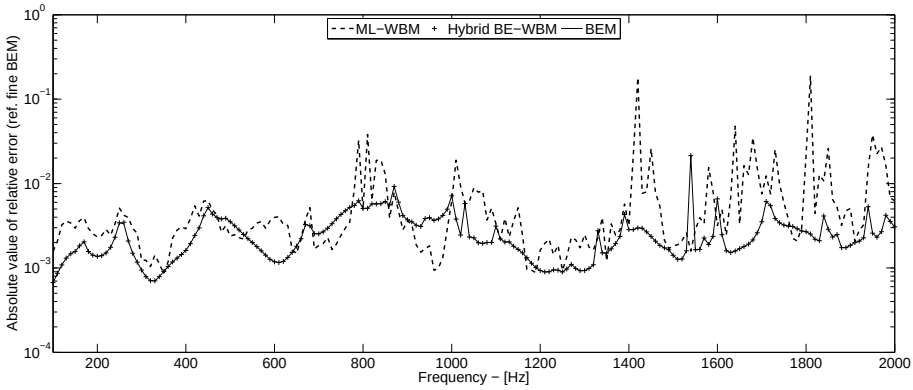

Figure 7.12: Absolute value of relative error (ref. fine BEM) averaged over 17 receiver points

With the FRF and error figures presented, the performance comparisons can be examined. The calculation times for the analysis shown in Figure 7.10 and 7.11 are presented in Table 7.1. All the benchmarks are run on a Windows 7 machine with Intel Core 2 Duo, 2.80 GHz CPU and with 4 GB RAM. For all three methods, dedicated Matlab codes are used to have a fair comparison. It should be noted that the BEM code utilized in the benchmarks is an efficient implementation of the method [74].

Table 7.1: Model information for the calculations between 100 to 2000 Hz with 10 Hz steps

	BEM Reference	BEM (100-1000 Hz / 1000-2000 Hz)	Hybrid BE-WBM (100-1000 Hz / 1000-2000 Hz)	ML-WBM
♯ DoF	2761	162 / 367	81-145 / 234-306	616-2526
mesh validity 6 el./ λ [Hz]	28330 Hz	1666 Hz / 3770 Hz	1666 Hz / 3770 Hz	-
mesh validity 10 el./ λ [Hz]	17000 Hz	1000 Hz / 2260 Hz	1000 Hz / 2260 Hz	-
total solving time [s]	41188 s	497 s	243 s	557 s

Looking at the calculation times, first thing to notice is the efficiency of the hybrid BE-WBM compared to the BEM and the ML-WBM. The hybrid method shows its efficiency over BEM by using the inexpensive and accurate WBM solution for the simple scatterer object. Moreover, it shows its efficiency over the ML-WBM by benefiting from BEM's capability of handling complex geometries. As a result, for the example at hand the calculation times are nearly halved compared to the BEM and the ML-WBM.

7.1.3 Performance assessment 2

The second performance assessment case deals with a 3D problem. The geometry is composed of 48 identical spherical scatterers and two curved panels, as shown in Figure 7.13. The spheres are placed as rows of $4 \times 3 \times 4$ in x, y and z axes, respectively. The radii of the spheres are 0.25 m and they are equally spaced from each other with 0.125 m distance in between. The curved panels are $0.4 \times 1.1 \times 3$ m in size and also identical with each other. The excitation to the system is a plane wave with 1 Pa magnitude that propagates along the y axis. All the boundaries have sound hard ($\bar{v}_n = 0$) boundary conditions.

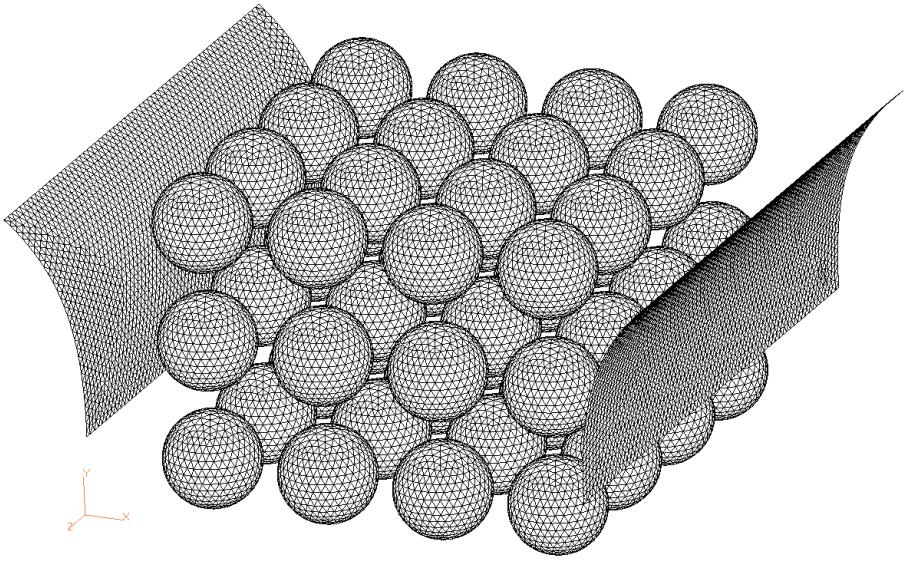

Figure 7.13: The mesh used for FMBEM calculations

These kinds of configurations are used as acoustic lens designs [148] in sonar applications, as sound shields or acoustic filters.

For the considered problem, the performance of the hybrid method is compared to the FM-BEM, as the size of the problem is already large and the conventional BEM is not efficient for such problems. However, for assessing the accuracy of the hybrid method, we do use a BEM model with a fine mesh as a reference.

For the hybrid BE-WBM model, the panels are modeled with the BEM and the spheres are modeled with the WBM. It is not practical to model the whole geometry with the ML-WBM because the space between the curved panels and their possible truncation spheres can not be divided into convex subdomains effectively. As a consequence, the ML-WBM is left out of the comparisons. In the end, this problem also demonstrates a case where the ML-WBM on its own is not adequate and the WBM can only be utilized through the hybrid approach.

The first comparison is presented on the contour map level for the hybrid BE-WBM and the reference BEM simulations in Figures 7.14 and 7.15 at 500 Hz. The field points are chosen on the x-y plane where $z = 0$ for all points. Both figures look very similar, showing the good accuracy of the hybrid BE-WBM model.

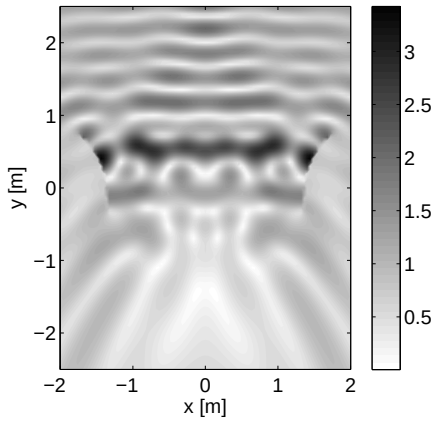

Figure 7.14: Pressure Amplitude [Pa] at 500 Hz for the fine BEM

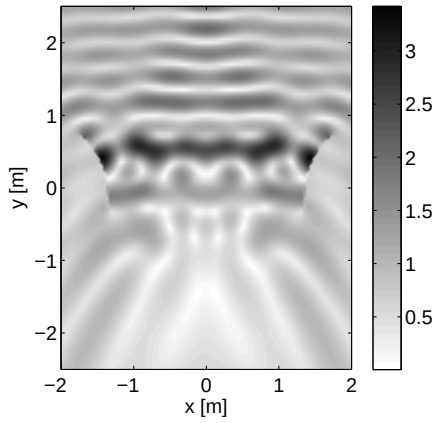

Figure 7.15: Pressure Amplitude [Pa] at 500 Hz for the hybrid BE-WBM

Next is the comparison of the FM-BEM and the hybrid BE-WBM over a wide frequency range with a fine BEM reference. For the FM-BEM simulations, LMS Virtual Lab R11 is used, which has a high frequency FM-BEM implementation [51]. The reference BEM simulations are also carried out using the same software. For the hybrid method, the WBM submodel is modeled in Matlab and the BEM submodel is modeled with in-house Fortran functions that are created with inspiration from the sample codes in [149] and that are called from the Matlab interface. The model details for all three models are given in Table 7.2, showing the number of DoF, the number of BEM elements and the validity of the used meshes. The FM-BEM and the BEM models use linear triangular elements, as well as the BEM submodel of the hybrid method.

The simulations are run from 150 Hz to 500 Hz with 5 Hz steps. The reasoning behind the chosen frequency is two fold. For the low frequency limit, 150 Hz is chosen such that the high frequency FM-BEM implementation used in the LMS software can have a good convergence behavior. For the high-frequency limit, although the 10 elements per wavelength rule shows that the mesh used for the FM-BEM is expected to yield accurate results up to 600 Hz, the predictions start to deteriorate already at 500 Hz due to the existence of the open boundaries. Furthermore, a BEM reference is essential in this comparison and going to a finer FM-BEM mesh would mean that a finer BEM reference model is required as well. However, going to a finer reference model was not possible because of the available computational power. All the simulations are run on a machine with 8 Intel Xeon X5650, 2.67 GHz Cpus and 32 GB RAM, while the FM-BEM and the hybrid BE-WBM simulations

are benchmarked using single processor. On a side note, both methods can be efficiently parallelized however they are limited to one processor for a comparison in a more controlled environment.

Figure 7.16 shows the FRF curves of the sound pressure levels for the three methods. The values are spatially averaged over 121 equally spaced points, chosen on a 3×2 m grid on the y-z plane with $x = 0$ for all points. Both hybrid BE-WBM and FM-BEM results match very well with the BEM reference. A more detailed error analysis is given in Figure 7.17 with the error criterion defined in equation (7.2). The simulations are aimed to have an engineering accuracy of 1 % and both methods satisfy that criterion while providing very similar error levels. For the FM-BEM simulation, the final normalized residual and the inner loop normalized residual for the iterative solver are chosen as 0.001 to achieve the desired accuracy and the number of iterations resulted between 25 to 40 for the given frequency range.

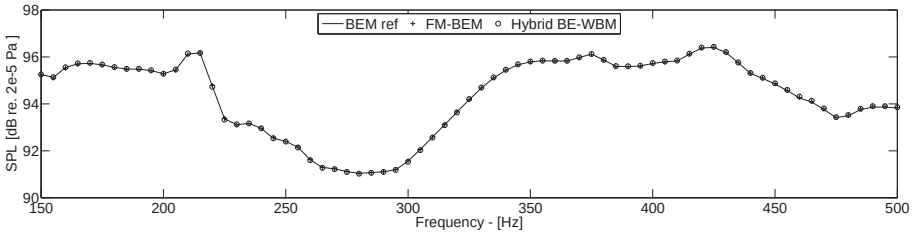

Figure 7.16: Spatial average of SPL over 121 receiver points from 150 to 500 Hz

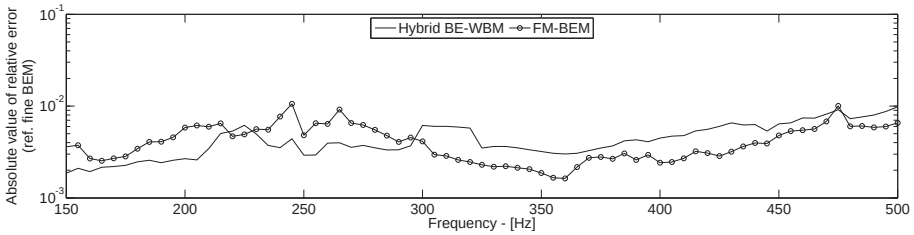

Figure 7.17: Absolute value of relative error (ref. fine BEM) averaged over 121 receiver points

As both methods give similar accuracy, fair performance comparisons can be made. Table 7.2 shows the calculation times as the total solution time over the whole frequency range and the average calculation time per frequency. The simulation times consist of system building and solution times. For the problem at hand, the hybrid method performs almost 6 times faster than the FM-BEM showing the efficiency of the proposed method.

Table 7.2: Model information for the calculations between 150 to 500 Hz with 5 Hz steps

	BEM Reference	FM-BEM	Hybrid BE-WBM
♯ DoF (nodes or wave func.)	39426	29076	(4548 B + 432 W)/ (4548 B + 2352 W)
Number of BEM elements	77952	57572	8708
mesh validity 10 el./ λ [Hz]	1080 Hz*	600 Hz	600 Hz
total solving time for FRF [s]	183418 s**	118707 s	20251 s
average solving time per freq. [s]	2583 s**	1672 s	285 s

* The value represents the refinement on the panels as they are the bottleneck in the accuracy of the model

** The timings for the reference calculation are obtained by using 8 processors

7.1.4 Discussion of the results

It should be noted that the performance comparison for the last case involves an in-house research code and a commercial software code. It is likely that performance optimizations could be performed both on the methodological side as well as on the code implementation side for both benchmarked approaches. This may impact the eventual performance comparison, but the reported benchmark is believed to have some indicative character.

In addition to the demonstrated performance advantage, an even more important advantage is the potential of the hybrid method in optimization problems. In a scenario where only one of the submodels of the hybrid method is optimized, i.e. the optimization of the spherical scatterers with the fixed panels or vice versa, the optimization of the panels with the fixed spheres; the fixed submodel of the hybrid method can be reused in the optimization iterations. This approach would be less straightforward with the FM-BEM, since a change in the geometry would lead to the recalculation of the multipole algorithms as well. Therefore, the hybrid method can be instrumental and highly effective in optimization problems, which will be investigated further in the future.

7.2 Numerical verifications for inclusion problems

In order to assess the accuracy and the performance of the method for inclusion problems, three numerical verification cases are presented in this section. The first verification case is a 2D problem, which aims to demonstrate the accuracy of the method and test the limits of the coupling algorithms. The second case is a 3D problem and is aimed at showing the convergence behavior of the method. The final case is also a 3D problem and demonstrates the performance of the

method over a wide frequency range. Dirichlet, Neumann and Robin boundary conditions are used throughout different verifications. The reference methods for error calculations are chosen depending on the geometry of the verification case. For the first two cases, the BEM and the ML-WBM are used as references, while for the third case, the FEM is the reference. For all simulations, the acoustic medium is air with mass density ρ_0, equal to 1.225 kg/m^3 and the speed of sound c_0, equal to 340 m/s.

7.2.1 Accuracy assessment

The first case is chosen to effectively assess the accuracy of the coupling algorithms. The aim of this study is to indicate that the coupling algorithms do not introduce an extra error in the field and that the hybrid method manages to converge to the limit set by its least accurate submodel. In order to do so, full model references of the ML-WBM and the BEM are needed. As such, a simple geometry is chosen to provide a good ML-WBM reference.

A 2D problem is considered (see Figure 7.18) with a 1 m × 1 m square box and a circle with 0.25 m radius placed in the center of the box (with its origin at the coordinate (0,0)). Dirichlet boundary conditions are used for this case. The boundary of the box has a value of $\bar{p} = 1$ Pa and the boundary of the circle is assigned to $\bar{p} = 0$ Pa.

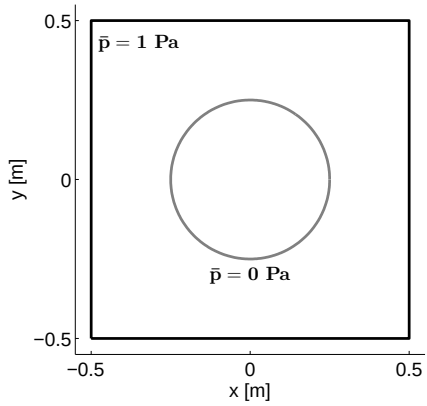

Figure 7.18: Problem geometry for the 2D case. The cavity boundaries are assigned to $\bar{p} = 1$ Pa and the circle boundary is assigned to $\bar{p} = 0$ Pa.

In order to assess the coupling accuracy, one part of the hybrid method (the WBM or the BEM submodel) is fixed and the other part is refined. Subsequently, the accuracy of the hybrid model is compared with the full BEM or full ML-WBM models that have the same number of degrees of freedom (DoF) on their associated geometries, i.e. the circle for the BEM and the cavity for the ML-WBM. The simulations are run at 2000 Hz and 5000 Hz. The

error criterion is the same as defined in equation (7.2). For all the following convergence figures in this subsection, 60 post processing points are defined. The points are equally distributed on a circle of 0.35 m radius, whose origin is set at the coordinate (0,0). Figures 7.19(a) and 7.19(b) show the case, where the number of DoF of the WBM submodel is fixed and the number of DoF of the BEM submodel is increased. The BEM submodel of the hybrid method uses linear elements with element lengths changing from 0.049 m to 0.001 m in 8 refinement steps. The reference model for the two figures is the ML-WBM. A high truncation rule of $T = 10$ is used to provide a good reference. The corresponding number of DoF of the reference model is given in the figures. The two straight lines with dashes and dots mark the accuracies given by the full ML-WBM models, when they use the same number of DoF on the box (with $T = 2$ and $T = 3$). It is clear that, when the hybrid method uses fixed WBM DoF, it converges to the limits given by the full ML-WBM models. When the number of DoF on the WBM submodel is chosen as equal to the reference ML-WBM model, the error curves keep converging. This shows that the coupling algorithms for the WBM submodel do not hinder the accuracy of the hybrid method.

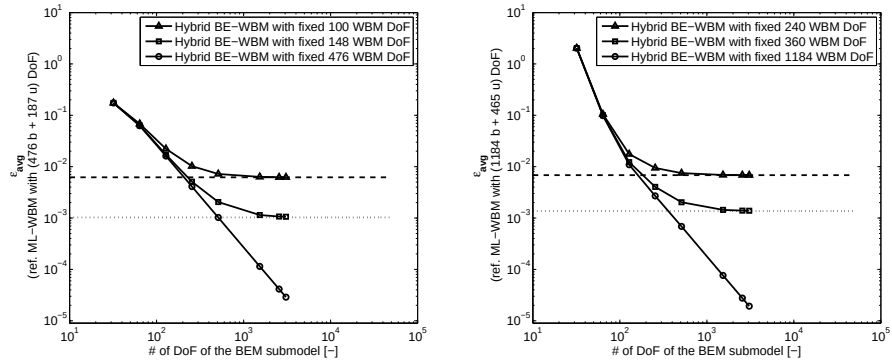

(a) 2000 Hz case. (· · ·) represents the accuracy of the full ML-WBM model, which has 148 DoF for the cavity. (- -) represents the accuracy of the full ML-WBM model, which has 100 DoF for the cavity.

(b) 5000 Hz case. (· · ·) represents the accuracy of the full ML-WBM model, which has 360 DoF for the cavity. (- -) represents the accuracy of the full ML-WBM model, which has 240 DoF for the cavity.

Figure 7.19: Convergence of the hybrid method with fixed DoF on the WBM submodel

Figures 7.20(a) and 7.20(b) show the case where the number of DoF of the BEM submodel is fixed and the number of DoF of the WBM submodel is increased. Each refinement corresponds to an integer value of truncation rule, with $T = 1 \ldots 10$. For this case, the reference is the BEM that uses linear elements. The two straight lines with dots and dashes show the limits of the BEM submodel. They are given by full BEM models that use the same element size (0.006 m and 0.003m) as the fixed submodel of the hybrid method. When the number of DoF of the WBM submodel is increased, the hybrid method

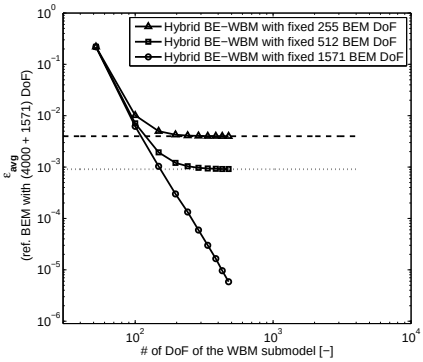

(a) 2000 Hz case. (· · ·) represents the accuracy of the full BEM model, which has 512 DoF for the circle. (--) represents the accuracy of the full BEM model, which has 255 DoF for the circle.

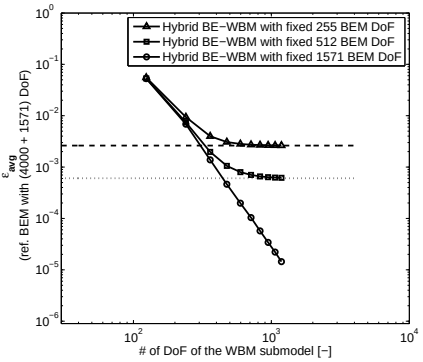

(b) 5000 Hz case. (· · ·) represents the accuracy of the full BEM model, which has 512 DoF for the circle. (--) represents the accuracy of the full BEM model, which has 255 DoF for the circle.

Figure 7.20: Convergence of the hybrid method with fixed DoF on the BEM submodel

converges to the limits for both cases of 2000 Hz and 5000 Hz. Moreover, when the BEM submodel of the hybrid BE-WBM is identical to that of the reference model's, the method keeps converging. These results demonstrate that the coupling algorithms for the BEM submodel also do not hinder the accuracy of the hybrid method.

It is also of interest to examine the pressure field given by the hybrid BE-WBM and to see how it compares against a BEM reference. The same two frequencies are investigated: 2000 Hz and 5000 Hz. Figures 7.21 and 7.22 show the amplitude of the pressure at 2000 Hz for the BEM and the hybrid BE-WBM, respectively. Figure 7.23 shows the $\log_{10}$ of the relative error for the hybrid BE-WBM, defined in equation (7.1) with the reference as the BEM model. The BEM model uses element length of 0.001 m, which results in 4000 DoF for the cavity and 1571 DoF for the circle. The finest refinement model of the convergence figures is chosen for the hybrid method, which has 476 DoF ($T = 10$) for the WBM submodel (cavity) and 1571 DoF for the BEM submodel (circle).

Figures 7.24, 7.25 and 7.26 show the same quantities for 5000 Hz. The BEM model is kept the same. The hybrid method is again chosen as the finest refinement model on the convergence figures, which has 1184 DoF ($T = 10$) for the WBM submodel (cavity) and 1571 DoF for the BEM submodel (circle). As it is clearly seen on the figures, the hybrid method gives an excellent accuracy throughout the field.

With the given contour plots of the field and convergence figures, it is demonstrated that the coupling algorithms do not lower the accuracy of the hybrid BE-WBM and the method is driven by the accuracy of the least accurate

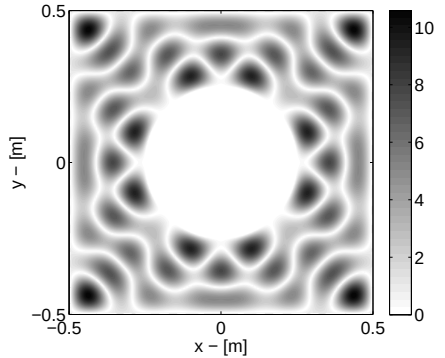

Figure 7.21: Pressure amplitude [Pa] at 2000 Hz given by the reference BEM.

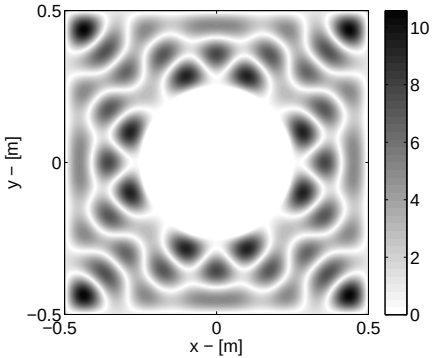

Figure 7.22: Pressure amplitude [Pa] at 2000 Hz given by the hybrid BE-WBM.

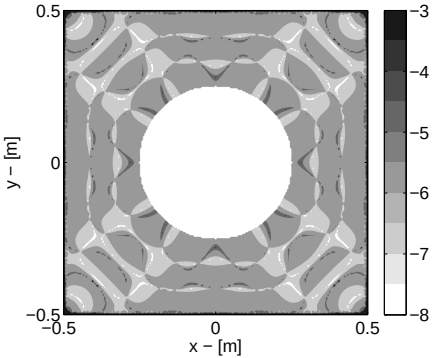

Figure 7.23: $\log_{10}(\epsilon)$ given by the hybrid BE-WBM (ref. BEM) at 2000 Hz.

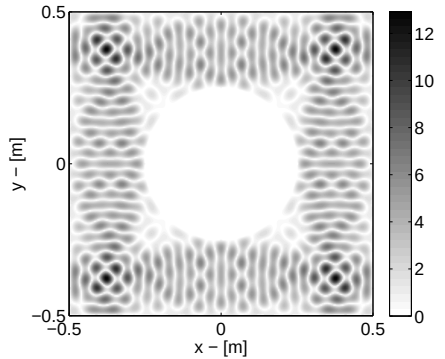

Figure 7.24: Pressure amplitude [Pa] at 5000 Hz given by the reference BEM.

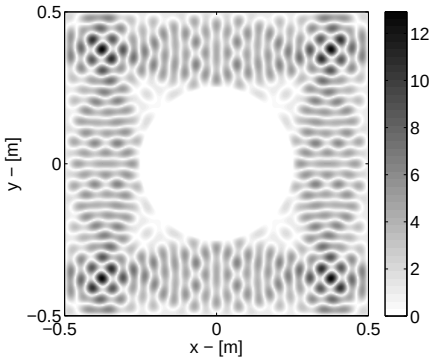

Figure 7.25: Pressure amplitude [Pa] at 5000 Hz given by the hybrid BE-WBM.

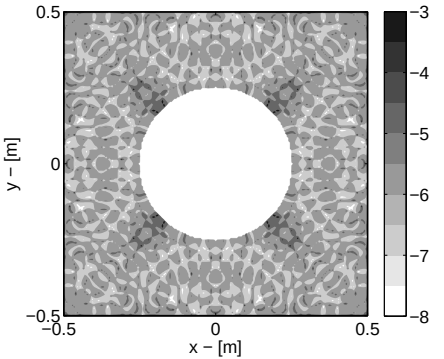

Figure 7.26: $\log_{10}(\epsilon)$ given by the hybrid BE-WBM (ref. BEM) at 5000 Hz.

of its submodels.

7.2.2 Performance assessment 1

The second verification case focuses on the convergence behavior of the method and how it compares to the FEM. The motivation is such that for bounded problems, the FEM is the state of the art and it is of interest to compare the convergence behavior of the two methods. The problem geometry is given in Figure 7.27. The cavity is a 1 m × 1 m × 1 m cube. The inclusion is a sphere with 0.25 m radius, placed at the center of the cube at the coordinate (0,0,0). All the boundaries are rigid, i.e. $\bar{v}_n = 0$. The excitation to the system is a point source placed at the coordinate (0.3,0.3,0.3) with an amplitude of 1 m^3/s.

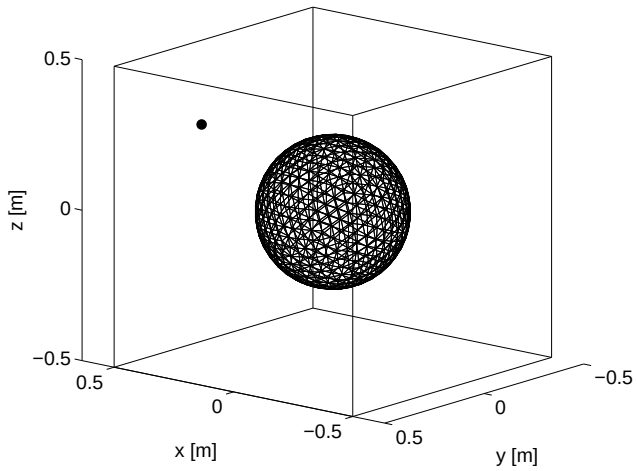

Figure 7.27: Problem geometry for the hybrid BE-WBM model. The point source (•) is located at the coordinate (0.3,0.3,0.3) and indicated with a black dot on the figure. All the boundaries are rigid ($\bar{v}_n = 0$)

It is of interest to see how the method behaves for successive refinements of the numerical models. As such, the performance of the method is evaluated with respect to its accuracy. The hybrid BE-WBM is compared to the conventional FEM for 500 Hz and 750 Hz in Figures 7.28 and 7.29. Two different element types are used for FEM models, i.e. linear tetrahedral elements and quadratic tetrahedral elements. The BEM submodel of the hybrid method uses linear triangular elements.

Equation (7.2) is used for the error criterion. The error is averaged over 42 points, which are equally distributed on a spherical surface with 0.4 m radius, placed in the center of the cavity at the coordinate (0,0,0). The corresponding numbers of DoF for the FEM and hybrid BE-WBM models are given in Tables

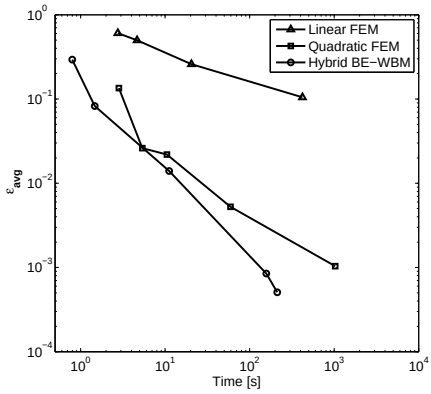

Figure 7.28: Convergence comparison of methods at 500 Hz (ref. ML-WBM with $T = 10$).

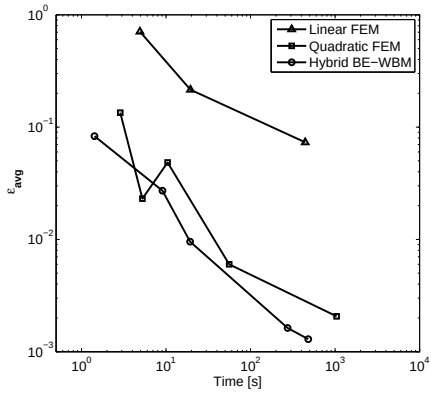

Figure 7.29: Convergence comparison of methods at 750 Hz (ref. ML-WBM with $T = 8$).

7.3 and 7.4 for 500 Hz and 750 Hz, respectively. The DoF of the hybrid method are obtained by combinations of $T = 1 \ldots 4$ for the WBM submodel and element sizes of 0.08 m, 0.04 m and 0.02 m for the BEM submodel. The reference model is the ML-WBM, which is very accurate and efficient for such a geometry [136]. For the 500 Hz case, the reference model has 5766 bounded and 625 unbounded wave functions, which corresponds to $T = 10$. For the 750 Hz case, the reference model has 8214 bounded and 900 unbounded wave functions, which corresponds to $T = 8$.

The comparisons are made in terms of CPU times. For the hybrid method, the system matrices should be built for each frequency. As such, the CPU time is assigned as the sum of system building time and system solving time. For the FEM, on the other hand, the system matrices are frequency independent. Consequently, only the system solving time is included in the CPU time. The benchmarks are run on a Linux machine with 8 Intel Xeon E5540, 2.53 GHz CPUs and 24 GB RAM. For all the models, one CPU is used to run the simulations, in order to make the comparison in a more controlled environment. However, effective parallelization is possible for both methods.

All the FEM models are calculated with Comsol 4.3 [30]. The refinements of the FEM mesh are carried out by using the standard auto-meshing property of the software, such that the refinements follow the physical problem boundary and not the boundary of the previous mesh. The efficient MUMPS direct solver is used. For the hybrid method, an in-house research code is used, which is mainly based on Matlab [96]. A Fortran function is called from the Matlab to calculate the BEM submodel, which is created with inspiration from the sample codes in [149].

Figures 7.28 and 7.29 show clearly that the hybrid method has a better convergence behavior than the linear and quadratic FEM. The linear FEM

Table 7.3: Model information for 500 Hz

	Number of DoF (nodes and/or wave functions)				
	refinement 1	refinement 2	refinement 3	refinement 4	refinement 5
Hybrid BE-WBM[a]	96 W + 162 B	294 W + 162 B	294 W + 642 B	600 W + 2562 B	1014 W + 2562 B
Quadratic FEM	6923	21762	42639	128679	506186
Linear FEM	5717	16845	65211	346350	-

[a] 'W' stands for the number of DoF of the WBM submodel and 'B' stands for the number of DoF of the BEM submodel.

Table 7.4: Model information for 750 Hz

	Number of DoF (nodes and/or wave functions)				
	refinement 1	refinement 2	refinement 3	refinement 4	refinement 5
Hybrid BE-WBM[a]	216 W + 162 B	216 W + 642 B	600 W + 642 B	1350 W + 2562 B	2166 W + 2562 B
Quadratic FEM	6923	21762	42639	128679	506186
Linear FEM	16845	65211	346350	-	-

[a] 'W' stands for the number of DoF of the WBM submodel and 'B' stands for the number of DoF of the BEM submodel.

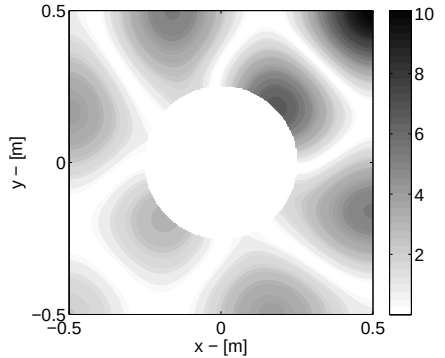

Figure 7.30: Pressure amp. [Pa] at 500 Hz given by the ML-WBM with $T = 10$.

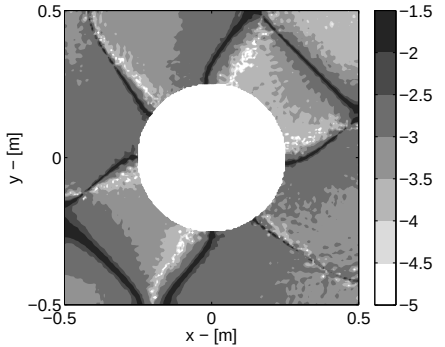

Figure 7.31: $\log_{10}(\epsilon)$ given by the quadratic FEM (ref. ML-WBM) at 500 Hz.

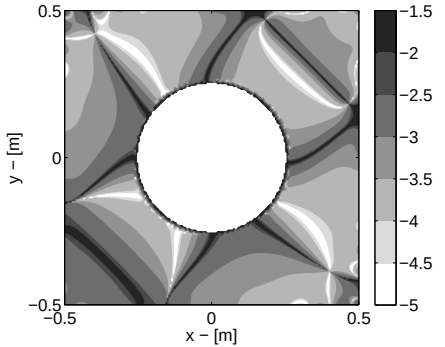

Figure 7.32: $\log_{10}(\epsilon)$ given by the hybrid BE-WBM (ref. ML-WBM) at 500 Hz.

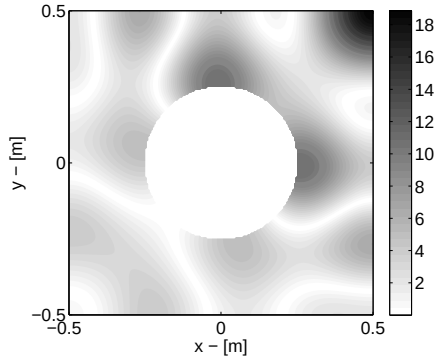

Figure 7.33: Pressure amp. [Pa] at 750 Hz given by the ML-WBM with $T = 8$.

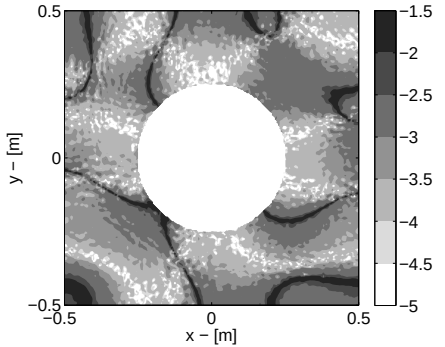

Figure 7.34: $\log_{10}(\epsilon)$ given by the quadratic FEM (ref. ML-WBM) at 750 Hz.

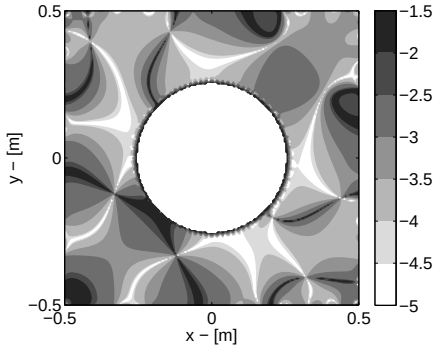

Figure 7.35: $\log_{10}(\epsilon)$ given by the hybrid BE-WBM (ref. ML-WBM) at 750 Hz.

struggles to get decent accuracy while having a heavy computational load. The quadratic FEM behaves better and shows good accuracy levels with reasonable computational time. However, when compared to the hybrid BE-WBM, it is roughly 5 times slower for its finest refinement models.

With the convergence figures presented, it is also of interest to see the error distribution on the field. Figure 7.30 shows the pressure field at 500 Hz predicted by the reference ML-WBM model. Figures 7.31 and 7.32 show $\log_{10}$ of the relative error (7.1) on the field given by the quadratic FEM and the hybrid BE-WBM, respectively. They are obtained by using the finest refinements of both methods. The figures show the x-y plane at $z = 0$. Figures 7.33, 7.34 and 7.35 show the same quantities at 750 Hz.

The error distributions on the field confirm that a good overall accuracy is obtained for both methods. It is only at the lowest pressure zones that the accuracies drop to $10^{-1.5}$. This is the case for both the FEM and the hybrid BE-WBM and is due to the fact that the relative error calculation needs division of the error to the value of the reference pressure.

7.2.3 Performance assessment 2

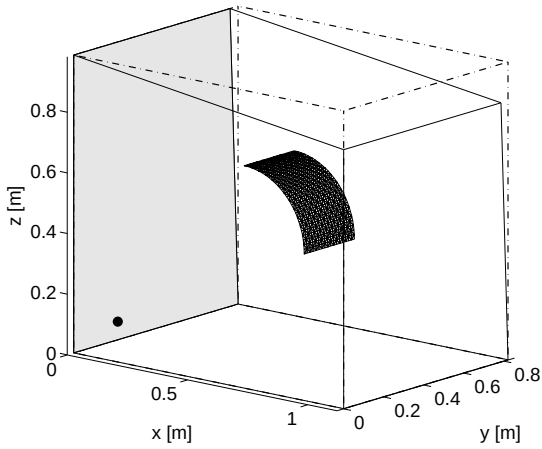

	Coordinates (m)		
	x	y	z
P1	0	0.82	0
P2	0	0.78	0.982
P3	0	0	0.982
P4	1.112	0	0.854
P5	1.112	0	0
P6	1.112	0	0
P7	1.112	0.785	0.854
P8	0	0	0

Figure 7.36: Problem geometry for the hybrid BE-WBM model is given on the left. The point source (•) is located at the coordinate (0.1,0.1,0.1). All the boundaries are rigid ($\bar{v} = 0$), except the one at $x = 0$ coordinate, which is indicated by the gray color and has an impedance value of $\bar{Z}_n = 1000$ kg/m^{2}s. The coordinates of the corners of the box is given on the right.

The third verification case aims to assess the performance of the hybrid BE-WBM over a wide frequency range and compares it to the FEM. The problem geometry is given in Figure 7.36. The cavity is a $1.122 \times 0.82 \times 0.982$ m convex box with non-parallel walls. The inclusion is a zero-thickness curved panel, which is obtained by taking a quarter of a cylinder wall. The radius of

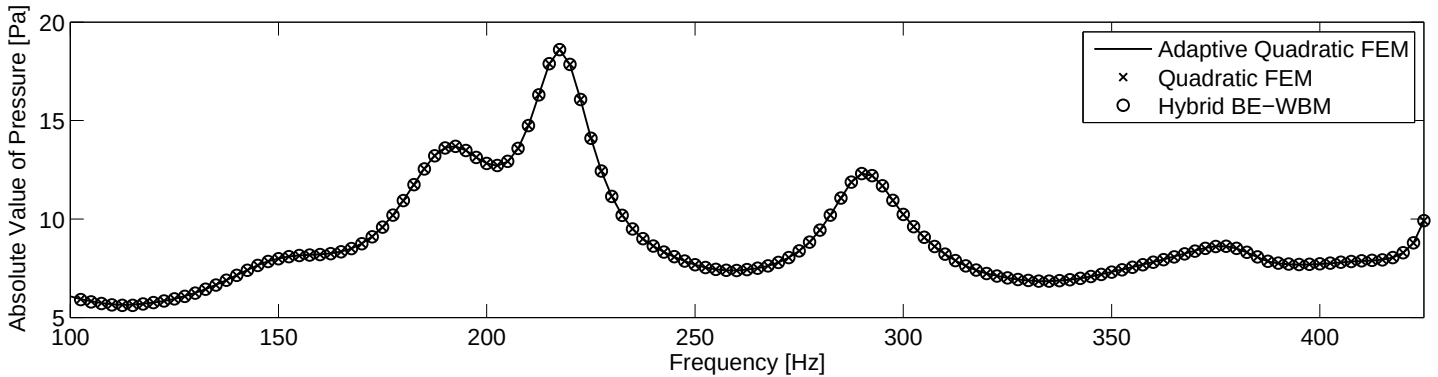

(a) Absolute value of pressure from 100 to 425 Hz

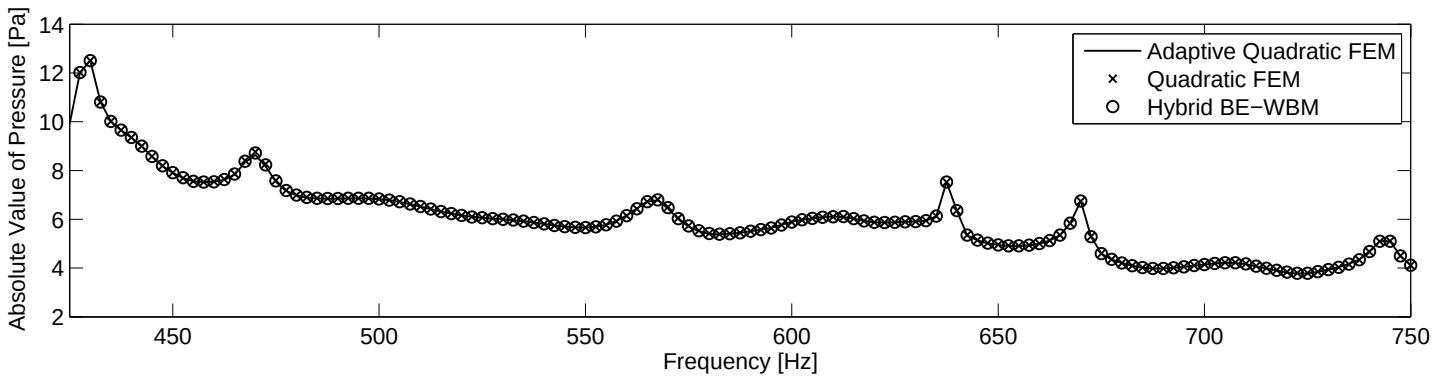

(b) Absolute value of pressure from 425 to 750 Hz

Figure 7.37: FRF comparison of methods. The frequency step is 2.5 Hz.

curvature is 0.25 m and the length of the panel in y axis is 0.25 m. The center of the cylinder, which the panel is created from, is located at the coordinate (0.5,0.375,0.4). The geometry of the cavity is based on a test box at KU Leuven, called SoundBox. More information can be found in [145, 146].

The problem geometry is chosen to demonstrate the flexibility of the hybrid BE-WBM. As such, this geometry is not feasible to model with a pure WBM or ML-WBM approach. The reason is that, decomposing the domain into convex subdomains would need a very fine discretization of the domain, which makes the WBM approaches inefficient.

All the boundaries of the problem are rigid ($\bar{v}_n = 0$), except the one at $x = 0$ coordinate, which is indicated by gray color on the figure and has an impedance value of $\bar{Z}_n = 1000$ kg/m^{2}s. The excitation is a point source placed at the coordinate (0.1,0.1,0.1), with an amplitude of 1 m^3/s.

Figure 7.37 shows the frequency response function(FRF) of the average pressure for three methods: hybrid BE-WBM, FEM with quadratic tetrahedral elements and an adaptive FEM with quadratic tetrahedral elements (as the reference). The pressure average is calculated over 42 equally distributed points on a spherical surface, with 0.4 m radius and its center located at the coordinate (0.6,0.4,0.5). The calculations are done from 100 Hz to 750 Hz, with 2.5 Hz steps.

In order to make a fair performance assessment, the accuracy of the models has to be identical. The model properties are adjusted for this purpose. The quadratic FEM model has 316037 nodes. The hybrid method has 486 DoF on the BEM submodel (element size is 0.015 m) and uses a truncation rule of $T = 3$ for the WBM submodel for all frequencies. As such, the number of DoF for the WBM submodel is between 54 and 1168 for the given frequency range. The adaptive quadratic FEM is chosen as the reference because obtaining a quality reference model by a further refinement of the regular quadratic FEM model was not feasible due to heavy computational load and huge RAM requirement. The adaptive quadratic FEM uses a h-refinement strategy and is configured to have either 20 successive refinements or a maximum number of 500000 elements. This results in an average of 964274 DoF over the whole frequency range. The FRF comparison in Figure 7.37 shows that all the methods nicely match with each other.

A more detailed look to the accuracy of the methods is given in Figure 7.38. The error is calculated for the same models and receiver points that are used to calculate the FRF curves. The relative error is calculated by using equation (7.2), with the adaptive quadratic FEM as the reference. It is apparent that the hybrid model and the quadratic FEM model have very similar accuracy, which is aimed to be around the engineering accuracy of 1 %.

It is also of interest to observe the error on the field. As such, Figure 7.39 shows the absolute value of the pressure at 500 Hz given by the adaptive quadratic FEM, while Figures 7.40 and 7.41 show the error field given by the quadratic

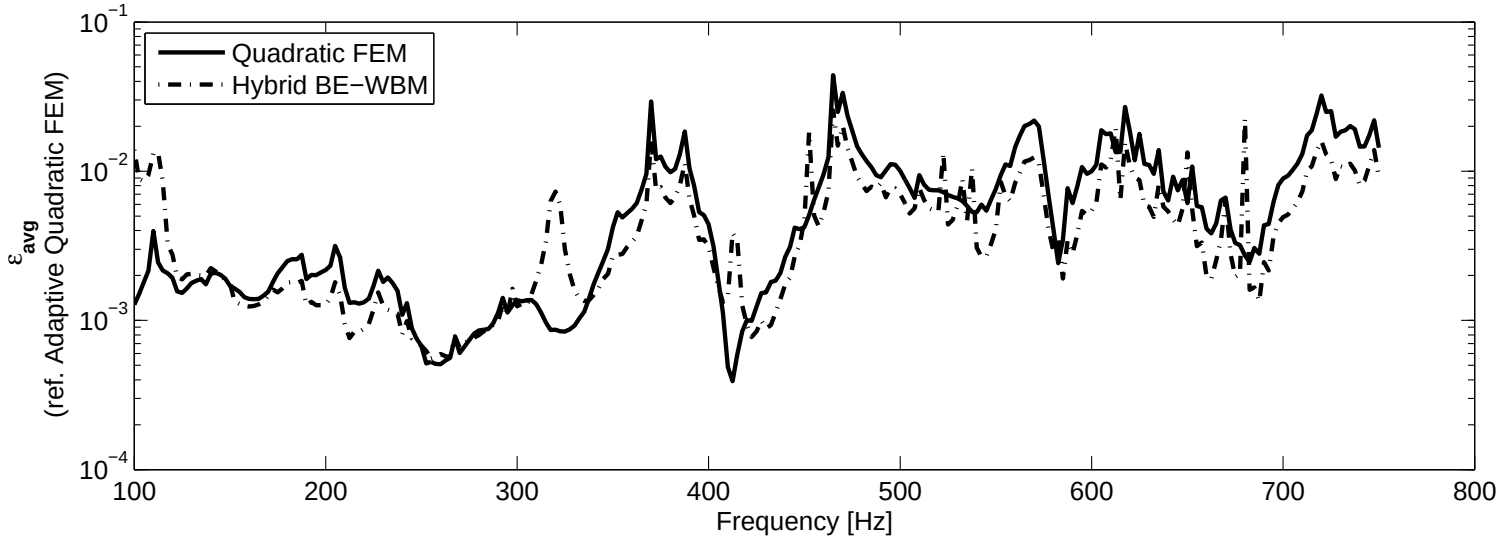

Figure 7.38: Comparison of relative error FRFs.

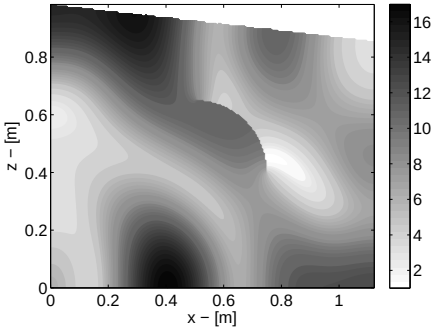

Figure 7.39: Pressure amplitude [Pa] at 500 Hz given by the adaptive quadratic FEM.

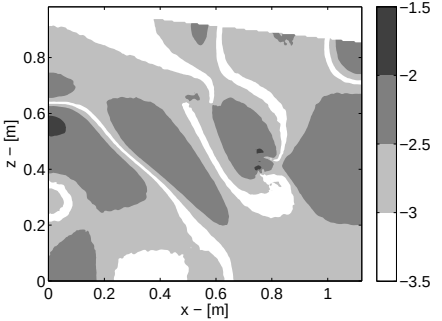

Figure 7.40: $\log_{10}(\epsilon)$ given by the quadratic FEM (ref. adaptive quadratic FEM) at 500 Hz.

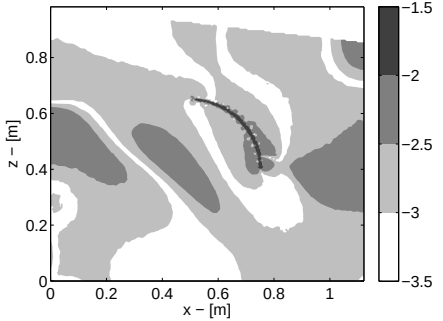

Figure 7.41: $\log_{10}(\epsilon)$ given by the hybrid BE-WBM (ref. adaptive quadratic FEM) at 500 Hz.

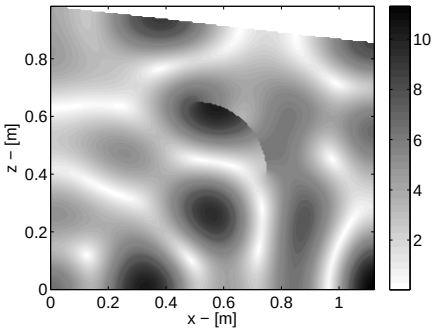

Figure 7.42: Pressure amplitude [Pa] at 750 Hz given by the adaptive quadratic FEM.

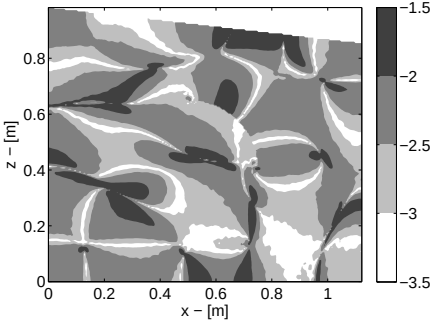

Figure 7.43: $\log_{10}(\epsilon)$ given by the quadratic FEM (ref. adaptive quadratic FEM) at 750 Hz.

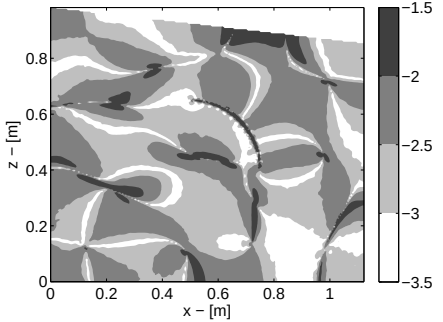

Figure 7.44: $\log_{10}(\epsilon)$ given by the hybrid BE-WBM (ref. adaptive quadratic FEM) at 750 Hz.

FEM and the hybrid BE-WBM, respectively. Equation (7.1) is used to evaluate the error, while the adaptive quadratic FEM is chosen as the reference. The contours are given for x-z plane at $y = 0.4$. Figures 7.42, 7.43 and 7.44 present the same quantities at 750 Hz. The models used for the contour figures are the same models that are used to calculate the FRF curves. The hybrid method gives a slightly better accuracy as compared to the quadratic FEM for the presented frequencies, which is in agreement with Figure 7.38.

Overall, the accuracy of the two methods is adjusted to be very similar, which allows a fair comparison of performances. Figure 7.45 presents the cumulative CPU time over the given frequency range. The benchmarks are run using the same hardware and software with the previous verification case. Once again, the CPU time for the hybrid method includes system building and system solving time, while for the FEM, it corresponds to the system solving time. The total CPU time over the whole frequency range for the quadratic FEM is approximately 29 hours and for the hybrid BE-WBM, it is approximately 1.5 hours. As such, the hybrid method is almost 20 times faster than the quadratic FEM for this verification case.

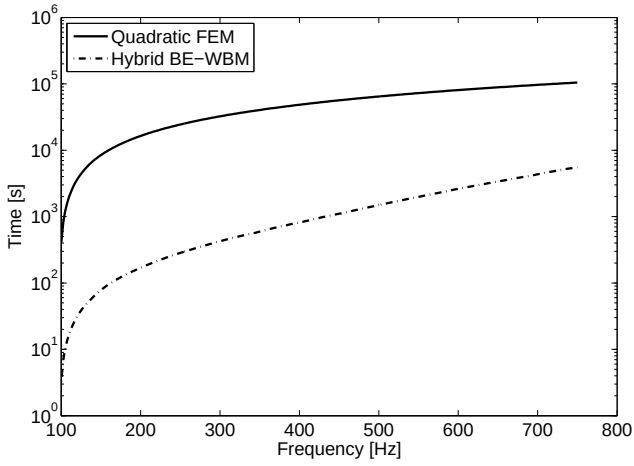

Figure 7.45: Comparison of cumulative CPU times.

7.2.4 Discussion of the results

It has been demonstrated that the hybrid BE-WBM gives high accuracy results while outperforming the FEM by almost 20 times for the last presented case.

Nevertheless, one should be cautious on interpreting the benchmark values presented in this section. The performance of the hybrid method depends on the relative size of the inclusion, as well as on the shape of the cavity. Having a very large inclusion would work in favor of the FEM, because the domain to be modeled gets smaller, while for the hybrid method, it would cost an extra

effort to model larger boundaries. Also, having a too complex cavity shape would drag the efficiency of the WBM submodel as well.

Beside the choice of the geometry, one should also note that the performance for both the FEM and the hybrid BE-WBM can be improved. The comparisons are made with an in-house code, mainly based on Matlab, for the hybrid BE-WBM and a commercial software, which uses an efficient implementation albeit a conventional version of the FEM. As such, improvements either from the methodological side (use of iterative solvers and accelerated schemes for the BEM and the FEM) or the implementation side is possible.

Keeping in mind all the above mentioned conditions, the performance figures presented here are believed to be indicative of the potential of the hybrid method, while the cases are, to a certain extend, representative of possible engineering applications.

Moreover, the advantages of the hybrid method are not only about the raw performance figures, but also about the modeling concepts it uses. Namely, the ease of refinement of the models as compared to the FEM makes the pre-processing stage more user friendly and less time consuming. In addition, the possible use of the hybrid BE-WBM in an optimization scenario would make the already good performance figures even more pronounced. To be more specific, if the position of an inclusion is to be optimized with a fixed cavity, only the coupling matrices have to be recalculated for different iteration steps. If the shape of the inclusion is to be optimized, the WBM submodel can be reused. Considering that the system building time takes a considerable percentage of the total CPU time, this relaxation would bring an extra boost for the performance of the hybrid BE-WBM for both cases.

7.3 Conclusion

Various numerical verification cases are presented in this chapter to assess the accuracy and the performance of the hybrid BE-WBM. The method is applied to inclusion and multiple scattering problems. For both problem types, 2D and 3D examples are presented. It is demonstrated that when used for the right application, the hybrid BE-WBM can be faster than the ML-WBM, the FM-BEM and the FEM. It is also demonstrated that the hybrid method is driven by the least accurate of its submodels and that the coupling algorithms do not hamper the accuracy.

For multiple scattering problems, the hybrid method is suitable when simple and complex geometries coexist. In addition, by using the ability of the WBM for modeling heterogeneities and the ability of the indirect variational BEM to model open boundaries, it is made easier for both methods to tackle a wider range of multiple scattering configurations.

For inclusion problems, the hybrid method becomes advantageous when there is

a moderately complex cavity with complex inclusions. As such, the efficiency of the WBM can be utilized for a wider range of bounded problem configurations.

Chapter 8

Conclusions and Future Work

The effect of sound on living quality is significant. Good acoustic properties are not considered luxurious for commercial products anymore, but necessary. Therefore, designers and engineers have made acoustic design an integral part of the product cycle. As the computational resources become ever more powerful, the acoustic design process, together with the other engineering and design decisions shift more and more to the virtual environment. Consequently, the need for good CAE tools is higher than ever.

An ideal numerical method for acoustic problems should provide accurate results with high efficiency and should be applicable over the full audible range. However, no mature method has accomplished these goals yet. Instead, the current methods show their strengths for specific frequency regions. For low frequencies, element based methods are the most commonly used and for high frequencies, Statistical Energy Analysis (SEA) and geometrical acoustic methods such as image source and ray tracing methods are common. While these methods are established for their target frequency ranges, they fail to adequately address the mid-frequency range, which holds a critical role on human perception. As it is indicated by the short survey of the state-of-the-art in Chapter 2, there is still demand for alternative methods to bridge the mid-frequency gap.

The Wave Based Method [38] has been developed to remedy this problem and provide an alternative to element based methods. The WBM is a deterministic method, which uses an expansion of *a priori* defined functions that exactly satisfy the governing equation to predict the field variables. As such, it belongs to the family of Trefftz approaches. The advantages of the WBM over conventional element based methods are that it has a small model size, a high convergence rate and does not introduce pollution errors in its representation of the primary field variable because of its basis function set. A sufficient

condition for the WBM to converge is the convexity of the problem domain or that the domain is divided into convex subdomains. The WBM shows its full efficiency for a small number of large subdomains. Therefore, it is more suitable for problems with moderately complex geometry. This requirement limits the WBM's practical applicability. As such, the method has not yet fulfilled its full potential.

There have been improvements to the WBM over the years in order to relax the geometrical requirements of the method. The Finite Element Method (FEM) has been coupled to the WBM for acoustic cavities that have fine details on the boundary [137]. For such problems, the WBM is used to create simple, large subdomains surrounded by the FEM mesh that handles the geometrical details. This way, the efficiency of the WBM is utilized together with the flexibility of the FEM. Apart from the hybrid Finite Element - Wave Based Method (FE-WBM), a method called the Multi-level WBM (ML-WBM) [133] has been developed to relax the geometrical requirements and make the WBM modeling framework more efficient for inclusion and multiple scattering problems. The ML-WBM divides the problem domain into 'levels' and allows the scatterers/inclusions in those levels to be modeled as if they are separate problems. A superposition principle is used to couple the levels while writing the weighted residual formulation and the resulting system of equations is solved at once. In the case of multiple scatterers, this leads to the use of individual truncation circles/spheres instead of one global truncation boundary and saves a great modeling effort. The same is true for inclusion problems, as the bounded domain can be modeled as if there is no inclusion and the inclusion can be modeled as if it is in free space.

The hybrid FE-WBM and the ML-WBM indeed extended the range of applications where the efficiency of the WBM can be exploited. Nevertheless, there are still problem settings where they can be inadequate. For instance, when the shape of an inclusion or scatterer is complex, the ML-WBM struggles because within the individual truncation circle/sphere, the convexity requirement of the WBM still applies. The hybrid FE-WBM also struggles, because the use of the FEM for inclusions leads to further partitioning of the bounded domains.

By considering the aforementioned advantages and shortcomings of the WBM and its extensions, a dual research goal is persued for the presented dissertation:

Assessment and enhancement of the WBM and the ML-WBM There are numerous practical applications where the WBM can be used efficiently, especially with its recent Multi-level extension. When it is used for the right application, the method outperforms the element based methods in computational efficiency and brings various practical advantages. As such, the first goal of this dissertation was to assess the advantages of the available WBM technologies and enhance them within their own framework.

Relaxing the geometrical requirements of the WBM While the hybrid FE-WBM and the ML-WBM are successful in their target applications, they fail to efficiently address bounded problems with complex inclusions or multiple scattering problems with geometrically complex scatterers. As such, the second goal of this dissertation was to develop new techniques that extend the practical applicability of the WBM.

8.1 Summary of the research and outcomes

8.1.1 Application of the WBM on a room acoustics case

The WBM is applied on a L-shaped room in Chapter 3 to assess the efficiency of the WBM for large-size problems in the mid-frequency range. The performance of the method is compared to the Fast Multipole Boundary Element Method's (FM-BEM). In addition, the WBM's accuracy is compared with measurements and a hybrid ray tracing method. For the FM-BEM simulations, LMS Virtual Lab is used and for the ray tracing method, ODEON software is used. For the WBM, an in-house C++/Fortran implementation is used. Necessary formulations to convert the surface absorption coefficients used in ray tracing methods to normal impedance values used in the WBM are presented.

The performance comparison of the WBM and the FM-BEM reveals the efficiency of the WBM in the mid-frequency range. The WBM is shown to be more than 6 times faster than the FM-BEM for the problem at hand. [1]

The WBM results are also compared with measurements and ray tracing results. In order to correctly capture the wave field, sound absorption should be added to the WBM model. This is done by making the speed of sound complex. The FM-BEM results are not included in the comparison, because the Virtual Lab implementation does not allow for a complex speed of sound. The WBM predicts the overall energy level (spatial average of the pressure over 11 receiver points) of the measurements within 2 dB. For mid-frequency results (the 250 Hz and 500 Hz octave bands), the ray tracing and the WBM results are very similar; both of them predict the overall energy levels within 0.5 dB as compared to measurements. An unexpected result is obtained at the 125 Hz octave band, where the WBM predicts the wave field worse than the ray tracing method. Comparison with various other deterministic methods shows that all the tested methods give very similar results. Therefore, the problem is expected to be at the core deterministic modeling of the system. The acoustical properties of the interior surfaces are estimated so that the corresponding reverberation time matches the ray tracing results to the measured reverberation time. This approach may have introduced an artificial correction to the ray tracing results in the lower frequencies. The 1 kHz octave band results were slightly in favor of the ray tracing method too. At this frequency range, it is shown that the

[1] These performance figures were obtained while the WBM used 1 processor and the FM-BEM used up to 8 processors.

effect of air absorption can be as high as 7 dB. A constant air absorption was chosen for the whole octave band. As such, a variable absorption value can make the WBM results more accurate.

To sum up, the WBM is shown to be a competitive mid-frequency method for a large-size problem of moderate complexity. This holds for both performance comparison with the FM-BEM and accuracy comparison with measurements and a ray tracing method. Possible sources of errors for the discrepancies between measurements, the ray tracing results and the WBM results for the 125 Hz and 1 kHz band are highlighted. The effect of air absorption at high frequencies is emphasized.

8.1.2 The Multi-level Wave Based Method

Chapter 4 starts with a review of the ML-WBM for multiple scattering problems, where the steps needed to make the WBM fit into the multilevel framework are presented. After the brief review of the method, symmetric boundary conditions are derived for 2D and 3D problems. The symmetry conditions defined in this chapter are based on the geometrical symmetry of the scatterers relative to a certain axis/plane. For such problems, using symmetric boundary conditions reduces the computational cost considerably. For 2D problems, the system building time is halved. The system solution time is even more reduced because the size of the system matrix is reduced from $N \times N$ to $N/2 \times N/2$, where N is the number of unknowns. For 3D problems, the system building time is reduced to one-fourth, if the problem is symmetric in two axes. Accordingly, the system matrix size is reduced to $N/4 \times N/4$. As such, this chapter extended the range of problems that the ML-WBM can address efficiently.

8.1.3 Optimization of acoustic lenses using the ML-WBM

The ML-WBM is applied on optimization of acoustic lenses in Chapter 5. The considered acoustic lenses are used to focus an incoming plane wave to a desired point at a given frequency and composed of a large number of scatterers. As such, it makes a good application case to demonstrate the capabilities of the ML-WBM. While there is an emphasis on the numerical modeling aspect of the acoustic lenses, there is also a focus on the results of the optimizations, as they have led to innovations in acoustic lens designs.

Three main innovations are presented for acoustic lens designs. The first part of the chapter proposes a new design procedure for acoustic lenses, where the shape of the unit scatterer is optimized together with the lattice parameters. The shape design is based on optimizing the aperture of circular arcs. An interesting outcome is that some designs resulted in highly open unit scatterers that look like satellite dishes. This is a surprising result, because in recent popular articles, acoustic lenses have been based on closed scatterers or

scatterers with small apertures. As such, the focusing effect has been explained by considering the volumetric filling fraction of the scatterers [21, 61, 72, 126]. It is observed that, for highly open scatterers, this value is irrelevant. A more general explanation for the physics of the focusing effect is provided by referencing the works in [3, 80]. The second part of the chapter focuses on a design procedure based on creating vacancies on predefined grids of scatterers. This design procedure was proposed by Håkansson *et al.* [66]. So far, this procedure has been applied on lenses that are based on rigid cylinders. As the second innovation in this chapter, the use of Helmholtz resonators as unit scatterers is proposed. This is applied on 2D problems first. By comparing the optimization results for lenses based on cylinders and lenses based on Helmholtz resonators, it is demonstrated that the use of Helmholtz resonators brings a big advantage. This is true especially for low frequencies, where the Helmholtz resonators utilize their local resonances. As the third innovation, the optimization cases are extended to 3D problems. The key aspect here is that the designs are executed directly in 3D space, as opposed to similar works in literature where the designs are executed in 2D space and rotated in z axis to retrieve 3D results. Spheres are used as unit scatterers first. Subsequently, cup shaped scatterers are used that act as Helmholtz resonators. It is shown that the lenses based on cup shaped scatterers are able to provide the same focusing power by occupying only one-fourth of the space that the spheres based lenses occupy. An important point is the comparison of these lenses with the ones in literature. For the same frequency and focal length, the presented lenses reveal slightly lower focusing power as compared to the ones in [114], i.e. 10.9 dB vs. 13.25 dB. However, the lenses based on cup shapes have 0.39 m width and height, while the lens presented in [114] has 1.165 m diameter. The choice depends on the priorities: space limitations vs. the desired focusing power. In the end, the lenses presented here become alternatives to the ones in literature as compact acoustic lenses.

As for the numerical modeling aspect of acoustic lens designs, the benefits of using the ML-WBM are demonstrated. Symmetric boundary conditions that are derived in Chapter 4 are used to model acoustic lenses with a large number of scatterers. For 3D problems, acoustic lenses with up to 1526 spherical scatterers are modeled with 3456 unknowns or less. In addition to the small model size, an even more important property of the ML-WBM is emphasized. The ML-WBM only requires the full model to be built once for the optimization problems, which are based on creating vacancies on the predefined grids. For each iteration, only a subset of the full matrix is solved. This property makes the already attractive performance figures of the ML-WBM even more pronounced.

To conclude, this chapter presents optimization of acoustic lenses using the ML-WBM with an emphasis on the benefits of the method. In addition, innovations are proposed for the application subject itself.

8.1.4 Hybrid Boundary Element - Wave Based Method

A novel hybrid method is proposed in Chapter 6, where the WBM is coupled to the Boundary Element Method (BEM). The hybrid Boundary Element - Wave Based Method (BE-WBM) targets two specific problem settings: multiple scattering problems where simple and complex scatterers co-exist and inclusion problems where the bounded domain has moderate complexity and the inclusions are geometrically complex. For both of these settings, current extensions to the WBM, i.e. the hybrid FE-WBM and the ML-WBM, fail to provide an efficient solution. For element based methods, the complexity of the scatterers/inclusions does not have (in general) a direct effect on the computational performance. However, as demonstrated in Chapter 7, their computational costs are high. With the hybrid BE-WBM, it is possible to address these problems with high efficiency.

In addition to the computational advantage the hybrid BE-WBM brings, it also provides key conceptual advantages to the aforementioned problem settings. The hybrid BE-WBM has an easier refinement procedure as compared to the FEM. The refinement of the WBM submodel only requires an increased number of wave functions, without further partitioning the domain. The BEM submodel needs a refined mesh of the problem boundary as compared to a refined mesh of the problem domain, which is the case for the FEM. Another key conceptual advantage of the hybrid BE-WBM is regarding optimization problems, i.e. it allows the reuse of the fixed parts of the problem. For instance, in a scenario where the position of an inclusion is to be optimized, the hybrid BE-WBM only needs the recalculation of the coupling matrices. On the other hand, the FEM would need the remeshing of the whole domain for each iteration, which hampers the practical applicability of the FEM to such problems.

To sum up, coupling of the WBM and the BEM is proposed for the efficient solution of inclusion and multiple scattering problems. For certain optimization problems, its intrinsic properties makes it a highly competitive alternative to the state-of-the-art methods.

8.1.5 Hybrid BE-WBM: numerical verifications

Chapter 7 presents numerical verifications for the hybrid BE-WBM. The accuracy of the coupling algorithms is assessed while the performance of the method is benchmarked against the ML-WBM, the BEM, the FM-BEM and the FEM. In total, six numerical verification cases are presented, where the first three of them are multiple scattering problems and the remaining three are inclusion problems. The cases comprise both 2D and 3D settings.

It is demonstrated that the coupling algorithms do not introduce extra error and the hybrid method converges to the limits given by its least accurate submodel. The method's efficiency is compared with the BEM's and the ML-

WBM's for a 2D problem that is composed of a simple and a complex scatterer. It is shown that the hybrid BE-WBM outperforms both for the presented case by being twice as fast. A similar setting for a 3D case is also presented where it is shown that the hybrid method is around six times faster than the FM-BEM for the presented case.

For inclusion problems, the benchmarks are carried out against the FEM. It is shown that the convergence rate of the hybrid BE-WBM is higher than both a linear and a quadratic FEM for a problem that consists of a cubic box and a sphere inside. In another example, a box with non-parallel walls is considered, which has a curved panel inside. For this case, the hybrid BE-WBM performs 20 times faster than a quadratic FEM.

An important note here is that the aforementioned calculation times should not be considered as definitive figures but as indications of the computational performance. This is because there might be improvements from methodological side and from implementation side to all the tested methods. On the other hand, it should be noted that widely used commercial packages are considered for the FM-BEM and the FEM simulations, i.e. LMS Virtual Lab and Comsol, while the hybrid method is based on a dedicated Matlab/Fortran routine.

To conclude, the presented cases demonstrate that the hybrid BE-WBM is capable of providing accurate and fast results and the method has a high potential as an alternative to element based methods.

8.2 Future research topics

The presented work concentrates on two research goals: application and improvements of the current WBM technologies, and development of new methods to relax geometrical requirements of the WBM. For both of them, major contributions are made as detailed in the previous section. These contributions pave the wave for new research topics, which are listed as the subject of future research below.

8.2.1 Application of the WBM and its extensions

It is demonstrated that the ML-WBM is a strong numerical tool with inherent advantages for the optimization of acoustic lenses. The presented cases are the first ones to explore this application field for the ML-WBM. In light of the results of this work, it is of interest to consider the following topics in the future:

Use of residue theorem for optimization over a wide frequency range
D'Amico *et al.* [31] suggested the use of the residue theorem for the efficient evaluation of band-averaged input power. The same principles presented there

can be applied to acoustic lens design, where the objective function can be modified to obtain results over a wide frequency range, rather than a single frequency. The benefit of using the residue theorem in this context is that, by running a single simulation at a complex frequency, the band-averaged values can be obtained which would save a great computational effort.

Experiments on acoustic lenses It is of interest to build physical realizations of the resulting acoustic lens designs and compare the numerical simulations with measurements. Håkansson *et al.* [66] showed that the numerical simulations of their optimized lenses (which are based on rigid cylinders) agreed well with measurements. However, the effect of using the Helmholtz resonators as unit scatterers is still to be investigated.

A combined shape optimization and vacancy optimization procedure for acoustic lenses In Chapter 5, two distinct optimization procedures are used to design acoustic lenses. The first one optimized the shape of the unit scatterer and lattice parameters. The second one optimized the overall topology by creating vacancies on predefined grids. A possible improvement can be achieved by combining these two procedures in one. The search space for the shape optimization can be limited to couple of discrete steps to relax on computational costs. The condition of existence for a certain scatterer can be added to this search space. This way, the designs can have more freedom and may lead to better results.

Optimization of acoustic barriers All the principles for designing acoustic lenses can be applied to design acoustic barriers. The possible use of residue theorem would make it easier to design acoustic barriers for a wide frequency range. Romero-García *et al.* [110] demonstrated that the vacancy optimization can be used to create wide band gaps. The addition of local resonances by using the Helmholtz resonators would bring a big advantage, especially at low frequencies, where the band gap creation is limited.

Including structural vibrations in numerical modeling of sonic crystals All the acoustic lenses presented in this work are considered rigid. On the other hand, the structural vibrations may play an important role, if the wall thickness of the Helmholtz resonators is small. Desmet [38] proposed the appropriate wave function sets for coupled vibro-acoustic simulations of circular shell sections. The structural resonances might be exploited in the design procedure to create multi-resonant metamaterials as presented in [111].

8.2.2 Relaxing the geometrical requirements of the WBM

A hybrid BE-WBM is proposed to further relax the geometrical requirements of the WBM. There are possible improvements that can be applied to this new approach, while it is also of interest to exploit its inherent advantages in optimization problems.

Further development of the hybrid BE-WBM: touching boundaries The current implementation of the hybrid BE-WBM prohibits the boundaries of the WBM and BEM submodels to touch each other. This stems from the (hyper-) singular operator of the BEM part. For the core BEM formulation, it is possible to use a transformation through Stoke's formula and change the kernel operator to a weakly singular operator [67]. However, that transformation is not suitable for the coupling operator. The coupling operator resembles Burton-Miller formulations and different techniques should be implemented. Implementing a modified integration rule as detailed in [124] or the use of singularity subtraction technique are possibilities [106].

Application of the hybrid BE-WBM in optimization settings As it is discussed before, the intrinsic properties of the hybrid BE-WBM make it a powerful tool for optimization problems. Finding the optimal positions of sound screens in a room to create silent compartments can be an interesting practice. This can be used in open office designs. The same procedure can be used to design a classroom, where the sound screens can be of help to distribute the speaker's voice more homogeneously over the audience area. A final example is the design of loudspeakers. The position of stiffeners inside the loudspeaker cabins can be optimized to reduce the back coupling of the cavity to the cone. As such, the frequency response of the loudspeaker would be more flat.

Investigations on coupling of the FM-BEM and the WBM The FM-BEM speeds up the BEM solution considerably, especially for large-size problems. Incorporating this enhancement into the hybrid scheme would reveal increased performance for the hybrid method. However, further investigations are needed to assess the feasibility of this coupling. In particular, the FM-BEM yields a fast matrix-vector product and requires an iterative solver, whereas the WBM requires a direct solver due to ill-conditioning.

Experiments for validating the hybrid BE-WBM It is of interest to validate the hybrid BE-WBM results with experiments. A research project that started in KU Leuven Physics Department investigates how visually impaired people use sound to perceive their surroundings. A measurement campaign will start, where inclusions with various shapes are placed in front of a dummy human head in a room. The hybrid BE-WBM is well suited for this problem and a comparison of numerical results with measurements would be an interesting

study. In addition, experiments with SoundBox [145] can be used for validations as well.

Appendix A

Compact lenses based on spheres

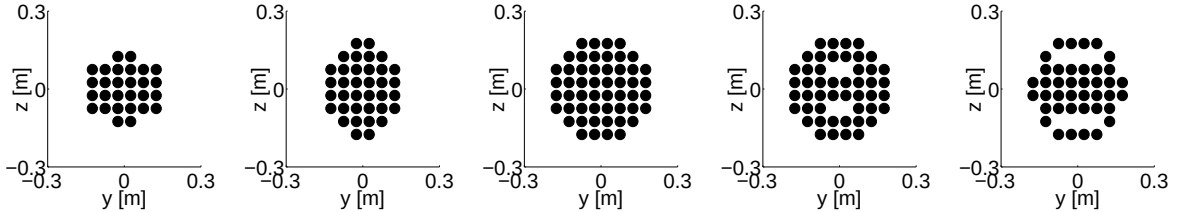

(a) x = -0.20 m (b) x = -0.15 m (c) x = -0.10 m (d) x = -0.05 m (e) x = 0 m

Figure A.1: The design results showing the topology of the lens optimized for 2200 Hz and 0.5 m. Each subfigure corresponds to one layer of the lens at the given x coordinate.

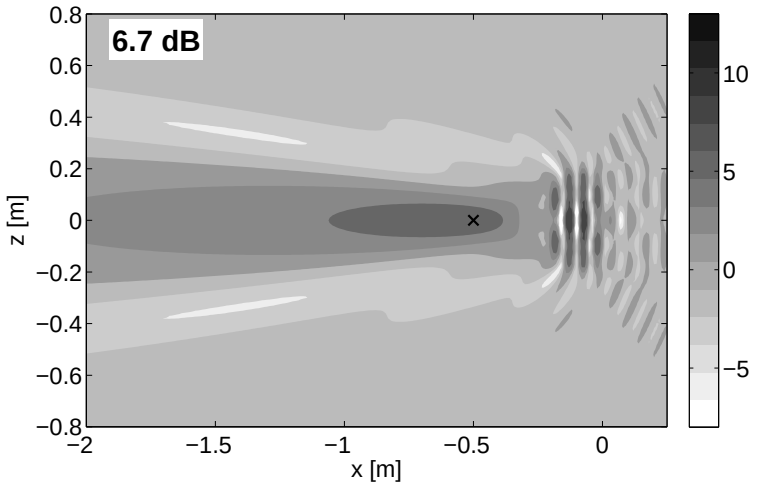

Figure A.2: The acoustic pressure field given in normalized SPL value - [dB]. The field is generated by the lens optimized for 2200 Hz and 0.5 m. The x marker shows the location of the focal point.

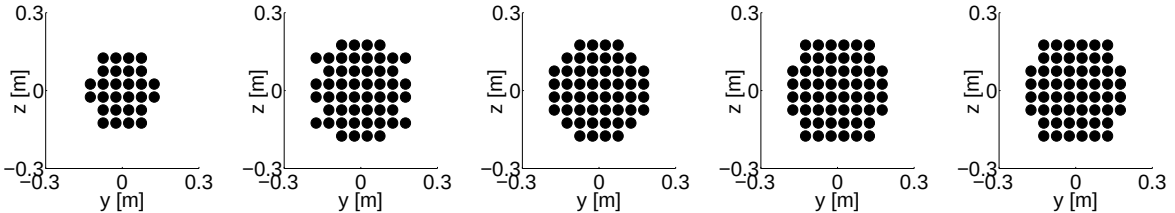

(a) x = -0.20 m (b) x = -0.15 m (c) x = -0.10 m (d) x = -0.05 m (e) x = 0 m

Figure A.3: The design results showing the topology of the lens optimized for 2500 Hz and 0.5 m. Each subfigure corresponds to one layer of the lens at the given x coordinate.

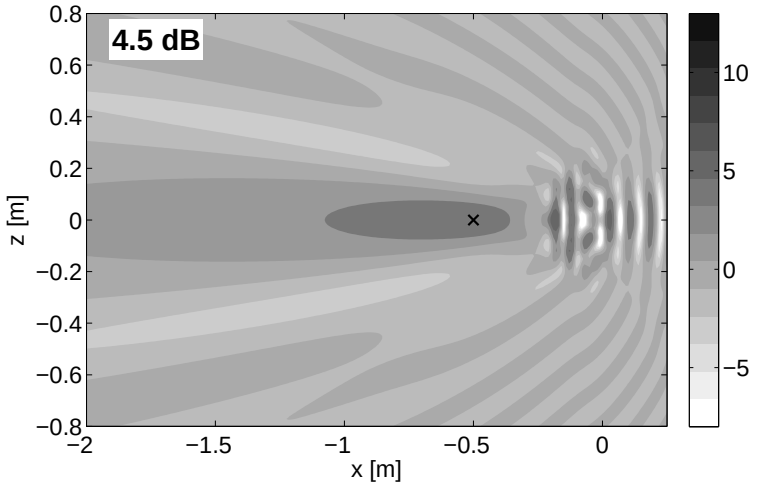

Figure A.4: The acoustic pressure field given in normalized SPL value - [dB]. The field is generated by the lens optimized for 2500 Hz and 0.5 m. The x marker shows the location of the focal point.

Bibliography

[1] Abramowitz, M., and Stegun, I. *Handbook of mathematical functions*, 9th ed. Dover, New York, 1972. pages

[2] Airaksinen, T., Heikkola, E., Pennanen, A., and Toivanen, J. An algebraic multigrid based shifted-laplacian preconditioner for the helmholtz equation. *Journal of Computational Physics 226*, 1 (2007), 1196 – 1210. pages

[3] Amram, M., and Stern, R. Refractive and other acoustic effects produced by a prism-shaped network of rigid strips. *The Journal of the Acoustical Society of America 70*, 5 (1981), 1463–1472. pages 13

[4] Aretz, M. *Combined Wave And Ray Based Room Acoustic Simulations Of Small Rooms*. RWTH Aachen University, Institute of Technical Acoustics, PhD. thesis D 82, 2012. pages 4

[5] Atak, O., Bergen, B., Huybrechs, D., Pluymers, B., and Desmet, W. Coupling of boundary element and wave based methods for the efficient solution of complex multiple scattering problems. *Journal of Computational Physics 258*, 0 (2014), 165 – 184. pages

[6] Avery, P., Farhat, C., and Reese, G. Fast frequency sweep computations using a multi-point Padé-based reconstruction method and an efficient iterative solver. *International Journal for Numerical Methods in Engineering 69*, 13 (2007), 2848 – 2875. pages

[7] Babuška, I., and Sauter, S. Is the Pollution Effect of the FEM Avoidable for the Helmholtz Equation Considering High Wave Numbers? *SIAM Review 42*, 3 (2000), 451–484. pages 4

[8] Barnett, A., and Betcke, T. Stability and convergence of the method of fundamental solutions for helmholtz problems on analytic domains. *Journal of Computational Physics 227*, 14 (2008), 7003–7026. pages

[9] Bebendorf, M. *Hierarchical Matrices: A Means to Efficiently Solve Elliptic Boundary Value Problems*. Springer, 2008. pages

[10] Benzi, M. Preconditioning techniques for large linear systems: A survey. *J. Comput. Phys. 182*, 2 (Nov. 2002), 418–477. pages

[11] Bergen, B. *Wave based modelling techniques for unbounded acoustic problems*. KULeuven, division PMA, PhD. thesis 2011D07, 2011. pages 6

[12] Bergen, B., Pluymers, B., Van Genechten, B., Vandepitte, D., and Desmet, W. A trefftz based method for solving helmholtz problems in semi-infinite domains. *Engineering Analysis with Boundary Elements 36*, 1 (2012), 30–38. pages

[13] Bergen, B., Van Genechten, B., Vandepitte, D., and Desmet, W. An Efficient Trefftz-Based Method for Three-Dimensional Helmholtz Problems in Unbounded Domains. *Computer Modeling in Engineering & Sciences 61*, 2 (2010), 155–175. pages

[14] Bériot, H., Perrey-Debain, E., Tahar, M. B., and Vayssade, C. Plane wave basis in galerkin {BEM} for bidimensional wave scattering. *Engineering Analysis with Boundary Elements 34*, 2 (2010), 130 – 143. pages

[15] Bonnet, M., Maier, G., and Polizzotto, C. Symmetric Galerkin Boundary Element Methods. *Applied Mechanics Reviews 51* (1998), 669. pages

[16] Bork, I. A comparison of room simulation software - The 2nd Round Robin on room acoustical computer simulation. *Acustica/Acta Acustica 86* (2000), 943–956. pages

[17] Bouillard, P., and Ihlenburg, F. Error estimation and adaptivity for the Finite Element Method in acoustics: 2D and 3D applications. *Computer Methods in Applied Mechanics and Engineering 176* (1999), 147–163. pages 4, 5

[18] Brebbia, C., Telles, J., and Wrobel, L. *Boundary Element Techniques: Theory and Applications in Engineering*. Springer-Verlag, 1984. pages

[19] Brunner, D., Junge, M., Rapp, P., Bebendorf, M., and Gaul, L. Comparison of the fast multipole method with hierarchical matrices for the helmholtz-bem. *Computer Modeling in Engineering & Sciences(CMES) 58*, 2 (2010), 131–160. pages

[20] Burton, A., and Miller, G. The Application of Integral Equation Methods to the Numerical Solution of Some Exterior Boundary-Value Problems. *Proceedings of the Royal Society of London. A. Mathematical and Physical Sciences 323*, 1553 (1971), 201–210. pages

[21] Cervera, F., Sanchis, L., Sánchez-Pérez, J. V., Mártinez-Sala, R., Rubio, C., Meseguer, F., López, C., Caballero, D., and

Sánchez-Dehesa, J. Refractive acoustic devices for airborne sound. *Phys. Rev. Lett. 88* (Dec 2001), 023902. pages 13

[22] Cessenat, O., and Després, B. Using Plane Waves as Base Functions for Solving Time Harmonic Equations with the Ultra Weak Variational Formulation. *Journal of Computational Acoustics 11*, 02 (2003), 227–238. pages 4

[23] Chandler-Wilde, S. N., Graham, I. G., Langdon, S., and Spence, E. A. Numerical-asymptotic boundary integral methods in high-frequency acoustic scattering. *Acta Numerica 21* (5 2012), 89–305. pages 4

[24] Chen, W. Symmetric boundary knot method. *Engineering Analysis with Boundary Elements 26* (2002), 489–494. pages

[25] Chen, Y.-Y., and Ye, Z. Acoustic attenuation by two-dimensional arrays of rigid cylinders. *Phys. Rev. Lett. 87* (Oct 2001), 184301. pages

[26] Cheng, C., Seybert, A., and Wu, T. A multidomain boundary element solution for silencer and muffler performance prediction. *Journal of Sound and Vibration 151*, 1 (1991), 119–129. pages

[27] Christensen, C. A new scattering that combines roughness and diffraction effects. In *Proceedings of Forum Acusticum* (Budapest, Hundary, 2005). pages

[28] Claeys, C. C., Vergote, K., Sas, P., and Desmet, W. On the potential of tuned resonators to obtain low-frequency vibrational stop bands in periodic panels. *J. Sound. Vib. 332*, 6 (2013), 1418 – 1436. pages

[29] Climente, Alfonso and Torrent, Daniel and Sánchez-Dehesa, José. Sound focusing by gradient index sonic lenses. *Applied Physics Letters 97*, 10 (2010), 104103. pages

[30] Comsol Multiphysics. *version 4.3*. Comsol, Inc., 2012. pages

[31] D'Amico, R., Koo, K., Huybrechs, D., and Desmet, W. On the use of the residue theorem for the efficient evaluation of band-averaged input power into linear second-order dynamic systems. *Journal of Sound and Vibration 332*, 26 (2013), 7205 – 7225. pages 15

[32] D'Amico, R., Pratellesi, A., Pierini, M., and Tournour, M. Efficient method to avoid fictitious eigenvalues for indirect BEM. In *Proceedings of the International Conference on Noise and Vibration Engineering ISMA 2010* (Leuven, Belgium, September 20–22 2010), pp. 4505–4519. pages

[33] Deckers, E., Atak, O., Coox, L., D'Amico, R., Devriendt, H., Jonckheere, S., Koo, K., Pluymers, B., Vandepitte, D., and Desmet, W. The wave based method: An overview of 15 years of research. *Wave Motion*, 0 (2013), –. pages

[34] Deckers, E., Drofmans, B., Van Genechten, B., Bergen, B., Vandepitte, D., and Desmet, W. Spline-based boundaries: a first step towards generic geometric domain descriptions for efficient mid-frequency acoustic anaylsis using the wave based method. *Journal of Computational and Applied Mathematics 235* (2011), 2679–2693. pages

[35] Deckers, E., Hörlin, N.-E., Vandepitte, D., and Desmet, W. A wave based method for the efficient solution of the 2d poroelastic biot equations. *Computer Methods in Applied Mechanics and Engineering 201-204* (2012), 245–262. pages

[36] Deckers, E., Van Genechten, B., Vandepitte, D., and Desmet, W. Efficient treatment of stress singularities in poroelastic wave based models using special purpose enrichment functions. *Computer and Structures 89* (2011), 1117–1130. pages

[37] Deckers, E., Vandepitte, D., and Desmet, W. A wave based method for the axisymmetric dynamic analysis of acoustic and poroelastic problems. *Computer Methods in Applied Mechanics and Engineering 257*, 0 (2013), 1–16. pages

[38] Desmet, W. *A wave based prediction technique for coupled vibro-acoustic analysis.* KULeuven, division PMA, PhD. thesis 98D12, 1998. pages 4, 5, 9, 16

[39] Elman, H. C., Ernst, O. G., and O'Leary, D. P. A multigrid method enhanced by krylov subspace iteration for discrete helmholtz equations. *SIAM J. Sci. Comput. 23*, 4 (Apr. 2001), 1291–1315. pages

[40] Erlangga, Y. Advances in iterative methods and preconditioners for the helmholtz equation. *Archives of Computational Methods in Engineering 15*, 1 (2008), 37–66. pages 4

[41] Erlangga, Y., Vuik, C., and Oosterlee, C. On a class of preconditioners for solving the helmholtz equation. *Applied Numerical Mathematics 50*, 3Ű4 (2004), 409 – 425. pages

[42] Erlangga, Y., Vuik, C., and Oosterlee, C. Comparison of multigrid and incomplete {LU} shifted-laplace preconditioners for the inhomogeneous helmholtz equation. *Applied Numerical Mathematics 56*, 5 (2006), 648 – 666. pages

[43] Fairweather, G., and A. Karageorghis, P. M. The method of fundamental solutions for scattering and radiation problems. *Engineering Analysis with Boundary Elements 27* (2003), 759–769. pages

[44] Farhat, C., Antonini, M., and Radek, T. FETI-H: a scalable domain decomposition method for high frequency exterior Helmholtz problems. *Domain Decomposition Methods in Sciences and Engineering* (1999), 228–238. pages

[45] Farhat, C., Avery, P., Tezaur, R., and Li, J. Feti-dph: A dual-primal domain decomposition method for acoustic scattering. *Journal of Computational Acoustics 13*, 03 (2005), 499–524. pages

[46] Farhat, C., Harari, I., and Franca, L. P. The discontinuous enrichment method. *Computer Methods in Applied Mechanics and Engineering 190*, 48 (2001), 6455–6479. pages 4

[47] Farhat, C., Harari, I., and Hetmaniuk, U. A discontinuous Galerkin method with Lagrange multipliers for the solution of Helmholtz problems in the mid-frequency regime . *Computer Methods in Applied Mechanics and Engineering 192*, 11Ű12 (2003), 1389–1419. pages 4

[48] Farhat, C., Macedo, A., Lesoinne, M., Roux, F.-X., Magoulès, F., and de La Bourdonnaie, A. Two-level domain decomposition methods with Lagrange multipliers for the fast iterative solution of acoustic scattering problems. *Computer Methods in Applied Mechanics and Engineering 184*, 2Ű4 (2000), 213–239. pages 4

[49] Farhat, C., and Roux, F.-X. A method of finite element tearing and interconnecting and its parallel solution algorithm. *International Journal for Numerical Methods in Engineering 32*, 6 (1991), 1205–1227. pages

[50] Farhat, C., Tezaur, R., and Weidemann-Goiran, P. Higher-order extensions of a discontinuous galerkin method for mid-frequency helmholtz problems. *International Journal for Numerical Methods in Engineering 61*, 11 (2004), 1938–1956. pages

[51] Fischer, M., Gauger, U., and Gaul, L. A multipole galerkin boundary element method for acoustics. *Engineering Analysis with Boundary Elements 28*, 2 (2004), 155–162. pages 4

[52] Freymann, R. *Advanced numerical and experimental methods in the field of vehicle structural-acoustics*. Hieronymus Buchreproduktions GmbH, 2000. pages

[53] Funkhouser, T., Tsingos, N., Carlbom, I., Elko, G., Sondhi, M., West, J. E., Pingali, G., Min, P., and Ngan, A. A beam tracing method for interactive architectural acoustics. *The Journal of the Acoustical Society of America 115*, 2 (2004), 739–756. pages

[54] Gibbs, B. M., and Jones, D. K. A Simple Image Method for Calculating the Distribution of Sound Pressure Levels within an Enclosure. *Acta Acustica united with Acustica 26*, 1 (1972), 24–32. pages 3

[55] Givoli, D. Recent advances in the DtN FE method. *Archives of Computational Methods in Engineering 6*, 2 (1999), 71–116. pages

[56] Godinho, L., and Tadeu, A. Acoustic analysis of heterogeneous domains coupling the {BEM} with kansa's method. *Engineering Analysis with Boundary Elements 36*, 6 (2012), 1014 – 1026. pages

[57] Greengard, L., Huang, J., Rokhlin, V., and Wandzura, S. Accelerating fast multipole methods for the helmholtz equation at low frequencies. *Computational Science Engineering, IEEE 5*, 3 (1998), 32–38. pages

[58] Greengard, L., and Rokhlin, V. A fast algorithm for particle simulations. *Journal of Computational Physics 73*, 2 (1987), 325–348. pages 4

[59] Grote, M., and Kirsch, C. Dirichlet-to-neumann boundary conditions for multiple scattering problems. *Journal of Computational Physics 201* (2004), 630–650. pages

[60] Guenneau, S., Movchan, A., Pétursson, G., and Ramakrishna, S. A. Acoustic metamaterials for sound focusing and confinement. *New Journal of Physics 9*, 11 (2007), 399. pages

[61] Gupta, B. C., and Ye, Z. Theoretical analysis of the focusing of acoustic waves by two-dimensional sonic crystals. *Phys. Rev. E 67* (Mar 2003), 036603. pages 13

[62] Håkansson, A., Cervera, F., and Sánchez-Dehesa, J. Sound focusing by flat acoustic lenses without negative refraction. *Applied Physics Letters 86*, 5 (2005), –. pages

[63] Håkansson, A., and Sánchez-Dehesa, J. Optimal design of microscaled scattering optical elements. *Applied Physics Letters 87*, 19 (Nov 2005), 193506–193506–3. pages

[64] Håkansson, A., Sánchez-Dehesa, J., and Cervera, F. Experimental realization of sonic demultiplexing devices based on inverse designed scattering acoustic elements. *Applied Physics Letters 88*, 16 (2006), –. pages

[65] Håkansson, A., Sánchez-Dehesa, J., Cervera, F., Meseguer, F., Sanchis, L., and Llinares, J. Comment on "theory of tailoring sonic devices: Diffraction dominates over refraction". *Phys. Rev. E 71* (Jan 2005), 018601. pages

[66] Håkansson, A., Sánchez-Dehesa, J., and Sanchis, L. Acoustic lens design by genetic algorithms. *Phys. Rev. B 70* (Dec 2004), 214302. pages 13, 16

[67] Hamdi, M., and Ville, J. Sound radiations from ducts: Theory and experiment. *Journal of Sound and Vibration 107*, 2 (1986), 231–242. pages 17

[68] Harari, I. A survey of finite element methods for time-harmonic acoustics. *Computer Methods in Applied Mechanics and Engineering 195* (2006), 1594–1607. pages

[69] Harari, I., and Avraham, D. High-Order Finite Element Methods for Acoustic Problems. *Journal of Computational Acoustics 05*, 01 (1997), 33–51. pages 4

[70] Harari, I., and Turkel, E. Accurate finite difference methods for time-harmonic wave propagation. *Journal of Computational Physics 119*, 2 (1995), 252 – 270. pages

[71] Herrera, I. *Boundary Methods: an Algebraic Theory*. Pitman Adv. Publ. Program, London, 1984. pages

[72] Hu, X., Chan, C. T., and Zi, J. Two-dimensional sonic crystals with helmholtz resonators. *Phys. Rev. E 71* (May 2005), 055601. pages 13

[73] Huttunen, T., Gamallo, P., and Astley, R. Comparison of two wave element methods for the Helmholtz problem. *Communications in Numerical Methods in Engeneering 25* (2009), 35–52. pages

[74] Huybrechs, D., and Vandewalle, S. An efficient implementation of boundary element methods for computationally expansive green's functions. *Engineering Analysis with Boundary Elements 32* (2008), 621–632. pages

[75] Ihlenburg, F. *Finite Element Analysis of Acoustic Scattering*. Springer-Verlag, 1998. pages

[76] Jonckheere, S., Deckers, E., Genechten, B. V., Vandepitte, D., and Desmet, W. A direct hybrid Finite Element Ű Wave Based Method for the steady-state analysis of acoustic cavities with poro-elastic damping layers using the coupled Helmholtz-Biot equations. *Computer Methods in Applied Mechanics and Engineering 263*, 0 (2013), 144–157. pages

[77] Kansa, E. MultiquadricsŮa scattered data approximation scheme with applications to computational fluid-dynamicsŮii solutions to parabolic, hyperbolic and elliptic partial differential equations. *Computers & Mathematics with Applications 19*, 8Ű9 (1990), 147 – 161. pages

[78] Kechroud, R., Soulaimani, A., Saad, Y., and Gowda, S. Preconditioning techniques for the solution of the helmholtz equation by the finite element method. *Mathematics and Computers in Simulation 65*, 4Ű5 (2004), 303 – 321. <ce:title>Wave Phenomena in Physics and Engineering: New Models, Algorithms, and Applications</ce:title>. pages

[79] Kita, E., and Kamiya, N. Trefftz method: an overview. *Advances in Engineering Software 24*, 13 (1995), 3 – 12. pages

[80] Kock, W. E., and Harvey, F. K. Refracting sound waves. *The Journal of the Acoustical Society of America 21*, 5 (1949), 471–481. pages 13

[81] Koopmann, G. H., Song, L., and Fahnline, J. B. A method for computing acoustic fields based on the principle of wave superposition. *Journal of Acoustic Society of America 86* (1989), 2433–2438. pages

[82] Kovalevsky, L., Ladevèze, P., and Riou, H. The fourier version of the variational theory of complex rays for medium-frequency acoustics. *Computer Methods in Applied Mechanics and Engineering 225Ű228*, 0 (2012), 142 – 153. pages

[83] Kuo, C.-H., and Ye, Z. Sonic crystal lenses that obey the lensmaker's formula. *Journal of Physics D: Applied Physics 37*, 15 (2004), 2155. pages

[84] Kushwaha, M. S. Stop-bands for periodic metallic rods: Sculptures that can filter the noise. *Applied Physics Letters 70*, 24 (1997), 3218–3220. pages

[85] Lamb, H. 6 ed. Cambridge University Press, 1975, ch. 4, pp. 77–85. pages

[86] Langer, U., and Steinbach, O. Boundary element tearing and interconnecting methods. *Computing 71* (2003), 205–228. pages

[87] Lenzi, M. S., Lefteriu, S., Beriot, H., and Desmet, W. A fast frequency sweep approach using padé approximations for solving helmholtz finite element models. *Journal of Sound and Vibration 332*, 8 (2013), 1897 – 1917. pages

[88] Lisa, M., Rindel, J., and Christensen, C. Predicting the Acoustics of Ancient Open-Air Theatres: The Importance of Calculation Methods and Geometrical Details. In *Proceedings of the Joint Baltic-Nordic Acoustics Meeting* (2004). pages

[89] Liu, Z., Zhang, X., Mao, Y., Zhu, Y. Y., Yang, Z., Chan, C. T., and Sheng, P. Locally resonant sonic materials. *Science 289*, 5485 (2000), 1734–1736. pages

[90] Lyon, R., and DeJong, R. *Theory and application of statistical energy analysis*, 2nd ed. Butterworth-Heinemann, Boston *et al.*, 1995. pages 3

[91] Maksimov, D. N., and Tanner, G. A hybrid approach for predicting the distribution of vibro-acoustic energy in complex built-up structures. *The Journal of the Acoustical Society of America 130*, 3 (2011), 1337–1347. pages 4

[92] Marburg, S. Six boundary elements per wavelength: is that enough? *Journal of Computational Acoustics 10* (2002), 25–51. pages

[93] Marburg, S., and Schneider, S. Performance of iterative solvers for acoustic problems. part i. solvers and effect of diagonal preconditioning. *Engineering Analysis with Boundary Elements 27*, 7 (2003), 727 – 750. pages

[94] Martin, Theodore P. and Nicholas, Michael and Orris, Gregory J. and Cai, Liang-Wu and Torrent, Daniel and Sánchez-Dehesa, José. Sonic gradient index lens for aqueous applications. *Applied Physics Letters 97*, 11 (2010), 113503. pages

[95] Martínez-Sala, R., Rubio, C., García-Raffi, L. M., Sánchez-Pérez, J. V., Sánchez-Pérez, E. A., and Llinares, J. Control of noise by trees arranged like sonic crystals. *Journal of Sound and Vibration 291*, 1Ű2 (2006), 100 – 106. pages

[96] MATLAB. *version 7.10.0 (R2010a)*. The MathWorks Inc., Natick, Massachusetts, 2010. pages

[97] Melenk, J., and BabuŽka, I. The partition of unity finite element method: Basic theory and applications. *Computer Methods in Applied Mechanics and Engineering 139*, 1Ű4 (1996), 289 – 314. pages

[98] Ochmann, M. The full-field equations for acoustic radiation and scattering. *Journal of Acoustic Society of America 105*, 5 (1999), 2574–2584. pages

[99] Pechstein, C. *Finite and Boundary Element Tearing and Interconnecting Solvers for Multiscale Problems*. Springer, 2012. pages

[100] Perrey-Debain, E., Trevelyan, J., and Bettess, P. Wave boundary elements: a theoretical overview presenting applications in scattering of short waves. *Engineering Analysis with Boundary Elements 28* (2004), 131–141. pages

[101] Petyt, M., Koopmann, G., and Pinnington, R. The acoustic modes of a rectangular cavity containing a rigid, incomplete partition. *Journal of Sound and Vibration 53*, 1 (1977), 71 – 82. pages

[102] Pierce, A. *Acoustics: An Introduction to Its Physical Principles and Applications*. McGraw-Hill series in mechanical engineering, McGraw-Hill, 1981. pages

[103] Pluymers, B., Desmet, W., Vandepitte, D., and Sas, P. Application of an efficient wave based prediction technique for the analysis of vibro-acoustic radiation problems. *Journal of Computational and Applied Mathematics 168* (2004), 353–365. pages

[104] Pluymers, B., Desmet, W., Vandepitte, D., and Sas, P. On the Use of a Wave Based Prediction Technique for Steady-State Structural-Acoustic Radiation Analysis. *Journal of Computer Modeling in Engineering & Sciences 7*, 2 (2005), 173–184. pages

[105] Pluymers, B., Van Hal, B., Vandepitte, D., and Desmet, W. Trefftz-based methods for time-harmonic acoustics. *Archives of Computational Methods in Engineering 14* (2007), 343–381. pages 4

[106] Polimeridis, A., Järvenpää, S., Ylä-Oijala, P., Gray, L., Kiminki, S., and Mosig, J. On the evaluation of hyper-singular double normal derivative kernels in surface integral equation methods. *Engineering Analysis with Boundary Elements 37*, 2 (2013), 205 – 210. pages 17

[107] Rachowicz, W., Pardo, D., and Demkowicz, L. Fully automatic hp-adaptivity in three dimensions. *Computer Methods in Applied Mechanics and Engineering 195*, 37Ű40 (2006), 4816–4842. pages 4

[108] Ragnarsson, P., Pluymers, B., Donders, S., and Desmet, W. Subcomponent modelling of input parameters for statistical energy analysis by using a wave-based boundary condition. *Journal of Sound and Vibration 329*, 1 (2010), 96 – 108. pages 4

[109] Riou, H., Ladeveze, P., and Sourcis, B. The multiscale vtcr approach applied to acoustics problems. *Journal of Computational Acoustics 16*, 04 (2008), 487–505. pages

[110] Romero-García, V., Fuster, E., Garcia-Raffi, L. M., Sánchez-Pérez, E. A., Sopena, M., Llinares, J., and Sánchez-Pérez, J. V. Band gap creation using quasiordered structures based on sonic crystals. *Applied Physics Letters 88*, 17 (2006), 174104. pages 16

[111] Romero-García, V., Krynkin, A., Garcia-Raffi, L., Umnova, O., and Sánchez-Pérez, J. Multi-resonant scatterers in sonic crystals: Locally multi-resonant acoustic metamaterial. *Journal of Sound and Vibration 332*, 1 (2013), 184 – 198. pages 16

[112] Sakuma, T., and Yasuda, Y. Fast multipole boundary element method for large-scale steady-state sound field analysis. part i: Setup and validation. *Acta Acustica united with Acustica 88*, 4 (2002), 513–525. pages

[113] Sánchez-Pérez, J. V., Caballero, D., Mártinez-Sala, R., Rubio, C., Sánchez-Dehesa, J., Meseguer, F., Llinares, J., and Gálvez, F. Sound attenuation by a two-dimensional array of rigid cylinders. *Phys. Rev. Lett. 80* (Jun 1998), 5325–5328. pages

[114] Sanchis, L., Yánez, A., Galindo, P. L., Pizarro, J., and Pastor, J. M. Three-dimensional acoustic lenses with axial symmetry. *Applied Physics Letters 97*, 5 (2010), 054103. pages 13

[115] Schenck, H. Improved integral formulation for acoustic radiation problems. *The Journal of the Acoustical Society of America 44*, 1 (1968), 41–58. pages

[116] Singer, I., and Turkel, E. A perfectly matched layer for the helmholtz equation in a semi-infinite strip. *Journal of Computational Physics 201*, 2 (2004), 439 – 465. pages

[117] Software, O. R. A. *v.9.0.* ODEON A/S, Denmark, 2007. pages

[118] Steinbach, O., and Windisch, M. Stable boundary element domain decomposition methods for the helmholtz equation. *Numerische Mathematik 118*, 1 (2011), 171–195. pages

[119] Strouboulis, T., Babuška, I., and Copss, K. The design and analysis of the generalized finite element method. *Computer Methods in Applied Mechanics and Engineering 181*, 1-3 (2000), 43 – 69. pages

[120] Strouboulis, T., Babuška, I., and Hidajat, R. The generalized finite element method for helmholtz equation: Theory, computation, and open problems. *Computer Methods in Applied Mechanics and Engineering 195*, 37-40 (2006), 4711 – 4731. John H. Argyris Memorial Issue. Part I. pages

[121] Strouboulis, T., Hidajat, R., and Babuška, I. The generalized finite element method for helmholtz equation. part ii: Effect of choice of handbook functions, error due to absorbing boundary conditions and its assessment. *Computer Methods in Applied Mechanics and Engineering 197*, 5 (2008), 364 – 380. Enriched Simulation Methods and Related Topics. pages

[122] Tadeu, A., António, J., and Castro, I. Coupling the bem/tbem and the mfs for the numerical simulation of acoustic wave propagation. *Engineering Analysis with Boundary Elements 34* (2010), 405–416. pages

[123] Tezaur, R., Zhang, L., and Farhat, C. A discontinuous enrichment method for capturing evanescent waves in multiscale fluid and fluid/solid problems. *Computer Methods in Applied Mechanics and Engineering 197*, 19Ű20 (2008), 1680 – 1698. pages

[124] Theotokoglou, E., and Tsamasphyros, G. A modified gauss quadrature formula with special integration points for evaluation of quasi-singular integrals. *Engineering Analysis with Boundary Elements 30*, 9 (2006), 758 – 766. pages 17

[125] Thompson, L. A review of finite element methods for time-harmonic acoustics. *Journal of the Acoustical Society of America 119* (2006), 1315–1330. pages

[126] Torrent, D., and Sánchez-Dehesa, J. Acoustic metamaterials for new two-dimensional sonic devices. *New Journal of Physics 9*, 9 (2007), 323. pages 13

[127] Trefftz, E. Ein Gegenstück zum Ritzschen Verfahren. In *Second International Congress on Applied Mechanics* (Zurich, Switserland, 1926), pp. 131–137. pages 4

[128] Twersky, V. Multiple scattering of radiation by an arbitrary configuration of parallel cylinders. *The Journal of the Acoustical Society of America 24*, 1 (1952). pages

[129] Valente, F., and Pina, H. Iterative solvers for {BEM} algebraic systems of equations. *Engineering Analysis with Boundary Elements 22*, 2 (1998), 117 – 124. pages

[130] Valente, F., and Pina, H. Iterative techniques for 3-d boundary element method systems of equations. *Engineering Analysis with Boundary Elements 25*, 6 (2001), 423 – 429. pages

[131] Valente, F., and Pina, H. Conjugate gradient methods for three-dimensional {BEM} systems of equations. *Engineering Analysis with Boundary Elements 30*, 6 (2006), 441 – 449. pages

[132] Van Genechten, B., Atak, O., Bergen, B., Deckers, E., Jonckheere, S., Lee, J., Maressa, A., Vergote, K., Pluymers, B., Vandepitte, D., and Desmet, W. An efficient wave based method for solving helmholtz problems in three-dimensional bounded domains. *Engineering Analysis with Boundary Elements 36*, 1 (2012), 63–75. pages

[133] Van Genechten, B., Bergen, B., Vandepitte, D., and Desmet, W. A Trefftz-based numerical modelling framework for Helmholtz problems with complex multiple-scatterer configurations. *Journal of Computational Physics 229* (2009), 6623–6643. pages 6, 10

[134] Van Genechten, B., Pluymers, B., Vandepitte, D., and Desmet, W. A Hybrid Wave Based - Modally Reduced Finite Element Method for the Efficient Analysis of Low- and Mid-frequency Car Cavity Acoustics. *SAE International Journal of Passenger Cars - Mechanical Systems 2*, 1 (2009), 1494–1504. pages

[135] Van Genechten, B., Vandepitte, D., and Desmet, W. A direct hybrid Finite Element - Wave Based modelling technique for efficient coupled vibro-acoustic analysis. *Computer Methods in Applied Mechanics and Engineering 200*, 5-8 (2011), 742–764. pages

[136] Van Genechten, B., Vergote, K., Vandepitte, D., and Desmet, W. A Multi-Level Wave Based numerical modelling framework for the steady-state dynamic analysis of bounded Helmholtz problems with multiple inclusions. *Computer Methods in Applied Mechanics and Engineering 199*, 29-32 (2010), 1881–1905. pages 6

[137] Van Hal, B., Desmet, W., and Vandepitte, D. Hybrid finite element - wave based method for acoustic problems. *Computer Assisted Mechanics and Engineering Sciences 10*, 4 (2003), 375–390. pages 6, 10

[138] Vanmaele, C., Vandepitte, D., and Desmet, W. An efficient wave based prediction technique for plate bending vibrations. *Computer Methods in Applied Mechanics and Engineering 196*, 33Ű34 (2007), 3178–3189. pages

[139] Vanmaele, C., Vergote, K., Vandepitte, D., and Desmet, W. Simulation of in-plane vibrations of 2d structural solids with singularities

using an efficient wave based prediction technique. *Computer Assisted Mechanics and Engineering Sciences 19* (2012), 135–171. pages

[140] Varah, J. A practical examination of some numerical methods for linear discrete ill-posed problems. *SIAM Review 21* (1979), 100–111. pages

[141] Varah, J. Pitfalls in the numerical solution of linear ill-posed problems. *SIAM Journal on Scientific and Statistical Computing 4* (1983), 164–176. pages

[142] Vergote, K. *Dynamic analysis of structural components in the mid frequency range using the wave based method: Non-determinism and inhomogeneities*. KULeuven, division PMA, PhD. thesis 2012D03, 2012. pages

[143] Vergote, K., Vanmaele, C., Vandepitte, D., and Desmet, W. An efficient wave based approach for the time-harmonic vibration analysis of 3D plate assemblies . *Journal of Sound and Vibration 332*, 8 (2013), 1930–1946. pages

[144] Vermeir, G., and Mees, P. Sound propagation in enclosed spaces. In *In Proceedings of Internoise* (Newport Beach, CA, USA, 1995), pp. 335–338. pages 3

[145] Vivolo, M., Jonckheere, S., Pluymers, B., Vandepitte, D., and Desmet, W. Broadband sound absorption measurements by means of a small cabin. *submitted to Journal of the Acoustical Society of America* (2013). pages 18

[146] Vivolo, M., Pluymers, B., Van Genechten, B., Vandepitte, D., and Desmet, W. Study of the vibro-acoustic behaviour of composite sandwich structures by means of a novel test setup. In *International Conference on Noise and Vibration Engineering (ISMA2012)* (Leuven, Belgium, September 2012). pages

[147] Vorländer, M. International round robin room acoustical computer simulations. In *In Proceedings of the 15th International Congress on Acoustics* (Trondheim, Norway, 1995), pp. 689–692. pages

[148] Wadbro, E., Udawalpola, R., and Berggren, M. Shape and topology optimization of an acoustic hornâĂŞlens combination. *Journal of Computational and Applied Mathematics 234*, 6 (2010), 1781–1787. pages

[149] Wu, T. *Boundary Element Acoustics, Fundamentals and Computer Codes*. WIT Press, 2000. pages 2

[150] Yang, S., Page, J. H., Liu, Z., Cowan, M. L., Chan, C. T., and Sheng, P. Focusing of sound in a 3d phononic crystal. *Phys. Rev. Lett. 93* (Jul 2004), 024301. pages

[151] Zeng, X., Christensen, C., and Rindel, J. Practical methods to define scattering coefficients in a room acoustics computer model. *Applied Acoustics 67*, 8 (2006), 771–786. pages

[152] Zieliński, A. P., and Herrera, I. Trefftz method: fitting boundary conditions. *International Journal on Numerical Methods in Engineering 24* (1987), 871–891. pages

[153] Zienkiewicz, O., and Taylor, R. *The Finite Element Method - The three volume set (6th ed.)*. Butterworth-Heinemann, 2005. pages 2

Curriculum Vitae

Personal Data

Onur Atak
°7 July 1984 in Ankara, Turkey

Education

2009–2014: Ph.D. at the Department of Mechanical Engineering, Katholieke Universiteit Leuven (Belgium).

Title: *"Wave Based Modeling Methods for Acoustic Inclusion and Multiple Scattering Problems in the Mid-Frequency Range"*.

Funded by:

- –Marie Curie ITN project 214909 "MID-FREQUENCY - CAE Methodologies for Mid-Frequency Analysis in Vibration and Acoustics" supported by the European Commission (2009–2012).
- –The Fund for Scientific Research - Flanders (F.W.O) (2012–2013).
- –IWT O&O ASTRA *"Advanced STRuctural Acoustics for lightweight structures and advanced materials"* supported by the Institute for the Promotion of Innoviation through Science and Technology in Flanders (IWT-Vlaanderen) (2013–2014).

2007–2009: M.Sc. in Sound and Vibration, Chalmers University of Technology, Gothenburg (Sweden).

Master thesis: *"Evaluation of Boundary Element Method as a Tool in Analysis of Acoustical Performance of Absorber and Screen Systems in Engine Bays"*.

2003–2007: Bachelor in Mechanical Engineering, METU-Middle East Technical University, Ankara (Turkey).

List of Publications

Articles in refereed journals

[1] Atak, O., Jonckheere, S., Deckers, E., Huybrechs, D., Pluymers, B., Desmet, W. A hybrid Boundary Element-Wave Based Method for the efficient solution of bounded acoustic problems with inclusions. In review *in Computer Methods in Applied Mechanics and Engineering* (2014).

[2] Atak, O., Bergen, B., Huybrechs, D., Pluymers, B., Desmet, W. The design of three-dimensional acoustic lenses by using the Multi-level Wave Based Method. In review *in Journal of Sound and Vibration* (2014).

[3] Deckers, E., Atak, O., Coox, L., D'Amico, R., Devriendt, H., Jonckheere, S., Ku, K., Pluymers, B., Vandepitte, D., Desmet, W. The Wave Based Method: an overview of 15 years of research. *Wave Motion, 51, 550-565.* (2014).

[4] Atak, O., Huybrechs, D., Pluymers, B., Desmet, W. The design of Helmholtz resonator based acoustic lenses by using the symmetric Multi-Level Wave Based Method and genetic algorithms. *Journal of Sound and Vibration, 333(15), 3367-3381* (2014).

[5] Atak, O., Bergen, B., Huybrechs, D., Pluymers, B., Desmet, W. Coupling of Boundary Element and Wave Based Methods for the efficient solution of complex multiple scattering problems. *Journal of Computational Physics, 258, 165-184* (2014).

[6] Van Genechten, B., Atak, O., Bergen, B., Deckers, E., Jonckheere, S., Lee, J., Maressa, A., Vergote, K., Pluymers, B., Vandepitte, D., Desmet, W. An efficient Wave Based Method for solving Helmholtz problems in three-dimensional bounded domains. *Engineering Analysis with Boundary Elements, 36 (1), 63-75* (2012).

Academic Books, as author

[7] Desmet, W., Pluymers, B., Atak, O. *"MID-FREQUENCY" CAE Methodologies for Mid-Frequency Analysis in Vibration and Acoustics.* KU Leuven, (2012).

Chapters in Academic Books, as author

[8] Desmet, W., Pluymers, B., Atak, O., Bergen, B., D'Amico, R., Deckers, E., Jonckheere, S., Ku, K., Lee, J., Maressa, A., Navarrete Alzate, N., Van Genechten, B., Vandepitte, D., Vergote, K. The Wave Based Method. In: *"Mid-Frequency" CAE Methodologies for Mid-Frequency Analysis in Vibration and Acoustics*, Chapt. 1 KU Leuven, 1-60. (2012).

Articles in conference proceedings

[9] Deckers, E., Atak, O., Coox, L., D'Amico, R., Devriendt, H., Jonckheere, S., Ku, K., Pluymers, B., Vandepitte, D., Desmet, W. The Wave Based Method: current state of the art. In *Proceedings of MEDYNA 2013, 1st Euro-Mediterranean Conference on Structural Dynamics and Vibroacoustics* (MEDYNA 2013. Marrakech (Morocco), 23-25 April 2013).

[10] Atak, O., Huybrechs, D., Pluymers, B., Desmet, W. A hybrid Boundary Element - Wave Based Method for 3D acoustic multiple scattering problems. In *Proceedings of ISMA2012 International Conference on Noise and Vibration Engineering.* Leuven, 17-19 September 2012.

[11] Atak, O., Bergen, B., Huybrechs, D., Pluymers, B., Desmet, W. Application of a Hybrid Boundary Element Wave Based Method on a 2D Multiple Scatterer Problem. In *Proceedings of International Congress on Sound & Vibration.* Rio De Janeiro, Brazil, 10-14 July 2011.

[12] Van Genechten, B., Atak, O., Bergen, B., Deckers, E., Jonckheere, S., Lee, J.S., Maressa, A., Vergote, K., Pluymers, B., Vandepitte, D. and Desmet, W. An efficient wave based method for solving Helmholtz problems in three-dimensional bounded domains. In *Proceedings of the Joint International Workshop on Trefftz Method VI and Method of Fundamental Solutions II* (Kaohsiung, Taiwan, 2011).

[13] Atak, O., Bergen, B., Huybrechs, D., Pluymers, B., Desmet, W. A hybrid Boundary Element - Wave Based Method in a Multi-Level concept for steady-state 2D acoustic analysis. In *Proceedings of International Conference on Structural Dynamics (EURODYN2011)*, Leuven, Belgium, 4-6 July 2011.

[14] Desmet, W., Pluymers, B., Atak, O., Bergen, B. Deckers, E., Huijssen, J., Van Genechten, B., Vergote, K. and Vandepitte, D. Simulation Techniques for Mid-Frequency Vibro-Acoustic Virtual Tools for Real Problems. In *Proceedings of the 20th Spring Conference of the Korean Society of Noise and Vibration (KSNVE2010)* (Jeju Island, Korea, 2010).

[15] Atak, O., Huijssen, J., Rychtarikova, M., Pluymers, B., Desmet, W. Application of the Wave Based Method for mid-frequency analysis on a room acoustics case. In *Proceedings of the ISMA2010 International Conference on Noise and Vibration Engineering.* Leuven, 20-23 September 2010 (pp. 1969-1984).

Abstracts in conference proceedings

[16] Desmet, W., Atak, O., Bergen, B., D'Amico, R., Deckers, E., Jonckheere, S., Ku, K., Van Genechten, B., Vergote, K., Pluymers, B., Vandepitte, D. The Wave Based Method: an efficient alternative for vibro-acoustic predictions in the mid-frequency range. In *Proceedings of Innovations in Wave Modelling 2012.* Nottingham (UK), 3-7 September 2012.

[17] Pluymers, B., Van Genechten, B., Bergen, B., Vergote, K., Deckers, E., Atak, O., Vandepitte, D. and Desmet, W. Hybrid FE-WB methods for efficient vehicle interior cavity acoustic analysis. In *Proceedings of the 2010 Styrian Noise, Vibration and Harshness Congress (SNVH2010)* (Graz, Austria, 2010).

Master's thesis

[18] Atak, O. *Evaluation of Boundary Element Method as a Tool in Analysis of Acoustical Performance of Absorber and Screen Systems in Engine Bays.* Master's thesis, Chalmers University of Technology, 2009.